Non-Aqueous Redox Flow Batteries: Active Species Stability and Cost Saving Design Concepts

by

Sydney Laramie Fisher

A dissertation submitted in partial fulfillment
of the requirements of the degree of
Doctor of Philosophy
(Chemical Engineering)
in The University of Michigan
2017

Doctoral Committee:

Professor Levi T. Thompson, Chair
Professor Mark A. Barteau
Professor Nicholas A. Kotov
Professor Melanie S. Sanford

Sydney L. Fisher

sydneyml@umich.edu

ORCID iD: 0000-0001-8459-179X

Dedication

I would like to dedicate this dissertation to my family and my husband. Thank you for always supporting me in everything I do.

Acknowledgements

There are many people that contributed to my success in graduate school. I would like to start by thanking the members of the Thompson research group for their assistance and countless helpful discussions. Specifically Dr. Jonathan Kucharyson, Dr. Tanya Breault, Dr. Brian Wyvratt, Ryan Franck, Dr. Siu On Tung, and Yixuan Chen. I am also grateful for the assistance of the summer students that worked with me over the years: Fiki Owhoso, Avery Jones, and Scott Johnson. I would also like to thank the members of the Sanford research group that were instrumental to this research: Dr. Rachel Brooner and Dr. Christo Sevov. The members of the Brushett research group from MIT were also incredibly helpful, especially Dr. Jarrod Milshtein. Finally, I would like to thank the National Science Foundation and the Joint Center for Energy Storage Research for funding this research.

Table of Contents

List of Figures

List of Tables

Abstract

Non-aqueous redox flow batteries (NAqRFBs) have recently received considerable attention as promising high energy density grid-level energy storage devices. Despite many attractive features, NAqRFBs are still at an early stage of development and currently suffer from limited stability and high projected costs. Research described in this thesis aimed to progress NAqRFBs toward commercial viability through the development of structure-function relationships that facilitate the design of stable active species and the introduction of design strategies that significantly reduce the cost of these devices. The first section of this thesis focuses on the development of trends that relate active species structural features to solubility, electrochemistry (number of redox events, standard potentials, reversibility), and electrochemical stability. This work specifically focuses on tridentate metal coordination complexes as active species and ultimately identifies a promising nickel bipyridylimino isoindoline metal coordination complex with exceptional cycling stability (>200 cycles through $2e^-$). Taken as a whole, these results can be used to guide the future design of stable NAqRFBs. Combining the stability, solubility and electrochemical trends will allow for the rapid identification and characterization of promising active species. The second section of this thesis discusses design strategies for increasing the viability of NAqRFBs. A compatibility analysis is established to design NAqRFBs that employ active species with either single or unbalanced redox events. Further, the concept of common ion exchange is introduced as a route for decreasing the use of expensive supporting salts. Using these strategies, a proof-of-concept NAqRFB employing iron (II) tris(2,2'-bypridine) tetrafluoroborate and ferrocenylmethyl dimethyl ethyl ammonium tetrafluoroborate as the

anolyte and catholyte active species, respectively, is designed and cycled in the complete absence of supporting salt. A techno-economic analysis demonstrates that this NAqRFB configuration provides savings of >$100/kWh over traditional cells employing high concentrations of supporting salt. These concepts offer a viable route for significant cost savings and can easily be extended to other promising redox chemistries to facilitate the development of stable, soluble, multi-electron NAqRFBs.

Chapter 1

Introduction

1.1 Energy Storage

Electricity demand in all sectors has increased significantly in the past few decades and is expected to continue rising (Figure 1.1). Driven by the need to decrease carbon emissions a growing percentage of this electricity demand is predicted to be supplied by renewable resources (Figure 1.1), predominately wind and solar. [1] Despite the advantages of transitioning to a renewable portfolio, widespread grid integration is currently limited by the variable nature of these resources. In the United States, only ~2% of electricity is supplied through energy storage devices [2] and without the introduction of additional energy storage it is predicted that the grid will become unstable once electricity supplied by intermittent renewables (e.g. wind and solar) surpasses 20%. [3] The integration of energy storage will also provide overall improvements to grid reliability, utilization, and cost through peak shaving, load shifting, and frequency regulation. [2] Energy storage devices are also crucial for the successful development of smart grids and decentralized electricity generation. [4]

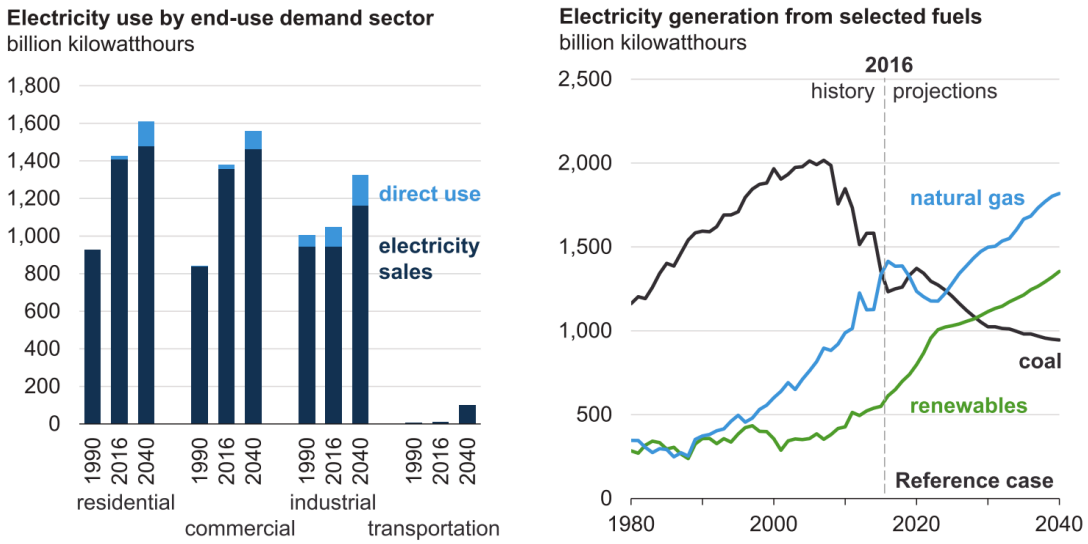

Figure 1.1 United States electricity demand and generation projections. [1]

Energy storage technologies suitable for grid scale applications can be classified into two main categories: mechanical and electrochemical systems. [5] Mechanical energy storage includes pumped-storage hydroelectricity. In this system, during times of low demand water is pumped from a lower reservoir to an upper reservoir and then during times of high demand that water is released to power turbines. [6] Compressed air energy storage (CAES) and flywheels are additional examples of mechanical storage technologies. Pumped hydroelectric storage currently dominates the market, accounting for 99% of the worldwide storage capacity. Despite their widespread use, both pumped hydroelectric and CAES are limited by geographical requirements and are only economical at a large scale. [4]

Efforts to develop more flexible technologies have led to a growing interest in a number of electrochemical devices, including both batteries and redox flow batteries. In a conventional secondary battery, at least one of the active materials is in the solid state. Examples of mature secondary electrochemical storage technologies include lead-acid and nickel-cadmium batteries,

and there are also other systems emerging for stationary applications, such as Li-ion batteries. While already fairly well established, these batteries suffer from mechanical degradation and must be carefully controlled to prevent thermal runaway. [5] Redox flow batteries (RFBs) are characterized by liquid electrolytes. Their most attractive feature is an ability to decouple energy and power, which allows for increased adaptability. In addition, RFBs offer long lifetimes, facile thermal management, and have no geographic limitations. [3] These advantages have led to significant research efforts focused on enhancing the energy density and decreasing the cost of these systems. However, substantial improvements are still necessary to make RFBs viable for widespread integration. The results I will discuss in this dissertation identify trends and establish design strategies that can be used to guide the future development of non-aqueous RFBs that approach the costs and energy densities necessary for implementation.

1.2 Redox Flow Batteries

A RFB is a large-scale energy storage system characterized by electrochemically active species dissolved in solvents and stored in separate reservoirs (Figure 1.2). This feature differentiates RFBs from conventional secondary batteries, where the active species are stored at or near the electrode surface. This unique characteristic allows the power and energy of a RFB to be scaled independently, with power being proportional to the electrode area and energy proportional to the size of the tanks. During charge and discharge, the electrolytes are pumped past electrodes on either side of a membrane or separator. This enriches one reservoir with oxidized species and the other with reduced species through an electrochemical reaction. The membrane provides electrical insulation and serves to limit crossover of the active species while allowing for the transport of non-reactive ions from the supporting electrolyte to satisfy charge

neutrality. Crossover of the active species can result in undesired reactions on either side of the RFB, leading to self-discharge and a decrease in performance. [7] RFB electrodes are typically inert materials that demonstrate low electronic resistance, high surface area, and high porosity. The most commonly employed materials are porous carbon based papers and felts, which can be modified through a variety of treatments to improve kinetics and decrease cell resistances. [3,8] In this work the anode and cathode are defined during charge, with reduction occurring at the anode (negative redox events) and oxidation at the cathode (positive redox events).

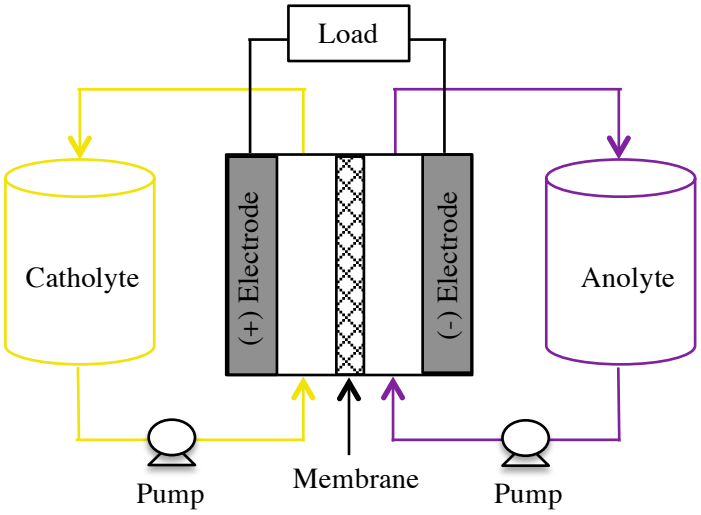

Figure 1.2 Schematic of a redox flow battery.

There are a number of performance metrics used to evaluate RFBs. One of the most important figures of merit is the energy density (E), which can be calculated using Equation 1:

$$E \approx nV_{Cell}C_{active} \qquad (1)$$

where n is the number of electrons transferred, V_{cell} is the cell voltage and C_{active} is the concentration of the active species. Increasing energy density decreases the necessary electrolyte volume as well as tank size, and is therefore an excellent route to decreasing costs. [9] An

additional performance metric is the cycle life, which is the number of cycles before a RFB reaches a certain percentage capacity fade. In this work, cycle life is defined as the number of cycles before a cell fades to 80% of the initial capacity, which is a value typically used for secondary batteries. [10] Considered together these two metrics encompass all of the requirements for an economically viable RFB: (1) high cell potential, (2) high active species solubility and (3) long cycle life. [11] Current commercial RFBs have energy densities of ~25 Wh/L and can be cycled thousands of times. [3,12] While their stability is impressive, it will be necessary to significantly improve the energy density in order to achieve widespread integration of RFBs as energy storage devices.

1.2.1 Aqueous Redox Flow Batteries

Initial efforts to develop RFBs focused on the discovery of high energy density aqueous (Aq) RFBs through the investigation of various redox couples and the advancement of cell components. [7,13–15] NASA developed the first modern AqRFB in the 1970's, which utilized Fe^{+2}/Fe^{+3} and Cr^{+2}/Cr^{+3} halide solutions as the catholyte and anolyte, respectively. This RFB had several significant shortcomings including extensive active material crossover, leading to rapid capacity fade, and poor reversibility of the Cr couple. [13] To mitigate crossover, further studies focused on an all-V system, employing V^{+4}/V^{+5} as the catholyte and V^{+2}/V^{+3} as the anolyte. [7,16,17] With only V as the active species electrolyte crossover results in decreased efficiency, instead of undesirable side reactions that limit the lifetime of the battery. The all-V RFB has been the most successful system to date with overall efficiencies as high as 85%, long lifetimes (>5000 cycles), and minimal crossover issues. [15] Aqueous all-V RFBs have been commercialized and over 20 systems have been installed worldwide. [18] However, widespread

implementation is hindered by low energy densities (25-35 Wh/L) resulting from the limited solubility of V (1.7 M) and the narrow voltage window of water (1.23 V), along with a narrow operational temperature window (10 – 40 °C). [3,10]

A number of approaches have been considered for improving the performance of all-V RFBs. Electrode treatments, including electrochemical, chemical and thermal, have been identified as promising routes to increasing power density. [19] Mixed electrolyte systems have been shown to improve the solubility of V species over a wide temperature range, with a 70% increase in energy capacity reported. [10] Finally, extensive studies have been performed to identify optimal flow field design, electrode type and number of electrode layers. [20,21] Active species development is also still an active area of research for AqRFBs. Efforts are primarily focused on inorganic species, but organic molecules have received significant attention recently due to their low cost and abundance. [22] In all cases, achieving high energy densities is difficult within the restrictive voltage window of water.

1.2.2 Aqueous vs. Non-aqueous

State of the art AqRFB chemistries are too expensive for widespread implementation. The Department of Energy (DOE) Office of Electricity Delivery and Energy Reliability set a target price of $150/kWh, including installation and inverter costs, to achieve full integration of an energy storage system that provides 4 h of storage. [23] Estimated system prices for AqRFBs in 2014, excluding installation costs, exceeded $500/kWh. [9,24] To reach the aggressive DOE target it will be necessary to significantly increase energy density as well as improve materials performance, decrease manufacturing costs, and improve cell architecture. [25] One promising route to increasing energy density is through the use of non-aqueous solvents. Non-aqueous

systems offer a number of advantages over their aqueous counterparts. First, non-aqueous solvents provide electrochemical windows that can exceed 4 V, more than triple the thermodynamic electrochemical window accessible in water (1.23 V). [26] This allows for high energy density RFBs and facilitates the use of multiple redox couples. [3] Second, a range of solvents and supporting salts are available to optimize system performance. Third, a wide array of active species is available, and through functionalization, target driven iterations can be used to tune the electrochemical and physicochemical properties of the active species. While not yet commercially viable, non-aqueous (NAq) RFBs have a number of desirable properties and do have the potential to achieve significantly higher energy densities than aqueous systems.

1.2.3 Non-aqueous Redox Flow Batteries

NAqRFBs have recently emerged as promising energy storage devices, but work to date suggests that many of the proposed active species have limited solubilities and/or stabilities in non-aqueous media. [3] To overcome these limitations, research efforts in this field are focused on active species development and characterization. Attention has mainly been focused on two classes of materials: metal coordination complexes (MCCs) and organic molecules. Recent reports describe improved active species solubilities via molecular modifications [27–29] and the development of active species with low molecular weights. [30,31] Systematic studies have also been used to establish structure-property relationships to guide the design of soluble molecules. [28,29] While extensive investigations have been performed to overcome the limited solubility of active species in non-aqueous media, there is a clear lack of studies focused on stability, and in the majority of cases the cause of poor cycling performance is not well understood.

1.2.3.1 Active Species: Metal Coordination Complexes

To solubilize redox active metals in non-aqueous media it is necessary to functionalize the metal center with organic ligands. [3] MCCs are advantageous as they have been shown to exhibit multiple, tunable, negative electron transfers in addition to positive redox events. [32] Figure 1.3 displays a number of MCCs that have been investigated as NAqRFB active species.

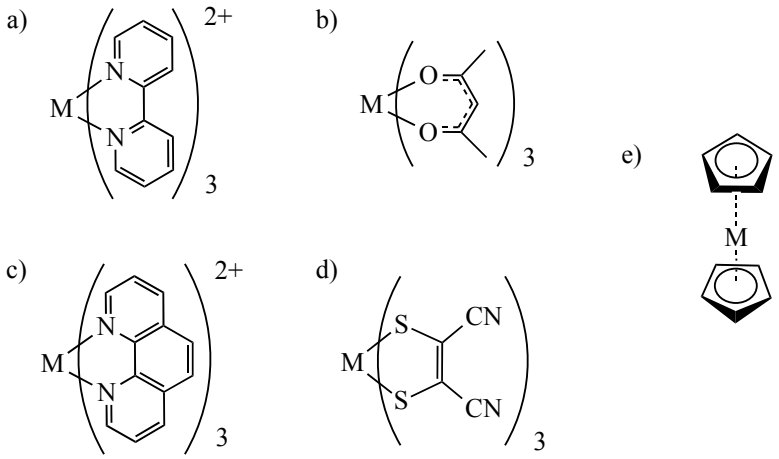

Figure 1.3 General structures of metal coordination complexes with (a) 2,2'-bipyridine, (b) acetylacetonate, (c) 1,10-phenanthroline and (d) dithiolate, and (e) cyclopentadiene ligands.

Bipyridine (bpy) MCCs were the first class of complexes proposed as active species for NAqRFBs. In the case of tris(2,2'-bipyridine) ruthenium(II) $[Ru(bpy)_3]^{+2}$, four redox couples were observed over 2.6 V, which is twice the voltage window of aqueous systems. However, the solubility of $Ru(bpy)_3$ is only 0.2 M in acetonitrile (MeCN). [33] These initial findings highlighted the promise of non-aqueous chemistries for RFB applications, but also revealed that solubility would be an issue. In subsequent years, novel active species were created through variation of the metal center and ligand modification. Chakrabarti *et al.* studied Ru complexes including ruthenium acetylacetonate, $Ru(acac)_3$, in MeCN. This system was found to have

favorable kinetics, but irreversible reactions occurred during charging that seriously limited performance. [34] Thompson *et al.* then evaluated $V(acac)_3$, $Cr(acac)_3$ and $Mn(acac)_3$ in MeCN. [35–38] $V(acac)_3$ exhibits two reversible redox couples and a cell potential of 2.2 V. However, the stability is poor and the maximum reported solubility is only 0.6 M for both $V(acac)_3$ and $Mn(acac)_3$. Phenanthroline [39] and dithiolate [40] have also been investigated as ligands with similarly poor cycling stability. The most promising MCC to date is an ionic ferrocene complex. This material has a solubility of 1.7 M in a mixture of carbonates and is stable for >100 cycles when cycled at 0.1 M against Li^+. However, when cycled at 0.8 M, <20 cycles were completed before fade to 80% of the initial capacity. [27]

In addition to the development of new ligand classes, systematic studies of bpy and acac ligand substituents have been used to develop relationships between ligand functionality, and electrochemistry and solubility. [28,29] Using these relationships, a functionalized $Cr(bpy)_3$ was synthesized that is soluble up to 0.7 M in MeCN and demonstrated six reversible electron transfers. However, this complex was only evaluated through 5 cycles and had poor coulombic efficiency (68%), indicating that it would be unstable during extended cycling. [32] In general, the literature reveals that significant advances have been made with regard to solubility, but that stability is still a major issue for MCCs. Commercial AqRFBs operate for thousands of cycles, while state of the art NAqRFBs can only perform a few hundred cycles before fading.

1.2.3.2 Active Species: Organic Molecules

Recently, organic molecules have received significant attention as NAqRFB active species. These molecules are attractive due to their low molecular weights, high solubilities and relatively low costs. [22] Many of these species were originally developed as overcharge

protection materials for Li-ion batteries, which is an application with very similar material requirements. [41] A few examples are shown in Figure 1.4.

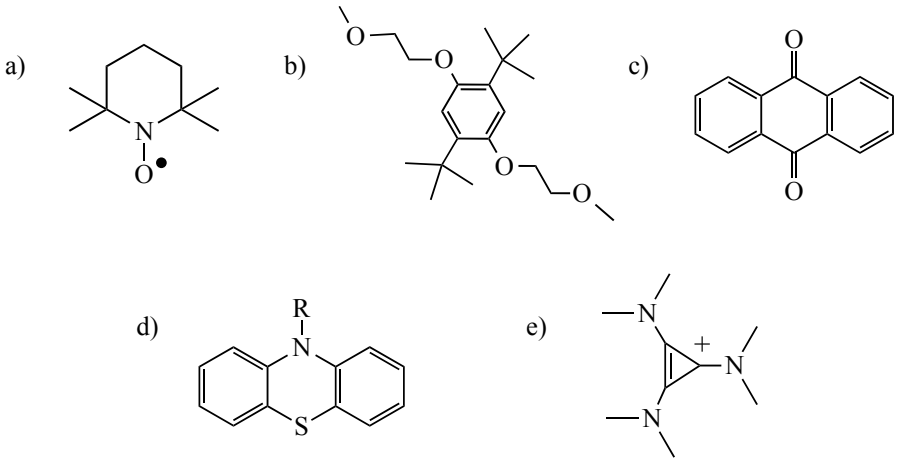

Figure 1.4 Structures of unsubstituted (a) TEMPO, (b) DBBB, (c) anthraquinone, (d) phenothiazine, and (e) cyclopropenium.

One of the most widely studied classes of organic molecules is dimethoxybenzenes (e.g. DBBB). Derivatives have been synthesized with solubilities up to 2 M in carbonate solvents, but these materials demonstrate limited stability when subjected to electrochemical cycling. [30,42–44] Following a similar trend, 2,2,6,6-tetramethylpiperidine-1-oxyl (TEMPO) is soluble up to 5.2 M in carbonate mixtures and is relatively stable for >100 cycles at a concentration of 0.1 M. [45] However, long term cycling at high concentrations has not been reported. Quinones have also been studied for non-aqueous applications, but their long term cycling stability is still unknown. [46,47] To counteract the limited stability of these early organic species, recent studies have focused on the development of more stable materials. Both phenothiazine and cyclopropenium derivatives have been identified to be stable for hundreds of cycles at moderate concentrations. [48,49] Overall, work on organic active species has made significant progress toward the

identification of materials that demonstrate high solubility and stability, however, these materials generally exhibit only a single redox event, negating one of the major advantages of moving to non-aqueous solvents.

1.2.3.3 Electrolytes

A wide variety of solvents and supporting salts are available for NAqRFB studies. [26,50,51] As discussed earlier, this additional design parameter is one advantage of non-aqueous systems over their aqueous counterparts. The most commonly employed solvents are acetonitrile (MeCN), propylene carbonate (PC) and carbonate mixtures. MeCN (0.34 mPa s) is significantly less viscous than carbonate solvents (2.53 - 3.20 mPa s), and has among the lowest viscosity of all non-aqueous solvents. This is advantageous as in general lower viscosity means higher ionic conductivity [50] and low viscosity is also desirable for minimizing pump losses in flow applications. [8] MeCN and PC also have relatively high dielectric constants and higher dielectric constant solvents have been shown to have higher solubility for supporting electrolytes and active species. [50] While carbonates do offer a slightly wider electrochemical window, the supporting salt typically dictates the upper potential limit, somewhat negating this advantage. [50] Overall, MeCN exhibits properties desirable for NAqRFB applications and as such all experiments in this thesis utilize MeCN as a solvent.

Supporting electrolytes are required to afford the ionic conductivity necessary for use in electrochemical applications. There are a variety of anions and cations available for use in non-aqueous solvents. The most commonly used anions are tetrafluoroborate (BF_4^-), perchlorate (ClO_4^-) and hexafluorophosphate (PF_6^-). BF_4^- has the smallest ionic radii and thus the highest limiting ionic conductivity of the listed anions. [50] Perchlorates are widely used, however, they

present a potential safety hazard because they can be explosive. [52] PF_6^- is known to react with trace amounts of water to produce HF. [53] This is a major issue with electrochemical glassware as HF will dissolve the glass frits employed as the separators in these cells. With these considerations in mind, BF_4^- is employed as the supporting anion throughout this thesis. The most commonly used cations are tetraalkylammoniums and Li^+. Li salts generally have low ionic conductivity due to a low degree of dissociation [54] and have been shown to negatively interact with some active species. [31] Tetraalkylammoniums offer high conductivity [50] and both TBA^+ (tetrabutylammonium) and TEA^+ (tetraethylammonium) are employed in this thesis.

1.3 Motivation for Research

1.3.1 Stability

To date, NAqRFB research has primarily focused on the discovery and characterization of novel active species with the goal of enhancing solubility. This approach has resulted in dramatic gains in solubility, but minimal concurrent enhancements in stability. Although solubility is key to achieving high energy densities, stability governs the practicality of using a material in a RFB. In many cases, the cause of capacity fade is not well understood and overall, comprehensive stability studies are lacking across all classes of NAqRFB active materials. The first part of my research focused on filling this gap by systematically studying the electrochemical stability of active species to develop an understanding of the relationships between structure and electrochemical stability. This is done while simultaneously expanding upon the relationships previously identified between structure and solubility/electrochemistry.

NAqRFB stability can be classified in terms of electrochemical or chemical stability. This work will focus primarily on electrochemical stability, which is the ability of a material to

cyclically accept and release electrons. This parameter is quantified using bulk cycling techniques, such as bulk electrolysis or cycling in flow cells. Chemical stability, on the other hand, is the ability of an active species to remain intact while interacting with the electrolyte and cell components. Shelf life studies or soak tests can be used to examine the chemical stability of an active species/material. These types of stability are not necessarily independent, but it should be noted that there are different definitions for stability and that this thesis will focus on the electrochemical version.

1.3.1 Cell Design

RFBs are currently too expensive for widespread implementation and a review of the literature reveals a lack of strategies available for reducing NAqRFB costs. [3,9,55] To achieve commercial viability it will be necessary to decrease cell costs and improve cell architecture as well as improve materials performance. The second portion of my thesis will focus on design strategies for reducing NAqRFB costs as well as routes that can be used to employ species that exhibit only a single redox event, or unbalanced redox couples.

1.4 Research Goals

The first part of this thesis will discuss the development and characterization of novel MCC active species. MCCs were selected because they exhibit multiple redox events, offer a number of tunable parameters, and are expected to provide high stability. Relationships are developed between the molecular structure of active species and solubility, electrochemistry (number of redox events, standard potentials, reversibility) and electrochemical stability. These relationships will be used to help guide the design of future multi-electron transfer active species

that exhibit the high solubility and stability necessary for NAqRFB applications. The second part of this thesis will discuss design strategies that were developed to reduce the cost of NAqRFBs. The implementation of these strategies will help decrease the costs of NAqRFBs to within range of the aggressive targets put forth by the DOE.

1.5 Chapter Summaries

1.5.1 Chapter 2: Electrochemistry and Solubility Trends for Tridentate Metal Coordination Complexes

In this chapter, I first discuss our motivation for studying MCCs and the improvements we expect to achieve through the use of tridentate ligands. I then present a series of bis(triazole)pyridine (BTP) MCCs with systematic variations in metal center and ligand substituents. Each material is characterized using solubility measurements and cyclic voltammetry, and trends are identified between these properties and molecular characteristics, including metal center and ligand functionalities. Bulk electrolysis is used to assess the stability of the BTP MCCs, and cyclic voltammograms after cycling were used to identify possible degradation mechanisms. Most importantly, the versatility of these trends is demonstrated through the synthesis and subsequent characterization of an analogous terpyridine MCC. Ultimately, this work establishes and validates trends for tridentate molecules that can be used in the design of highly soluble, reversible, and electrochemically stable active species for NAqRFBs.

1.5.2 Chapter 3: Impact of Metal Center and Ligand Structure on the Electrochemical Stability of Metal Coordination Complexes

In this chapter, I first describe the development of MCCs bearing bipyridylimino isoindoline (BPI) ligands. To understand the impact of metal center on electrochemical stability, a library of BPI MCCs is synthesized with various metal centers and identical ligand structures. Solubility measurements and cyclic voltammetry experiments are used to characterize the relevant properties of each material. Bulk electrolysis experiments are then used to quantify electrochemical stability. A promising BPI MCC was identified and modifications of the ligand substituents afforded a chemically stable complex that exhibited multiple redox couples at negative potentials as well as high solubility in acetonitrile. Overall, these results provide strategies that can be used to guide the design of stable, soluble MCCs. I conclude this chapter with a discussion of ligand characteristics that impact electrochemical stability. These considerations can be used in the selection of future ligand classes as an additional tool for the guided design of viable NAqRFB active species.

1.5.3 Chapter 4: Effect of Electrode Material on ATEMPO Stability and Flow Cell Performance

In this chapter, I discuss the effect of electrode material on the cycling stability and flow cell performance of a NAqRFB employing 4-acetamido-2,2,6,6-tetramethylpiperidine-1-oxyl (ATEMPO) as a model active species. Experiments are performed on a variety of carbon based electrode materials, including three papers, one cloth, and one felt. First, single electrolyte cells are used to carry out electrochemical impedance spectroscopy and polarization curves at varying flow rates. From these experiments, cell area specific resistance (ASR) and limiting current

densities are calculated. Next, symmetric flow cells are assembled to measure the electrochemical stability of ATEMPO on each material, using capacity retention after 100 cycles as a performance metric. Finally, a techno-economic model is used to quantify the potential cost savings associated with minimizing flow cell ASR. Overall, this work offers an assessment of the impact of electrode material on flow cell stability and performance in non-aqueous media and demonstrates the importance of component optimization for NAqRFB development.

1.5.4 Chapter 5: Active Species Compatibility Analysis for the Development of Asymmetric Non-aqueous Redox Flow Batteries

In this chapter, I discuss the design and demonstration of a series of experiments to examine the compatibility of asymmetric NAq chemistries. Iron (II) tris(2,2'-bypridine) tetrafluoroborate ($Fe(bpy)_3(BF_4)_2$) and ferrocenylmethyl dimethyl ethyl ammonium tetrafluoroborate (Fc1N112-BF_4) serve as model active species, and are examined via a progression of electrochemical techniques. This includes cyclic voltammetry, bulk electrolysis, small volume H-type cells with reference electrodes, and flow cells. Flow cell cycling experiments characterize both the one electron and, for the first time, two electron variations of the $Fe(bpy)_3(BF_4)_2$/Fc1N112-BF_4 system, revealing the complexity of multi-electron transfer cells. Taken as a whole, this work develops an extensive compatibility analysis for asymmetric NAqRFB chemistries that minimizes the use of active material and also offers a route to easily interpreting complex flow cell cycling behavior. The systematic approach and suite of electrochemical techniques utilized here can be easily extended to other promising active species, including organics, MCCs, and mixed MCC/organic systems. This versatility is demonstrated with the development of a stable, multi-electron $Co(BPI)_2$/ferrocene cell.

1.5.5 Chapter 6: Design of a Supporting Salt Free, Common Ion Exchange Non-aqueous Redox Flow Battery

In this chapter, I discuss the design and demonstration of a common ion exchange NAqRFB configured to operate in the absence of any supporting salt. Iron (II) tris(2,2'-bipyridine) tetrafluoroborate ($Fe(bpy)_3(BF_4)_2$) and ferrocenylmethyl dimethyl ethyl ammonium tetrafluoroborate ($Fc1N112\text{-}BF_4$) are selected as model anolyte and catholyte active species, respectively. First, conductivity measurements are performed to demonstrate the high conductivities of the model ionic active species in MeCN. Second, cyclic voltammetry and bulk electrolysis experiments indicate that the ionic active species maintain redox activity in the absence of supporting salt. Third, proof-of-concept flow cell experiments demonstrate the feasibility of a supporting salt free NAqRFB, exhibiting resistances and efficiencies similar to those of other recently reported NAqRFBs. Finally, a chemistry-agnostic techno-economic analysis highlights the cost savings afforded by minimizing or eliminating the amount of salt in NAqRFBs with varying active species costs, salt costs, and cell potentials. Overall, this work highlights the benefits of common ion exchange NAqRFBs, which enable higher active species concentrations, increasing electrolyte energy density, and minimizing the use of expensive NAq solvents and supporting salts. Further, the design principles outlined in this work can be extended beyond these model compounds to other active species as they are developed, including organic molecules, providing a viable route to minimizing the cost of promising future NAqRFBs.

1.5.6 Chapter 7: Conclusions and Future Directions

In this chapter, I briefly discuss the overall conclusions from my research and the relevance of these findings for advancing the field of NAqRFBs. Future directions are also

proposed for both the expansion and application of the developed structure-property relationships, and the implementation of the proposed cell design concepts.

1.6 References

[1] U.S.E.I. Administration, Annual energy outlook 2017, (2017).

[2] B. Dunn, H. Kamath, J.M. Tarascon, Electrical energy storage for the grid: a battery of choices, Science (80-.). 334 (2011) 928–35.

[3] W. Wang, Q. Luo, B. Li, X. Wei, L. Li, Z. Yang, Recent progress in redox flow battery research and development, Adv. Funct. Mater. 23 (2013) 970–986.

[4] G.L. Soloveichik, Flow batteries: current status and trends, Chem. Rev. 115 (2014) 11533–11558.

[5] G.L. Soloveichik, Battery technologies for large-scale stationary energy storage, Annu. Rev. Chem. Biomol. Eng. 2 (2011) 503–527.

[6] H. Ibrahim, A. Ilinca, J. Perron, Energy storage systems-characteristics and comparisons, Renew. Sustain. Energy Rev. 12 (2008) 1221–1250.

[7] M. Skyllas-Kazacos, M. Rychcik, R.G. Robins, A.G. Fane, New all-vanadium redox flow cell, J. Electrochem. Soc. 133 (1986) 1057–1058.

[8] B.R. Chalamala, T. Soundappan, G.R. Fisher, M.R. Anstey, V. V. Viswanathan, M.L. Perry, Redox flow batteries: an engineering perspective, Proc. IEEE. 102 (2014) 976–999.

[9] R. Darling, K.G. Gallagher, J.A. Kowalski, S. Ha, F.R. Brushett, Pathways to low-cost electrochemical energy storage: a comparison of aqueous and nonaqueous flow batteries, Energy Environ. Sci. 7 (2014) 3459–3477.

[10] L. Li, S. Kim, W. Wang, M. Vijayakumar, Z. Nie, B. Chen, J. Zhang, G. Xia, J. Hu, G. Graff, J. Liu, Z. Yang, A stable vanadium redox-flow battery with high energy density for large-scale energy storage, Adv. Energy Mater. 1 (2011) 394–400.

[11] C.S. Sevov, S.L. Fisher, L.T. Thompson, M.S. Sanford, Mechanism-based development of a low-potential, soluble, and cyclable multielectron anolyte for nonaqueous redox flow batteries, J. Am. Chem. Soc. 138 (2016) 15378–15384.

[12] M. Skyllas-Kazacos, M.H. Chakrabarti, S.A. Hajimolana, F.S. Mjalli, M. Saleem, Progress in flow battery research and development, J. Electrochem. Soc. 158 (2011) R55–R79.

[13] NASA, Redox flow cell development and demonstration project: calendar year 1977, NASA TM-79067. (1979).

[14] Q.H. Liu, G.M. Grim, A.B. Papandrew, A. Turhan, T.A. Zawodzinski, M.M. Mench, High performance vanadium redox flow batteries with optimized electrode configuration and

membrane selection, J. Electrochem. Soc. 159 (2012) A1246–A1252.

[15] C. Ponce de León, a. Frías-Ferrer, J. González-García, D. a. Szánto, F.C. Walsh, Redox flow cells for energy conversion, J. Power Sources. 160 (2006) 716–732.

[16] E. Sum, M. Rychcik, M. Skyllas-Kazacos, Investigation of the V(V)/V(IV) system for use in the positive half-cell of a redox flow battery, J. Power Sources. 16 (1985) 85–95.

[17] E. Sum, M. Skyllas-Kazacos, A study of the V(II)/V(III) redox couple for redox flow cell applications, J. Power Sources. 15 (1985) 179–190.

[18] M. Skyllas-Kazacos, G. Kazacos, G. Poon, H. Verseema, Recent advances with UNSW vanadium-based redox flow batteries, Int. J. Energy Res. 34 (2010) 182–189.

[19] A. Bourke, M.A. Miller, R.P. Lynch, J.S. Wainright, R.F. Savinell, D.N. Buckley, Effect of cathodic and anodic treatments of carbon on the electrode kinetics of V IV /V V oxidation-reduction, J. Electrochem. Soc. 162 (2015) A1547–A1555.

[20] R.M. Darling, M.L. Perry, The Influence of electrode and channel configurations on flow battery performance, J. Electrochem. Soc. 161 (2014) A1381–A1387.

[21] D.S. Aaron, Q. Liu, Z. Tang, G.M. Grim, A.B. Papandrew, A. Turhan, T.A. Zawodzinski, M.M. Mench, Dramatic performance gains in vanadium redox flow batteries through modified cell architecture, J. Power Sources. 206 (2012) 450–453.

[22] P. Leung, A.A. Shah, L. Sanz, C. Flox, J.R. Morante, Q. Xu, M.R. Mohamed, C. Ponce de León, F.C. Walsh, Recent developments in organic redox flow batteries: A critical review, J. Power Sources. 360 (2017) 243–283.

[23] D. Rastler, Market driven distributed energy storage requirements for load management applications, Palo Alto, CA, 2007.

[24] V. Viswanathan, A. Crawford, D. Stephenson, S. Kim, W. Wang, B. Li, G. Coffey, E. Thomsen, G. Graff, P. Balducci, M. Kintner-Meyer, V. Sprenkle, Cost and performance model for redox flow batteries, J. Power Sources. 247 (2014) 1040–1051.

[25] R.D. Dmello, J.D. Milshtein, F.R. Brushett, K.C. Smith, Cost-driven materials selection criteria for redox flow battery electrolytes, J. Power Sources. 330 (2016) 261–272.

[26] K. Xu, Nonaqueous liquid electrolytes for lithium-based rechargeable batteries, Chem. Rev. 104 (2004) 4303–417.

[27] X. Wei, L. Cosimbescu, W. Xu, J.Z. Hu, M. Vijayakumar, J. Feng, M.Y. Hu, X. Deng, J. Xiao, J. Liu, V. Sprenkle, W. Wang, Towards high-performance nonaqueous redox flow electrolyte via ionic modification of active species, Adv. Energy Mater. 5 (2014) 1400678.

[28] P.J. Cabrera, X. Yang, J.A. Suttil, R.E.M. Brooner, L.T. Thompson, M.S. Sanford, Evaluation of tris-bipyridine chromium complexes for flow battery applications: Impact of bipyridine ligand structure on solubility and electrochemistry, Inorg. Chem. 54 (2015) 10214–10223.

[29] J.A. Suttil, J.F. Kucharyson, I.L. Escalante-Garcia, P.J. Cabrera, B.R. James, R. F. Savinell, M.S. Sanford, L. Thompson, Metal acetylacetonate complexes for high energy

density non-aqueous redox flow batteries, J. Mater. Chem. A. 3 (2015) 7929–7938.

[30] J. Huang, L. Su, J. a. Kowalski, J.L. Barton, M. Ferrandon, A.K. Burrell, F.R. Brushett, L. Zhang, A subtractive approach to molecular engineering of dimethoxybenzene-based redox materials for non-aqueous flow batteries, J. Mater. Chem. A. 3 (2015) 14971–14976.

[31] C.S. Sevov, R.E.M. Brooner, E. Chénard, R.S. Assary, J.S. Moore, J. Rodríguez-López, M.S. Sanford, Evolutionary design of low molecular weight organic anolyte materials for applications in nonaqueous redox flow batteries, J. Am. Chem. Soc. 137 (2015) 14465–14472.

[32] P.J. Cabrera, X. Yang, J.A. Suttil, K.L. Hawthorne, R.E.M. Brooner, M.S. Sanford, L.T. Thompson, Complexes containing redox noninnocent ligands for symmetric, multielectron transfer nonaqueous redox flow batteries, J. Phys. Chem. C. 119 (2015) 15882–15889.

[33] Y. Matsuda, K. Tanaka, M. Okada, U. Takasu, M. Morita, A rechargeable redox battery utilizing ruthenium complexes with non-aqueous organic electrolyte, J. Appl. Electrochem. 18 (1988) 909–914.

[34] M.H. Chakrabarti, R.A.W. Dryfe, E.P.L. Roberts, Evaluation of electrolytes for redox flow battery applications, Electrochim. Acta. 52 (2007) 2189–2195.

[35] Q. Liu, A.E.S. Sleightholme, A.A. Shinkle, Y. Li, L.T. Thompson, Non-aqueous vanadium acetylacetonate electrolyte for redox flow batteries, Electrochem. Commun. 11 (2009) 2312–2315.

[36] Q. Liu, A.A. Shinkle, Y. Li, C.W. Monroe, L.T. Thompson, A.E.S. Sleightholme, Non-aqueous chromium acetylacetonate electrolyte for redox flow batteries, Electrochem. Commun. 12 (2010) 1634–1637.

[37] A.E.S. Sleightholme, A.A. Shinkle, Q. Liu, Y. Li, C.W. Monroe, L.T. Thompson, Non-aqueous manganese acetylacetonate electrolyte for redox flow batteries, J. Power Sources. 196 (2011) 5742–5745.

[38] A.A. Shinkle, A.E.S. Sleightholme, L.D. Griffith, L.T. Thompson, C.W. Monroe, Degradation mechanisms in the non-aqueous vanadium acetylacetonate redox flow battery, J. Power Sources. 206 (2012) 490–496.

[39] X. Xing, Y. Zhao, Y. Li, A non-aqueous redox flow battery based on tris(1,10-phenanthroline) complexes of iron(II) and cobalt(II), J. Power Sources. 293 (2015) 778–783.

[40] P.J. Cappillino, H.D. Pratt, N.S. Hudak, N.C. Tomson, T.M. Anderson, M.R. Anstey, Application of redox non-innocent ligands to non-aqueous flow battery electrolytes, Adv. Energy Mater. 4 (2014) 1300566.

[41] L. Zhang, Z. Zhang, P.C. Redfern, L.A. Curtiss, K. Amine, Molecular engineering towards safer lithium-ion batteries: a highly stable and compatible redox shuttle for overcharge protection, Energy Environ. Sci. 5 (2012) 8204.

[42] F.R. Brushett, J.T. Vaughey, A.N. Jansen, An all-organic non-aqueous lithium-ion redox

flow battery, Adv. Energy Mater. 2 (2012) 1390–1396.

[43] J. Huang, L. Cheng, R.S. Assary, P. Wang, Z. Xue, A.K. Burrell, L.A. Curtiss, L. Zhang, Liquid catholyte molecules for nonaqueous redox flow batteries, Adv. Energy Mater. 5 (2015) 1–6.

[44] J. Huang, B. Pan, W. Duan, X. Wei, R.S. Assary, L. Su, F.R. Brushett, L. Cheng, C. Liao, M.S. Ferrandon, W. Wang, Z. Zhang, A.K. Burrell, L.A. Curtiss, I.A. Shkrob, J.S. Moore, L. Zhang, The lightest organic radical cation for charge storage in redox flow batteries, Sci. Rep. 6 (2016) 32102.

[45] X. Wei, W. Xu, M. Vijayakumar, L. Cosimbescu, T. Liu, V. Sprenkle, W. Wang, TEMPO-based catholyte for high-energy density nonaqueous redox flow batteries, Adv. Mater. 26 (2014) 7649–7653.

[46] W. Wang, W. Xu, L. Cosimbescu, D. Choi, L. Li, Z. Yang, Anthraquinone with tailored structure for a nonaqueous metal-organic redox flow battery, Chem. Commun. 48 (2012) 6669–71.

[47] L. Cheng, R.S. Assary, X. Qu, A. Jain, S.P. Ong, N.N. Rajput, K. Persson, L.A. Curtiss, Accelerating electrolyte discovery for energy storage with high-throughput screening, J. Phys. Chem. Lett. 6 (2015) 283–291.

[48] J.D. Milshtein, A.P. Kaur, M.D. Casselman, J.A. Kowalski, S. Modekrutti, P. Zhang, N.H. Attanayake, C.F. Elliott, S.R. Parkin, C. Risko, F.R. Brushett, S.A. Odom, High current density, long duration cycling of soluble organic active species for non-aqueous redox flow batteries, Energy Environ. Sci. 9 (2016) 3531–3543.

[49] C.S. Sevov, S.K. Samaroo, M.S. Sanford, Cyclopropenium salts as cyclable, high-potential catholytes in nonaqueous media, Adv. Energy Mater. (2016) 1602027.

[50] K. Gong, Q. Fang, S. Gu, S.F.Y. Li, Y. Yan, Nonaqueous redox-flow batteries: organic solvents, supporting electrolytes, and redox pairs, Energy Environ. Sci. 8 (2015) 3515–3530.

[51] A. a. Shinkle, T.J. Pomaville, A.E.S. Sleightholme, L.T. Thompson, C.W. Monroe, Solvents and supporting electrolytes for vanadium acetylacetonate flow batteries, J. Power Sources. 248 (2014) 1299–1305.

[52] W.R. Robinson, Perchlorate salts of metal ion complexes: potential explosives, J. Chem. Educ. 62 (1985) 1001.

[53] C.W. Barlow, Reaction of water with hexafluorophosphates and with Li bis(perfluoroethylsulfonyl)imide salt, Electrochem. Solid-State Lett. 2 (1999) 362–364.

[54] J. Milshtein, S. Fisher, T. Breault, L. Thompson, F. Brushett, Feasibility of a supporting salt free non-aqueous redox flow battery utilizing ionic active materials, ChemSusChem. 10 (2017) 2080–2088.

[55] Q. Huang, Q. Wang, Next-generation, high-energy-density redox flow batteries, Chempluschem. 80 (2015) 312–322.

Chapter 2

Electrochemistry and Solubility Trends for Tridentate Metal Coordination Complexes

2.1 Background and Approach

Nonaqueous redox flow batteries (NAqRFBs) are emerging as promising devices for large scale energy storage applications, however, significant progress is still necessary for this technology to be considered market ready. A key challenge on the path to commercial viability is the development of active species that exhibit electrochemical reversibility, high solubility and cycling stability. [1] To date, there are few reports of active species that meet all of these criteria. Furthermore, there is limited information available on the molecular characteristics that impact each of these properties. To enable the efficient design of new active materials it will be necessary to first understand the structural features that impact electrochemical reversibility, solubility and cycling stability.

Work described in this dissertation is focused specifically on using metal coordination complexes (MCCs) to develop these active species trends. MCCs are highly tunable, offering a broad design space through modification of the metal center, ligand structure and ligand functionalities. [2] Recent efforts have focused on the development of MCCs with non-innocent ligands, which are ligands that exhibit redox activity. [3] These materials are capable of multiple electron transfers at both high and low potentials by utilizing the redox activity of both the metal

center and the ligand. Initial studies have focused on the development of active species with bidentate ligands, including bipyridine, [4–6] acetylacetonate [7–9] and dithiolate. [10] In general, these MCCs suffer from limited stability due to facile ligand dissociation during electrochemical cycling. [11] One possible route to enhancing stability is through the use of higher denticity ligands. In an effort to mitigate ligand shedding while retaining the capability of multiple electron transfers, this work investigates non-innocent tridentate MCCs.

Previous studies have examined the impact of molecular structure on the electrochemical properties and solubility of tris-bipyridine chromium [12] and chromium acetylacetonate complexes. [13] In an effort to expand upon these trends for tridentate systems we sought a ligand system with a modular synthesis that allowed for substitution at various sites on the ligand backbone using common building blocks and a standard synthetic protocol. This type of system minimizes the time and resources necessary for ligand synthesis, enabling rapid development of a library of active species. Based on these criteria, we focused our initial efforts on complexes with tridentate 2,6-bis(1,2,3-triazol-4-yl)pyridine (BTP) ligands. These ligands are synthesized using "click" cycloaddition of organic azides to a 2,6-bis(ethynyl)pyridine core and have been shown to form octahedral, bis-ligated metal complexes with a variety of transition metal ions. [14–16] Furthermore, seminal reports suggest that the redox activity of a $[Fe(BTP)_2]^{2+}$ complex is comparable to that of an analogous terpyridine complex $[Fe(tpy)_2]^{2+}$, which has been shown to undergo ligand-based reductions. [14] While the potential of this "clicked" scaffold has been investigated for electronic materials applications we sought to use the readily modified ligand structure to systematically assess a series of first-row transition metal complexes for use in NAqRFBs.

In this chapter, I first discuss our motivation for studying MCCs and the potential advantages of tridentate ligands. I then present results for a series of BTP MCCs with systematic variations in metal center and ligand substituents. Each material is characterized using solubility measurements and cyclic voltammetry (CV), and trends are identified between these properties and molecular characteristics, including metal center and ligand functionalities. Bulk electrolysis (BE) is used to assess the stability of the BTP MCCs, and CVs after cycling identify electroactive degradation products and possible degradation mechanisms. Most importantly, the versatility of these trends is demonstrated through the synthesis and subsequent characterization of an analogous terpyridine MCC. Ultimately, this work establishes and validates trends for tridentate molecules that can be used in the design of highly soluble, reversible and electrochemically stable active species for NAqRFBs.

2.2 Experimental

2.2.1 Synthesis

*2.2.1.1 Ligands **L1** – **L6***

Bis(triazole)pyridine ligands were synthesized in a one pot, two step procedure from alkyl halides, through *in situ* generation of alkyl azides, and bis(TMS-ethynyl)pyridines (Figure 2.1). A 100 mL round-bottom Schlenk flask with Teflon-lined screw cap and stir bar was charged with sodium azide (4.5 equiv) and H_2O (0.45 M in azide). The corresponding alkyl bromide (3 equiv) was added to the solution, the flask was capped, and mixture was heated to 95 °C and stirred for 12-14 h. The mixture was cooled to room temperature then 0 °C, and to the flask were added potassium carbonate (2.5 equiv), $CuSO_4 \cdot 5H_2O$ (0.2 equiv), ascorbic acid (0.4 equiv), and a solution of 2,6-di(trimethylsilylethynyl)pyridine (0.1 M, 1 equiv) in *t*-BuOH. The

flask was re-capped, and the reaction was warmed to room temperature and stirred 24 hours. Upon completion, the crude orange/brown reaction mixture was diluted with H_2O, aq. NH_4OH, and CH_2Cl_2. Chelex resin was added, and the mixture was stirred vigorously until it fully separated into clear colorless or pale-yellow organic and aqueous phases and the resin turned blue. The mix was filtered then transferred to a separatory funnel, the layers were separated, and the aqueous phase was further extracted with CH_2Cl_2. The combined organic layers were dried over Na_2SO_4, filtered, and concentrated. Ligands were isolated via column chromatography (SiO_2).

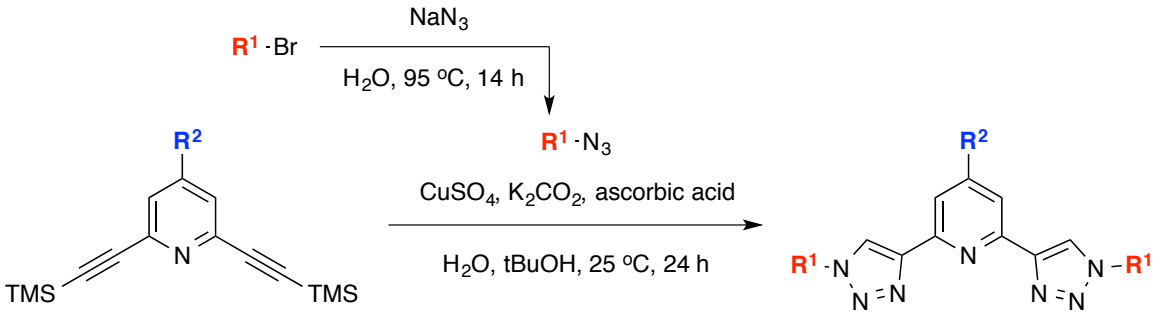

Figure 2.1 Procedure used to synthesize the 2,6-bis(1-alkyl-1,2,3-triazol-4-yl)pyridine ligands.

*2.2.1.2 [Fe(**L**)$_2$](BF$_4$)$_2$ Complexes (**L2 – L6**)*

The high solubility of $[Fe(L)_2](BF_4)_2$ complexes of **L3 – L6** precluded their synthesis via the typical route, which involves ligation of $FeSO_4$ in a water/alcohol mix then counter-ion exchange and precipitation of the BF_4 salt. Therefore, an alternative method was developed. In a separatory funnel, a solution of $FeSO_4 \cdot 7H_2O$ (0.01 M, 1.0 equiv) in sat. aq. $NaBF_4$ was treated with a solution of ligand (0.01 M, 2.0 equiv) in CH_2Cl_2. The resultant orange/red mixture was shaken vigorously for 15 sec then allowed to separate. The dark orange/red organic layer was

collected, dried over anhydrous $NaBF_4$, and concentrated to ~1/2 its original volume. An equal volume of Et_2O was added, and the resulatant orange or red precipitate was collected by filtration, washed with Et_2O, and dried *in vacuo*.

2.2.2 Solubility

Solubility measurements of the synthesized active species were performed using a UV/Visible method with absorbance measurements performed in air using a Shimadzu UV-1601 spectrophotometer. [12] Stock solutions of the active species in acetonitrile (MeCN) were prepared and used to create a calibration curve of characteristic peak absorbance as a function of active species concentration. The individual active species were then added in excess to MeCN to generate a suspension. The saturated solutions were filtered through cotton wool to remove any undissolved solids. The remaining solution was then diluted with MeCN to within the range of the calibration curve, and the absorption of the diluted solution was measured. Maximum solubilities were calculated based on the dilutions.

2.2.3 Cyclic Voltammetry

CV experiments allow a quick assessment of electrochemical behavior. This technique provides information on: number of redox events, standard potentials, reversibility, diffusivity and kinetics. An example voltammogram is shown in Figure 2.2. The standard potential of a redox couple is defined as the average of E_p^{anodic} and $E_p^{cathodic}$. For a reversible system the theoretical peak separation (difference between E_p^{anodic} and $E_p^{cathodic}$) is 59/n mV, where n is the number of e^- transfers. However, this separation is very difficult to achieve, particularly in non-aqueous solvents with limited conductivity, and values of 80 – 100 mV are more typical. Even

larger separations suggest slow kinetics or high solution resistance. Peak height ratios ($i_p^{anodic}/i_p^{cathodic}$) provide a measure of reversibility. A fully reversible redox event will have a peak height ratio of unity, where all of the material that is oxidized is subsequently reduced, or vice versa. Diffusion coefficients and reaction rate constants can be measured by conducting CVs at varying scan rates. Active species diffusivity can potentially impact the maximum achievable power density in a flow cell, however, within a family of MCCs negligible variations have been observed. [13] The reaction kinetics will impact the overpotentials observed in a flow cell, but in general non-aqueous chemistries exhibit facile kinetics [2] and CV offers only an order of magnitude estimate of this parameter. As such, these values are not covered in this dissertation and these calculations will not be discussed. Overall, CV is a rapid technique that provides an initial assessment of electrochemical behavior while requiring only a small amount of active material. However, only the material immediately adjacent to the electrode surface reacts, so reversibility measured by CV is not necessarily representative of reversibility that will be observed in a battery cycling experiment where the entire solution changes oxidation state.

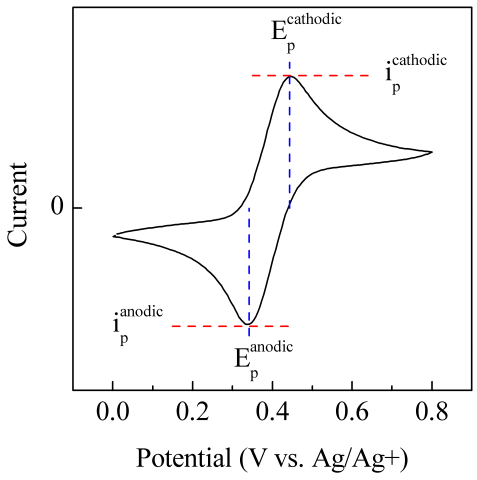

Figure 2.2 Example CV with peak potentials (E_p) and peak heights (i_p) labeled with blue and red dashed lines, respectively.

For this work, all solution preparation and electrochemical measurements were performed inside an argon filled glove box (O_2 < 5 ppm, H_2O < 1 ppm). CVs were measured in a custom 10 mL, three-electrode electrochemical cell with a 3 mm diameter glassy carbon working electrode (BASi), a coiled Pt wire counter electrode, and a Ag/Ag^+ quasi-reference electrode (BASi). The reference electrode was a fritted chamber containing 0.01 M silver tetrafluoroborate (98%, Sigma Aldrich) in MeCN and a silver wire. CVs were recorded using an Autolab PGSTAT302N potentiostat at a scan rate of 100 mV s^{-1}. All solutions contained 5 mM of the individual active species and 0.1 M $TBABF_4$ (electrochemical grade, >99%, Sigma Aldrich) dissolved in MeCN (99.9%, Acros Organics).

2.2.4 Bulk Electrolysis

BE studies provide an initial evaluation of active species electrochemical stability. For these experiments, a three-electrode electrochemical cell is used to cyclically alter the oxidation state of the bulk electrolyte solution. This technique can be used to gather information on the stability of all charge states that would be accessed during full cell cycling. Coupled with CV experiments on the cycled material, this method can also be used to identify possible degradation mechanisms. This technique is often performed at low concentrations, although it is relevant over a wide range of conditions (2 mM – 0.1 M), and only requires small volumes of solution, minimizing the use of active material. BE is especially powerful as only the working electrode is controlled during charge and discharge, thus enabling the analysis of the stability of individual redox events. One limitation of note is the deleterious effects of crossover on the measured cycle life. As only the working chamber is controlled, significant degradation typically occurs in the counter chamber. Over time, the degraded material diffuses through the cell to the working

chamber, potentially contributing to capacity fade. Therefore, while offering an excellent initial assessment of stability, these experiments provide a lower bound on active species performance.

Cycling experiments can be performed at either constant current while measuring the potential response or constant potential while measuring the current response. In general, constant current cycling provides more information as the potential curves can be used to understand which redox events are being accessed. In this type of experiment the working electrode is held at a constant current, and appropriate cutoffs (capacity, state-of-charge, potential) are used to repeatedly alternate between charge and discharge. Metrics of interest include capacity retention/cycle life and coulombic efficiency. In this work, cycle life is defined as the number of cycles before reaching 80% of the initial capacity. Coulombic efficiency is the ratio of discharge capacity to charge capacity, commonly reported as a percentage. This value provides information on losses due to irreversibility/instability of the redox event and crossover. Voltaic efficiencies can also be calculated, but as the potential is measured versus a reference electrode, not the counter electrode, these values are meaningless.

BE experiments are performed in a custom glass H-type cell (Figure 2.3) consisting of two 5 mL chambers separated with an ultra-fine glass frit (P5, Adams and Chittenden). The use of a glass frit to isolate the chambers avoids the need for a separator or membrane. Many common membranes and separators are incompatible with non-aqueous solvents [17] and can lead to deleterious side reactions that convolute the cycling behavior. Reticulated vitreous carbon (RVC), a high surface area glassy carbon, is used as the working electrode. This material offers high surface area, similar surface chemistry to the glassy carbon electrodes used for CV, and is electrochemically inert. [18] A separate port is available for a glassy carbon (GC) electrode to

perform CV studies before and after cycling. The cell is fully sealed once assembled and both chambers are stirred continuously during cycling.

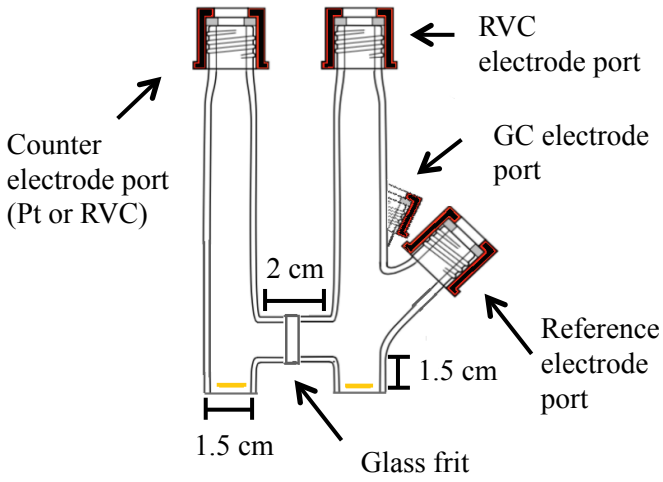

Figure 2.3 Schematic of the BE cell used in this work.

For this work, solutions were composed of 5 mM of the active species dissolved in 0.5 M $TBABF_4$ / MeCN. RVC (100 PPI, Duocell) was used as the working electrode with a Pt coil counter electrode and Ag/Ag^+ quasi-reference electrode. An Autolab PGSTAT302N potentiostat was used to apply a constant potential. The charge and discharge potentials used for each experiment are reported with the results, and were determined using the redox potentials of each material observed by CV. Both a current cutoff (0.3 mA) and a coulombic cutoff (100% SOC) were used to control each experiment. A 3 mm diameter glassy carbon working electrode (BASi) was used to record CVs before and after cycling.

2.3 Results and Discussion

2.3.1 Motivation to Study MCCs

Current efforts toward developing NAqRFB active species are focused primarily on two classes of materials: redox active organics and MCCs. Organic molecules have received increasing attention due to their low molecular weights, offering potentially higher solubilities and lower costs. [19,20] Recent reports have identified organics that demonstrate high stability and solubility, [21,22] however, performance is limited at high concentrations and the vast majority of organic molecules only exhibit a single redox event. As discussed previously, the development of materials capable of multiple electron transfers is a very promising route toward increasing energy density. Although larger than organics, MCCs exhibit multiple redox couples at potentials that can be tailored to a given application. Further, MCCs offer a variety of routes for synthetic modifications, including variation of the metal center, ligand structure and ligand substituents. Most importantly, MCCs may offer higher stability than their organic counterparts. These advantages are demonstrated with a comparison of the electrochemical performance of bipyridine (bpy) and iron (II) tris(2,2'-bypridine) tetrafluoroborate ($Fe(bpy)_3(BF_4)_2$). A CV of bpy is shown in Figure 2.4a, exhibiting a single reversible redox event at a relatively negative potential. A single bulk electrolysis cycle through this negative couple reveals significant instabilities. The potential curve during charging (Figure 2.4b) is very flat, suggesting the material is decomposing immediately upon charging. The material is also unable to discharge, further supporting this evaluation. A CV after cycling (Figure 2.4a, dashed) reveals that the peak height of the characteristic bpy peak has decreased substantially and an electrochemically active degradation product is now present with a peak around -0.3 V.

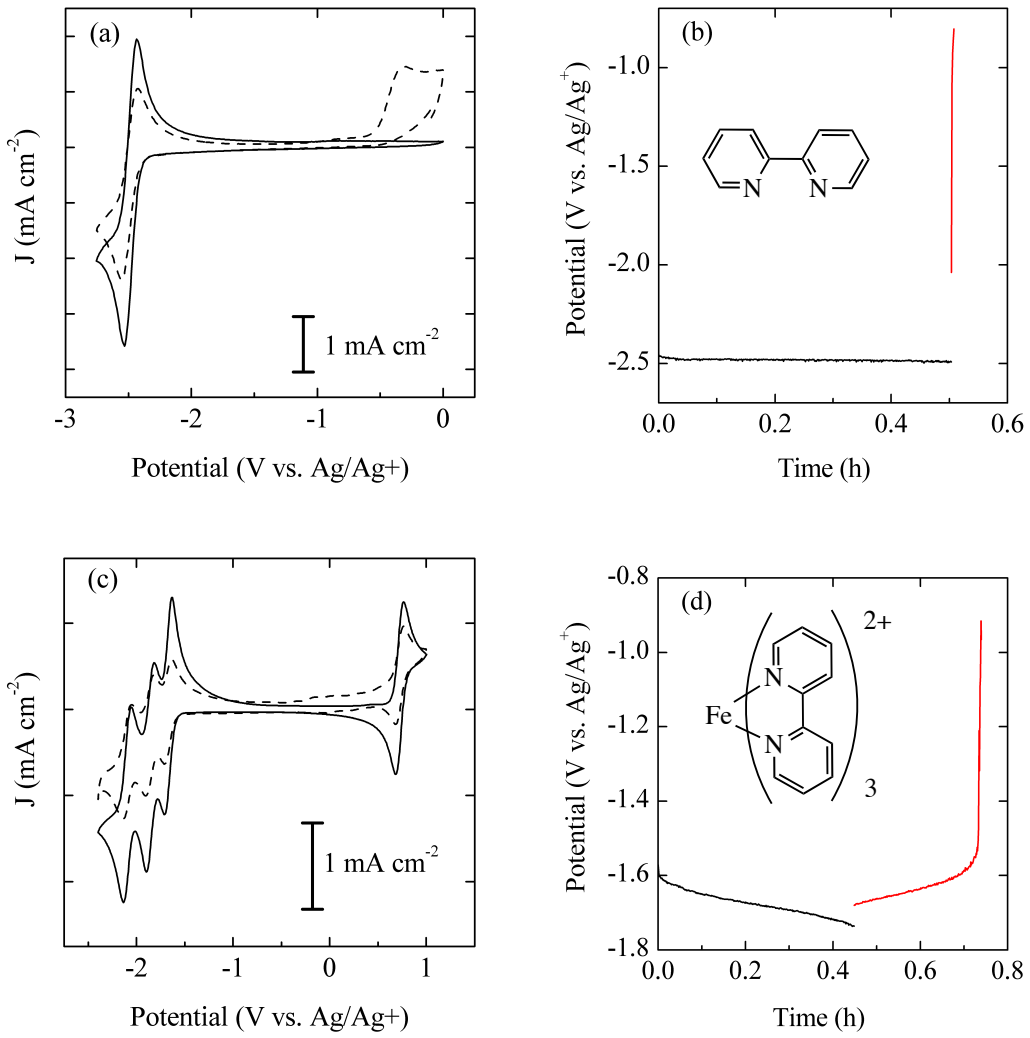

Figure 2.4 CVs before (solid) and after (dashed) **(a)** a single cycle of bpy and **(c)** 25 cycles of $Fe(bpy)_3(BF_4)_2$ through 1 negative e^-. Structure and potential curves for the first charge (black) and discharge (red) of **(b)** bpy and **(d)** $Fe(bpy)_3(BF_4)_2$.

Once metallated the electrochemical behavior of bpy changes dramatically. A CV of $Fe(bpy)_3(BF_4)_2$ exhibits four reversible redox couples, (Figure 2.4c) with each negative redox event associated with ligand activity and the positive couple a result of the $Fe^{II/III}$ transition. [23] Compared to bpy, the couples of $Fe(bpy)_3(BF_4)_2$ have decreased peak heights. This is due to the increased size, and subsequent decrease in diffusivity, of $Fe(bpy)_3(BF_4)_2$. Upon cycling, the charging potential curve displays the expected Nernstian shape and the material is now able to

discharge (Figure 2.4d). A CV after cycling (Figure 2.4c) shows that $Fe(bpy)_3(BF_4)_2$ is degrading over time, but at a significantly slower rate than that for bpy. The degradation of $Fe(bpy)_3(BF_4)_2$ after 25 cycles is comparable to that of bpy after a single cycle.

These results provide motivation for studying MCCs as active species. As stated previously, they offer multiple redox couples and potentially higher stability. While organics exhibit a number of promising attributes, the first step towards a feasible NAqRFB will necessarily be the development of a stable active species that exhibits multiple electron transfers. MCCs show promise for achieving these aims.

2.3.2 Motivation to Study Tridentate MCCs

To date, efforts to develop MCCs for NAqRFB applications have focused primarily on complexes with bidentate ligands. [10,12,13] In general, these materials suffer from poor stability as a result of ligand shedding during electrochemical cycling. Our motivation for studying tridentate MCCs is an anticipated increase in electrochemical stability due to a stronger bond between the ligand and the metal center. [23] This expected improvement in stability is investigated using a comparison between $Fe(bpy)_3(BF_4)_2$ and iron (II) terpyridine tetrafluoroborate ($Fe(tpy)_2(BF_4)_2$) (Figure 2.5c). These materials provide an excellent comparison point as they have nearly identical ligand structures with only a difference in denticity. Furthermore, they are relevant for NAqRFB applications, as bipyridine has been investigated extensively as an active species. [6,12,24–26]

CVs for each material are shown in Figure 2.5a. In both cases the negative redox activity is associated with ligand activity while the positive redox event results from the $Fe^{II/III}$ transition. Ligand dissociation typically occurs at negative potentials, so comparative bulk electrolysis

experiments were performed through a single negative electron transfer. The capacity retention for each material is shown in Figure 2.5b. $Fe(bpy)_3(BF_4)_2$ starts to fade immediately at a fairly rapid rate while $Fe(tpy)_2(BF_4)_2$ demonstrates substantially better stability. These experiments validate that tridentate ligands do offer increased stability and motivated our studies of the development of tridentate MCCs as NAqRFB active species.

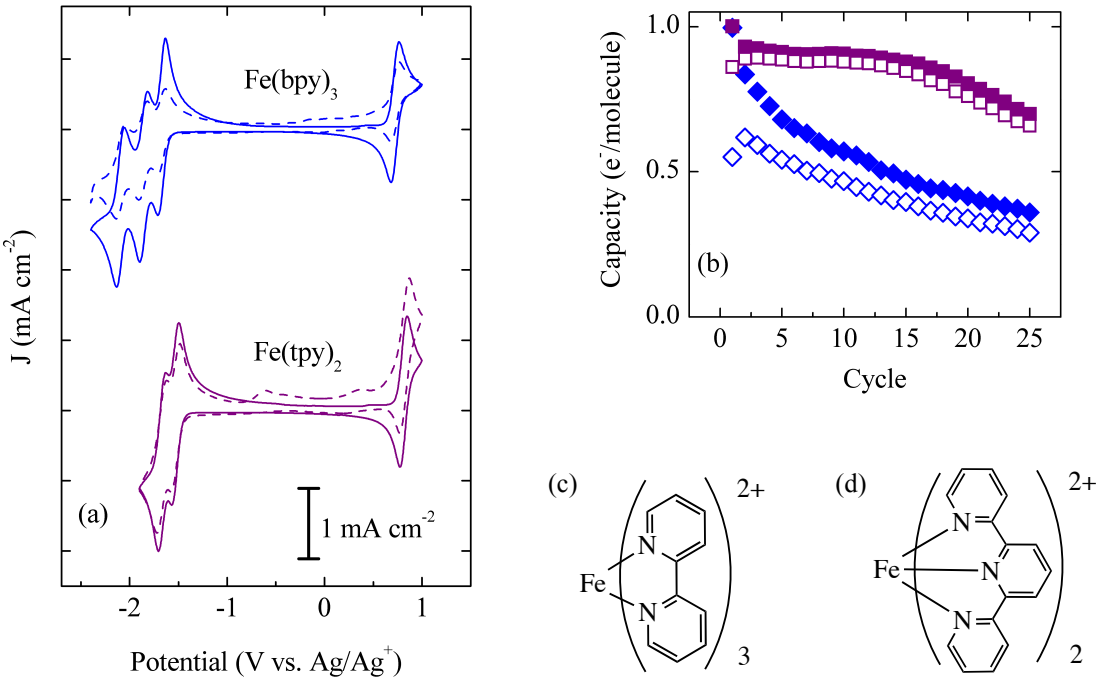

Figure 2.5 (a) CVs of $Fe(bpy)_3(BF_4)_2$ and $Fe(tpy)_2(BF_4)_2$ before (solid) and after 25 BE cycles (dashed). **(b)** Capacity retention for cycling through a single negative electron: $Fe(bpy)_3(BF_4)_2$ (■) and $Fe(tpy)_2(BF_4)_2$ (◆) with both charge (solid) and discharge (open) capacities. Structures of **(c)** $Fe(bpy)_3(BF_4)_2$ and **(d)** $Fe(tpy)_2(BF_4)_2$.

2.3.3 Active Species Selection and Synthesis

After confirming the attractive features exhibited by tridentate MCCs, it was necessary to select an appropriate ligand scaffold for further studies. While terpyridine MCCs are promising, the ligand is difficult to functionalize and the complexes have poor solubility in NAq solvents.

For this work, we sought a ligand system with a modular synthesis that allowed for substitution at various sites on the ligand backbone using common building blocks and a standard synthetic protocol. Additionally, it was desirable for this MCC to exhibit multiple, reversible electron transfers over a wide potential window and moderate solubility in MeCN. Based on these criteria, we focused our efforts on complexes of tridentate BTP ligands.

The BTP ligands were synthesized in a one-pot, two step procedure from bench-stable starting materials. This method allowed for the modular synthesis of a variety of ligands with different substituents on both the triazole and pyridine rings from common precursors, which subsequently enabled the systematic study of the effect of ligand substitution on metal complex solubility and electrochemistry. Dr. Rachel Brooner performed all of the synthetic work and additional details can be found in Sections 2.2.1.1 and 2.2.1.2. The complexes were characterized using elemental analysis, IR spectroscopy and ^{1}H, ^{13}C, and ^{19}F NMR. Figure 2.6 displays the ligands that were synthesized for this study. Systematic variations of the metal center and ligand functionalities were used to establish the impact of each alteration on the solubility and electrochemical behavior of tridentate MCCs.

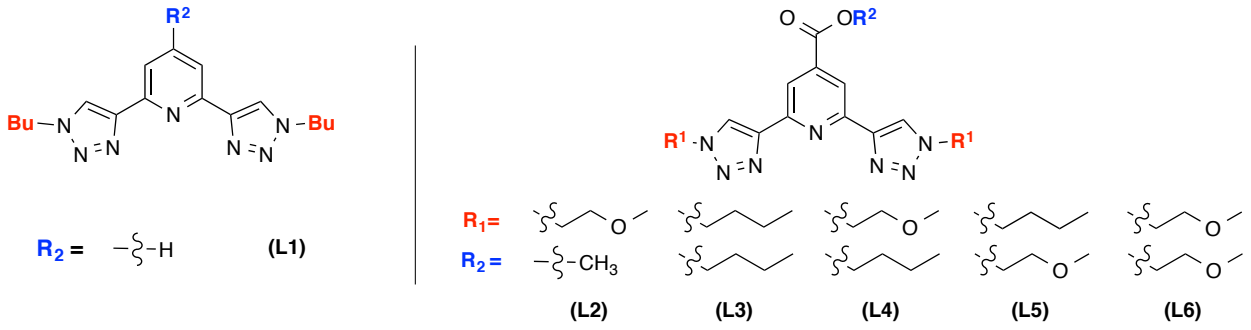

Figure 2.6 Structures of all bis(triazole)pyridine ligands studied (**L1–L6**).

2.3.4 Solubility

The first aim of this study was to establish trends between solubility and the molecular characteristics of tridentate MCCs. To develop these relationships, the solubilities of a series of metallated BTP complexes were measured using UV/Visible spectrophotometry (Table 2.1). First, to assess the impact of metal center on solubility, the metal center was varied while maintaining an identical ligand structure. A comparison of the solubility of $[Fe(\mathbf{L2})_2](BF_4)_2$, $[Co(\mathbf{L2})_2](BF_4)_2$ and $[Ni(\mathbf{L2})_2](BF_4)_2$ in MeCN reveals nearly an order of magnitude difference between the metal centers. An increase in solubility in the order Ni < Co < Fe was observed, revealing a correlation with decreasing atomic number. This trend is in agreement with reports of other tridentate MCC solubilities [11] and has been attributed to decreased charge shielding by the ligand for earlier transition metals. Since $[Fe(\mathbf{L2})_2](BF_4)_2$ afforded the highest solubility of the reported bis-**L2** complexes, Fe was selected as the metal center for additional studies with the aim of further enhancing solubility. Butyl and 2-methoxyethyl chains were selected to achieve this goal as they have previously been shown to increase the solubility of MCCs in MeCN. [12] A systematic variation of ligand functionalities using these groups, $[Fe(\mathbf{L3})_2](BF_4)_2$ – $[Fe(\mathbf{L6})_2](BF_4)_2$, reveals that it is possible to selectively tune solubility using only the ligand substituents. A four-fold increase in solubility was achieved using these targeted structural variations, with $[Fe(\mathbf{L5})_2](BF_4)_2$ reaching 0.7 M solubility in MeCN. Interestingly, complexes $[Fe(\mathbf{L3})_2](BF_4)_2$ and $[Fe(\mathbf{L6})_2](BF_4)_2$, whose ligands included all butyl or all methoxyethyl chains, respectively, exhibited essentially the same solubility in MeCN (~0.5 M). In contrast, complexes $[Fe(\mathbf{L4})_2](BF_4)_2$ and $[Fe(\mathbf{L5})_2](BF_4)_2$, with ligands that incorporated both butyl chains and methoxyethyl chains in combination were more soluble in MeCN than either of their more symmetric counterparts, suggesting that the introduction of ligand asymmetry can be used

to enhance solubility. Similar increases in solubility have been observed for asymmetric organic molecules and attributed to the creation of additional intramolecular dipole moments. [27]

Table 2.1: Solubility of metallated **L1-L6**.

Complex	Solubility in MeCN (mM)
$[Fe(\mathbf{L1})_2](BF_4)_2$	214 ± 6
$[Fe(\mathbf{L2})_2](BF_4)_2$	193 ± 6
$[Co(\mathbf{L2})_2](BF_4)_2$	130 ± 3
$[Ni(\mathbf{L2})_2](BF_4)_2$	53 ± 1
$[Fe(\mathbf{L3})_2](BF_4)_2$	553 ± 37
$[Fe(\mathbf{L4})_2](BF_4)_2$	641 ± 17
$[Fe(\mathbf{L5})_2](BF_4)_2$	769 ± 94
$[Fe(\mathbf{L6})_2](BF_4)_2$	554 ± 24

2.3.5 Electrochemistry

The second aim of this work was to establish relationships between structural characteristics and electrochemical properties, including the number of redox events, standard potentials and reversibility.

*2.3.5.1 Metal Complexes of **L1** – **L2***

To examine the range of electrochemistries available within the selected ligand scaffold, CV was used to characterize Fe, Co and Ni octahedral bis-ligated metal coordination complexes of **L1** and **L2**. Potential windows for each complex were selected to include all reversible couples within the electrolyte window. For this study, reversibility is defined as a peak height ratio of ~1. A comparison between Fe, Co and Ni complexes of **L1** reveals the significant effect of the metal center on electrochemical behavior (Figure 2.7). According to previous reports, the redox couple of $[Fe(\mathbf{L1})_2](BF_4)_2$ at 0.9 V vs. Ag/Ag^+ corresponds to the Fe^{II}/Fe^{III} transition,

while both negative redox events have been assigned to ligand redox activity. [14] A comparison between [Fe(**L1**)$_2$](BF$_4$)$_2$ and [Fe(**L2**)$_2$](BF$_4$)$_2$ reveals that modifications to the peripheral ligand structure primarily affect the negative electrochemistry, supporting this assignment of the redox events. **L1** and **L2** complexes of Ni and Co also show analogous differences in electrochemical behavior, enabling a similar assignment of redox activity. Furthermore, neither [Ni(**L1**)$_2$](BF$_4$)$_2$ or [Ni(**L2**)$_2$](BF$_4$)$_2$ display any positive redox couples within the measured window, which can be attributed to the difficulty of accessing Ni^{III} at low potentials. [28] Beyond these general similarities in redox assignments, each metal demonstrates variations in the potential, reversibility and quantity of the observed redox couples. [Ni(**L1**)$_2$](BF$_4$)$_2$ and [Ni(**L2**)$_2$](BF$_4$)$_2$ exhibit irreversible redox activity with redox events that are difficult to distinguish. Both [Co(**L1**)$_2$](BF$_4$)$_2$ and [Fe(**L1**)$_2$](BF$_4$)$_2$ demonstrate reversible behavior, however, the positive redox event of [Co(**L1**)$_2$](BF$_4$)$_2$ demonstrates slow kinetics, as indicated by significant peak splitting. Similar behavior has previously been observed on glassy carbon for Co complexes with azole-pyridine ligands and was suggested to be a result of a spin change required for the $Co^{III/II}$ couple. [29,30] Overall, the Fe BTP complexes demonstrate the most promising electrochemistry, with redox couples that are reversible and exhibit facile kinetics. Further, these couples span a wide voltage window, with a symmetric NAqRFB utilizing the single positive couple as the catholyte and the first negative redox event as the anolyte providing a potential of 2.57 V for **L1** or 2.32 V for **L2**.

In addition to comparing the electrochemistry for different metal centers, the impact of varying ligand substituents on the electrochemical behavior of the tridentate BTP MCCs was also evaluated. It has previously been reported that the incorporation of functional groups onto the rings of bipyridine MCCs can have a dramatic effect on the reversibility and number of redox

events, in addition to the solubility, of these complexes. [12] Additionally, it is well established that electron-withdrawing groups shift all redox potentials more positive, and vice versa for electron-donating groups. [16,31] Therefore, functionalization of the BTP ligand scaffold provides a straightforward avenue for tuning the properties of these materials and the results will provide insight that can be applied to other classes of tridentate ligands. To systematically probe the effect of the addition of an electron-withdrawing ester to the 4-position of the pyridine ring, complexes $[Fe(\mathbf{L2})_2](BF_4)_2$, $[Co(\mathbf{L2})_2](BF_4)_2$, and $[Ni(\mathbf{L2})_2](BF_4)_2$ were synthesized. As expected, when compared to the analogous **L1** complexes, the addition of an electron-withdrawing group shifts the redox potentials of both the ligand and metal couples to more positive potentials. This functionalization also results in the appearance of additional negative couples, suggesting these new redox events have either been shifted to within the measurable electrochemical window or that the ester provides an additional site for electron storage. To complete the series, a variation of the BTP ligand was synthesized with an electron-donating pyrrolidine group in the 4-position of the pyridine ring. However, the Fe complex of this ligand was never isolated cleanly, and, while the complex was reduced at more negative potentials, the electrochemistry was highly irreversible. As a result, this functionalization was not applied to any additional metal centers. These design iterations reveal that additional reversible redox couples can be accessed through the addition of an electron-withdrawing group, which is beneficial for the design of multi-electron NAqRFB materials.

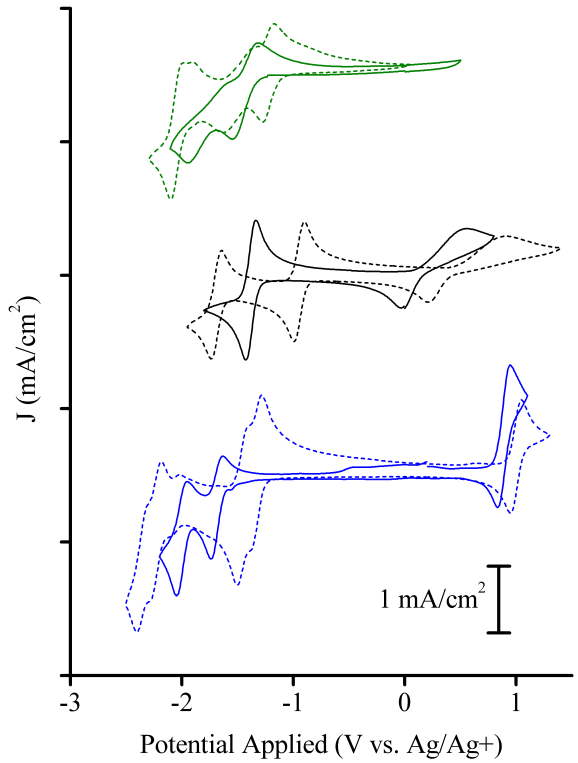

Figure 2.7 Cyclic voltammograms of Fe(**L**)$_2$ (blue), Co(**L**)$_2$ (black), and Ni(**L**)$_2$ (green). For each metal, solid lines correspond to the **L1** complex and dashed lines represent the **L2** analogue.

Of the three metal centers that were tested, the Fe analogues exhibit the best electrochemical properties for use in a single-component NAqRFB; i.e. at least one reversible high- and low-potential redox couple that are separated by a wide voltage window. Furthermore, the low cost, abundance, and inherently low toxicity of Fe make it an ideal metal for large-scale industrial applications. While the modest solubility of [Fe(**L2**)$_2$](BF$_4$)$_2$ in MeCN (193 mM) would limit its applicability in NAqRFBs, simple modification of the 1-alkyl substiutents on the triazole rings can be used to increase complex solubility without detriment to the electrochemical behavior, including the quantity, potential and reversibility the redox events. Indeed, complexes [Fe(**L4**)$_2$](BF$_4$)$_2$ and [Fe(**L5**)$_2$](BF$_4$)$_2$, with polar ethylene glycol ether chains incorporated onto the ligand, demonstrate solubilities of over 600 mM in MeCN.

*2.3.5.2 Iron Complexes of **L3-L6***

Given the desirable electrochemical properties of the Fe(II) complexes bearing ester-substituted BTP ligands, we sought to increase their solubility in MeCN through modification of both the *N1*-substituents on the triazole rings as well as the alkyl substituent on the ester functionality. As mentioned previously, butyl and 2-methoxyethyl chains were selected for this study as they have been shown to enhance the solubility of MCCs in MeCN. [12] Exploiting the modular ligand synthesis described above, we were able to rapidly generate a small library of ligands **L3** – **L6** (Figure 2.6), and, thus, the corresponding bis-ligated Fe(II) tetrafluoroborate complexes, to examine the effects of the incorporation of these functionalities on complex solubility and electrochemistry.

Complexes $[Fe(\mathbf{L3})_2](BF_4)_2$, $[Fe(\mathbf{L4})_2](BF_4)_2$, $[Fe(\mathbf{L5})_2](BF_4)_2$, and $[Fe(\mathbf{L6})_2](BF_4)_2$ range in solubility in MeCN from 553 mM to 769 mM (Table 2.1), demonstrating a significant improvement in solubility over the complex of the methyl-ester substituted ligand $[Fe(\mathbf{L2})_2](BF_4)_2$. An analysis of the electrochemical properties reveals that the electrochemistry of these complexes is nearly identical (Figure 2.8). Each complex exhibits four negative couples that can be associated with the ligand and a single positive couple from the Fe^{II}/Fe^{III} transition. These results reveal the excellent tunability of BTP MCCs, as it is possible to independently vary the electrochemistry and solubility. Taking these trends one step further, we can start to understand the impact of substituent location on both the electrochemical properties and the solubility. In general, the redox potential and reversibility of the redox events are dictated by the metal center and the primary functional group on the pyridine ring, while the triazole substituents and the secondary group on the pyridine predominately affect the solubility. These insights can

be used to further tune these complexes by enabling independent modification of the electrochemical properties and solubilities.

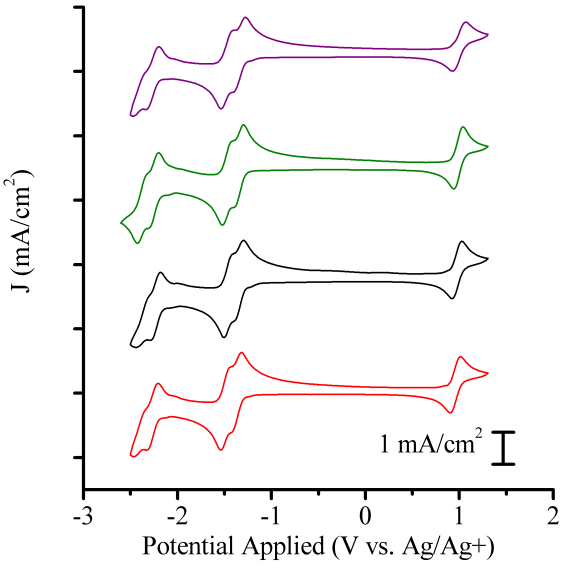

Figure 2.8 Cyclic voltammograms of 5 mM Fe(**L3**)$_2$(BF$_4$)$_2$ (purple), Fe(**L4**)$_2$(BF$_4$)$_2$ (green), Fe(**L5**)$_2$(BF$_4$)$_2$ (black) and Fe(**L6**)$_2$(BF$_4$)$_2$ (red) in MeCN at a scan rate of 100 mV/s.

2.3.6 Electrochemical Stability and Degradation Mechanisms

BTP MCCs are a promising material for NAqRFB applications as they exhibit multiple redox couples and have relatively high solubility. To assess the viability of this chemistry for use as an active species, cyclic BE experiments were performed to quantify the electrochemical stability and identify possible degradation pathways. Potentiostatic cycling experiments were performed in a custom glass H-cell with a porous glass frit separating the working and counter chambers. This set-up avoids the use of a membrane or separator, which can lead to interactions that further convolute stability data. [17] All cycling experiments were performed on Fe(**L4**)$_2$(BF$_4$)$_2$ as it exhibited peak height ratios close to one and a moderately high solubility.

The single positive couple of Fe(**L4**)$_2$(BF$_4$)$_2$ exhibits relatively high stability, with only 18% capacity fade over 50 cycles (Figure 2.9a). A CV after cycling, however, does reveal that the complex is degrading over time (Figure 2.9b). While the positive couple remains relatively unchanged, there is significant degradation observed at negative potentials. Cycling through a single negative electron transfer reveals moderate stability, with 17 cycles before reaching 80% of the initial capacity. These results reveal the possibility of a 1 e^- NAqRFB employing Fe(**L4**)$_2$(BF$_4$)$_2$ as both the anolyte and the catholyte active species. Multi-electron materials are highly desirable, however, so two negative electron transfers were also tested (Figure 2.10a). Unfortunately, Fe(**L4**)$_2$(BF$_4$)$_2$ displays very limited stability past a single electron. After only 10 cycles, the material discharges less than a single electron. In both negative cases, an analysis of the capacity retention reveals that approximately 70% of the active species is charged during cycling. This is due to the tight potential cutoffs used to ensure only the couples of interest were accessed. To understand the cause of the observed capacity fade, CV was used to characterize the electrolyte after cycling through two negative electrons. Ligand dissociation was expected as a degradation pathway and a CV of pure **L4** reveals a characteristic peak at -2.05 V vs Ag/Ag$^+$. As anticipated, a comparison of the CVs for fresh and cycled Fe(**L4**)$_2$(BF$_4$)$_2$ (Figure 2.10b) reveals evidence of ligand shedding after cycling. These results indicate that additional routes must be pursued to further minimize ligand shedding, such as utilizing charged ligands or ligands of higher denticity to further increase the binding strength. With the identification of ligand structures and substituents that provide enhanced stability, the trends presented in this work can be used to readily tailor the electrochemical properties and solubility to achieve promising tridentate MCCs for NAqRFB applications.

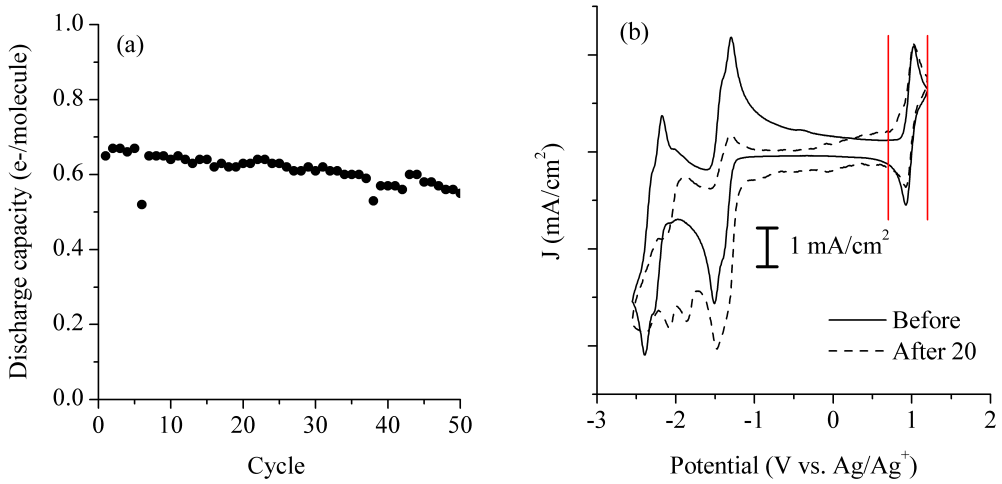

Figure 2.9 (a) Capacity retention of Fe(**L4**)$_2$(BF$_4$)$_2$ cycled through a single positive redox couple. **(b)** CV of Fe(**L4**)$_2$(BF$_4$)$_2$ before cycling (solid) and after 20 cycles (dashed). Solid red lines represent the potential holds used during charge and discharge (1.2 V and 0.70 V respectively).

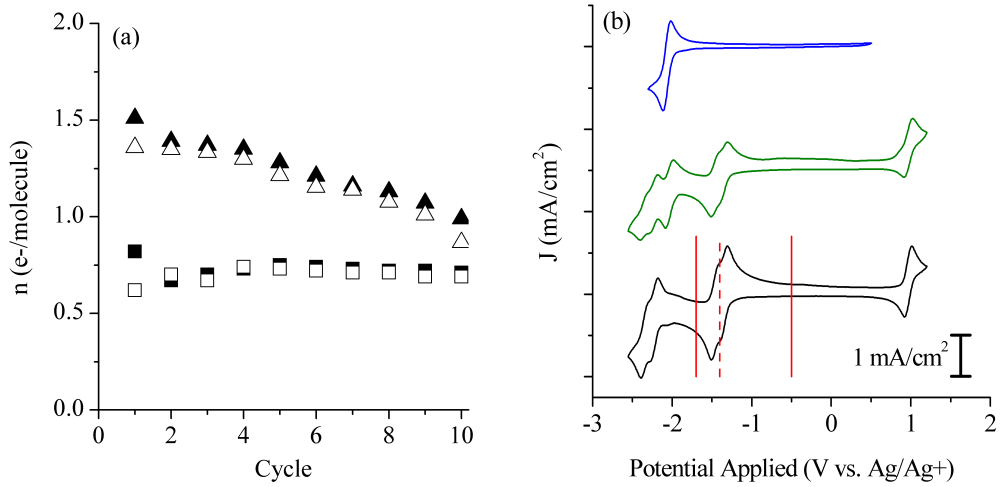

Figure 2.10 (a) Capacity retention of Fe(**L4**)$_2$(BF$_4$)$_2$ through a single negative redox couple (■) and 2 negative redox couples (▲) with charge (filled) and discharge (open) capacities. **(b)** CVs of Fe(**L4**)$_2$(BF$_4$)$_2$ before (black) and after 15 cycles through 2 negative electrons (green) compared to **L4** (blue). Red vertical lines represent the potential holds that were used during charge (-1.0 V) and discharge (-1.42 V and -1.70 V for the 1e$^-$ and 2e$^-$ experiments, respectively).

2.3.7 Extension of Trends to Terpyridine MCCs

To establish that the electrochemical and solubility trends identified for BTP will provide useful input for general molecular design, this work was extended to include an additional class of tridentate ligands. Terpyridine MCCs are a promising class of tridentate active species for NAqRFBs as they exhibit multiple, reversible electron transfers. [32–34] Initial results with terpyridine MCCs indicate that these complexes may offer high stability for NAqRFB applications (see section 2.3.2). However, the solubility of unsubstituted terpyridine MCCs are quite low and despite extensive studies on the electrochemistry of unsubstituted versions, functionalized analogues have not received much attention. For these reasons, terpyridine MCCs are an excellent system to assess the versatility of the trends identified in this work. The goal was to synthesize a terpyridine MCC analogous to Fe(**L4**)$_2$(BF$_4$)$_2$, but due to the complexity of terpyridine synthesis, Fe(**L7**)$_2$(BF$_4$)$_2$ was selected as the target molecule (Figure 2.11a). A CV of Fe(**L7**)$_2$(BF$_4$)$_2$ reveals five reversible redox events (Figure 2.11b), with the single positive couple assigned to a metal-based oxidation and the four negative couples assigned to ligand-based processes. [33] Similar to the BTP complexes (Figure 2.7), the addition of an electron-withdrawing ester group shifted the redox events more positive and resulted in the appearance of two additional negative redox couples. These synthetic modifications successfully increased the solubility to 0.15 M, as compared to 0.1 M for Fe(tpy)$_2$(BF$_4$)$_2$ in MeCN. This is expected to increase even more with the addition of a butyl chain in the R$_1$ position. A BE experiment of the first negative couple of Fe(**L7**)$_2$(BF$_4$)$_2$ reveals impressive stability over 100 cycles (Figure 2.11c), demonstrating that the electrochemistry and solubility of these tridentate MCCs can be modified while maintaining high stability. These exciting results establish that the findings for

the BTP complexes are relevant for other classes of tridentate MCCs and that these trends can be used to guide the design of future NAqRFB active species.

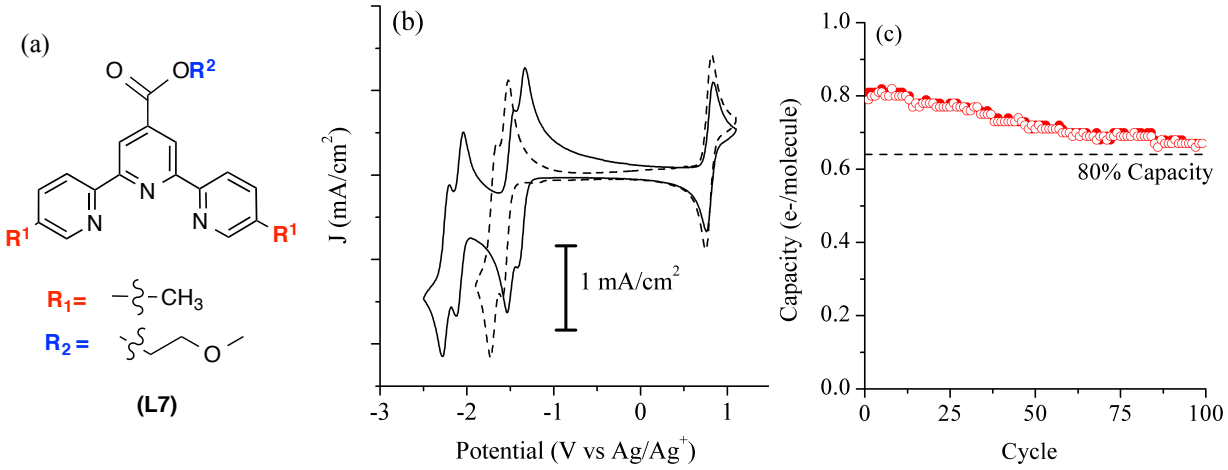

Figure 2.11 (a) Structure of **L7**. **(b)** CV of $Fe(tpy)_2(BF_4)_2$ (dashed) and $Fe(\mathbf{L7})_2(BF_4)_2$ (solid) in MeCN at 100 mV/s. **(c)** Capacity retention plot for a single negative electron transfer with both charge (filled) and discharge (open) capacities. Potential holds were -1.43 V and -1.0 V for charge and discharge, respectively.

2.4 Conclusions

In this work we synthesized a library of tridentate BTP MCCs, implementing systematic ligand variations to identify trends in electrochemical properties and solubility. Analysis of the electrochemical behavior and solubility of each complex revealed that these properties can be tuned independently, highlighting the appeal of tridentate MCCs. In particular, $Fe(BTP)_2$ exhibits properties desirable for NAqRFB applications, with $Fe(\mathbf{L5})_2(BF_4)_2$ demonstrating five reversible redox couples, a solubility > 0.7 M and a functional potential window of 2.32 V. The versatility of these design strategies was demonstrated through the synthesis and characterization of an analogous iron terpyridine complex. The voltammetry results demonstrated that the identified trends in the number and potential of redox features as well as solubility hold for other classes of tridentate ligands. Furthermore, BE experiments showed the promising stability of terpyridine

MCCs, although additional synthetic work is necessary to further increase solubility. Overall, this work established design strategies that can be used to rapidly engineer future MCCs. Active species can first be selected to maximize stability and then synthetically modified to achieve the electrochemical and solubility properties necessary for NAqRFB applications.

2.5 Acknowledgements

I would like to thank Dr. Rachel Brooner from Dr. Melanie Sanford's group at the University of Michigan for her collaborative efforts on this project. She was responsible for synthesizing all of the active species tested in this chapter as well as the solubility measurements.

2.6 References

[1] G.L. Soloveichik, Flow batteries: current status and trends, Chem. Rev. 115 (2014) 11533–11558.

[2] W. Wang, Q. Luo, B. Li, X. Wei, L. Li, Z. Yang, Recent progress in redox flow battery research and development, Adv. Funct. Mater. 23 (2013) 970–986.

[3] W. Kaim, The shrinking world of innocent ligands: conventional and non-conventional redox-active ligands, Eur. J. Inorg. Chem. 2012 (2012) 343–348.

[4] Y. Matsuda, K. Tanaka, M. Okada, U. Takasu, M. Morita, A rechargeable redox battery utilizing ruthenium complexes with non-aqueous organic electrolyte, J. Appl. Electrochem. 18 (1988) 909–914.

[5] M.H. Chakrabarti, L.E.P. Roberts, M. Saleem, Charge-discharge performance of a novel undivided redox flow battery for renewable energy storage, Int. J. Green Energy. 7 (2010) 445–460.

[6] P.J. Cabrera, X. Yang, J.A. Suttil, K.L. Hawthorne, R.E.M. Brooner, M.S. Sanford, L.T. Thompson, Complexes containing redox noninnocent ligands for symmetric, multielectron transfer nonaqueous redox flow batteries, J. Phys. Chem. C. 119 (2015) 15882–15889.

[7] A.E.S. Sleightholme, A.A. Shinkle, Q. Liu, Y. Li, C.W. Monroe, L.T. Thompson, Non-aqueous manganese acetylacetonate electrolyte for redox flow batteries, J. Power Sources. 196 (2011) 5742–5745.

[8] Q. Liu, A.A. Shinkle, Y. Li, C.W. Monroe, L.T. Thompson, A.E.S. Sleightholme, Non-aqueous chromium acetylacetonate electrolyte for redox flow batteries, Electrochem.

Commun. 12 (2010) 1634–1637.

[9] Q. Liu, A.E.S. Sleightholme, A.A. Shinkle, Y. Li, L.T. Thompson, Non-aqueous vanadium acetylacetonate electrolyte for redox flow batteries, Electrochem. Commun. 11 (2009) 2312–2315.

[10] P.J. Cappillino, H.D. Pratt, N.S. Hudak, N.C. Tomson, T.M. Anderson, M.R. Anstey, Application of redox non-innocent ligands to non-aqueous flow battery electrolytes, Adv. Energy Mater. 4 (2014) 1300566.

[11] C.S. Sevov, S.L. Fisher, L.T. Thompson, M.S. Sanford, Mechanism-based development of a low-potential, soluble, and cyclable multielectron anolyte for nonaqueous redox flow batteries, J. Am. Chem. Soc. 138 (2016) 15378–15384.

[12] P.J. Cabrera, X. Yang, J.A. Suttil, R.E.M. Brooner, L.T. Thompson, M.S. Sanford, Evaluation of tris-bipyridine chromium complexes for flow battery applications: Impact of bipyridine ligand structure on solubility and electrochemistry, Inorg. Chem. 54 (2015) 10214–10223.

[13] J.A. Suttil, J.F. Kucharyson, I.L. Escalante-Garcia, P.J. Cabrera, B.R. James, R. F. Savinell, M.S. Sanford, L. Thompson, Metal acetylacetonate complexes for high energy density non-aqueous redox flow batteries, J. Mater. Chem. A. 3 (2015) 7929–7938.

[14] Y. Li, J.C. Huffman, A.H. Flood, Can terdentate 2,6-bis(1,2,3-triazol-4-yl)pyridines form stable coordination compounds?, Chem. Commun. 26 (2007) 2692–2694.

[15] R.M. Meudtner, M. Ostermeier, R. Goddard, C. Limberg, S. Hecht, Multifunctional “clickates” as versatile extended heteroaromatic building blocks: efficient synthesis via click chemistry, conformational preferences, and metal coordination., Chem. Eur. J. 13 (2007) 9834–40.

[16] M. Ostermeier, M.A. Berlin, R.M. Meudtner, S. Demeshko, F. Meyer, C. Limberg, S. Hecht, Complexes of click-derived bistriazolylpyridines: remarkable electronic influence of remote substituents on thermodynamic stability as well as electronic and magnetic properties., Chem. Eur. J. 16 (2010) 10202–10213.

[17] S.H. Shin, S.H. Yun, S.H. Moon, A review of current developments in non-aqueous redox flow batteries: characterization of their membranes for design perspective, RSC Adv. 3 (2013) 9095.

[18] J.M. Friedrich, C. Ponce-de-Leon, G.W. Reade, F.C. Walsh, Reticulated vitreous carbon as an electrode material, J. Electroanal. Chem. 561 (2004) 203–217.

[19] C.S. Sevov, R.E.M. Brooner, E. Chénard, R.S. Assary, J.S. Moore, J. Rodríguez-López, M.S. Sanford, Evolutionary design of low molecular weight organic anolyte materials for applications in nonaqueous redox flow batteries, J. Am. Chem. Soc. 137 (2015) 14465–14472.

[20] J. Huang, L. Su, J.A. Kowalski, J.L. Barton, M. Ferrandon, A.K. Burrell, F.R. Brushett, L. Zhang, A subtractive approach to molecular engineering of dimethoxybenzene-based redox materials for non-aqueous flow batteries, J. Mater. Chem. A. 3 (2015) 14971–14976.

[21] C.S. Sevov, S.K. Samaroo, M.S. Sanford, Cyclopropenium salts as cyclable, high-potential catholytes in nonaqueous media, Adv. Energy Mater. 7 (2016) 1602027.

[22] J.D. Milshtein, A.P. Kaur, M.D. Casselman, J.A. Kowalski, S. Modekrutti, P. Zhang, N.H. Attanayake, C.F. Elliott, S.R. Parkin, C. Risko, F.R. Brushett, S.A. Odom, High current density, long duration cycling of soluble organic active species for non-aqueous redox flow batteries, Energy Environ. Sci. 9 (2016) 3531–3543.

[23] J. England, C.C. Scarborough, T. Weyhermüller, S. Sproules, K. Wieghardt, Electronic structures of the electron transfer Series $[M(bpy)_3]^n$, $[M(tpy)_2]^n$, and $[Fe(t\text{-}bpy)_3]^n$ (M = Fe, Ru; n = 3+, 2+, 1+, 0, 1-): a mössbauer spectroscopic and DFT study, Eur. J. Inorg. Chem. 29 (2012) 4605–4621.

[24] J. Mun, M.-J. Lee, J.-W. Park, D.-J. Oh, D.-Y. Lee, S.-G. Doo, Non-aqueous redox flow batteries with nickel and iron tris(2,2′-bipyridine) complex electrolyte, Electrochem. Solid-State Lett. 15 (2012) A80-A82.

[25] S.M. Laramie, J.D. Milshtein, T.M. Breault, F.R. Brushett, L.T. Thompson, Performance and cost characteristics of multi-electron transfer, common ion exchange non-aqueous redox flow batteries, J. Power Sources. 327 (2016) 681–692.

[26] J. Milshtein, S. Fisher, T. Breault, L. Thompson, F. Brushett, Feasibility of a supporting salt free non-aqueous redox flow battery utilizing ionic active materials, ChemSusChem. 10 (2017) 2080–2088.

[27] J. Huang, L. Cheng, R.S. Assary, P. Wang, Z. Xue, A.K. Burrell, L.A. Curtiss, L. Zhang, Liquid catholyte molecules for nonaqueous redox flow batteries, Adv. Energy Mater. 5 (2015) 1–6.

[28] H.J. Kruger, G. Peng, R.H. Holm, Low-potential nickel(III,II) complexes: new systems based on tetradentate amidate-thiolate ligands and the influence of ligand structure on potentials in relation to the nickel site in [NiFe]-hydrogenases, Inorg. Chem. 30 (1991) 734–742.

[29] N.M. Shavaleev, F. Kessler, M. Grätzel, M.K. Nazeeruddin, Redox properties of cobalt (II) complexes with azole-pyridines, Inorganica Chim. Acta. 407 (2013) 261–268.

[30] C.G. Armstrong, K.E. Toghill, Cobalt(II) complexes with azole-pyridine type ligands for non-aqueous redox-flow batteries: tunable electrochemistry via structural modification, J. Power Sources. 349 (2017) 121–129.

[31] J.R. Wright, K.J. Shaffer, C.J. McAdam, J.D. Crowley, 3,5-diferrocenylpyridine: Synthesis, characterisation, palladium(II) dichloride complex and electrochemistry, Polyhedron. 36 (2012) 73–78.

[32] J.M. Rao, M.C. Hughes, D.J. Macero, Voltammetry of terpyridine and terosine complexes of cobalt (II) and iron (II), Inorganica Chim. Acta. 16 (1976) 231–236.

[33] P.S. Braterman, J.I. Song, R.D. Peacock, Electronic absorption spectra of the iron(II) complexes of 2,2'-bipyridine, 2,2'-bipyrimidine, 1,10-phenanthroline, and 2,2':6',2''-terpyridine and their reduction products, Inorg. Chem. 31 (1992) 555–559.

[34] G.D. Storrier, S.B. Colbran, D.C. Craig, Transition-metal complexes of terpyridine ligands with hydroquinone or quinone substituents, J. Chem. Soc. Dalt. Trans. 3 (1998) 1351–1364.

Chapter 3

Impact of Metal Center and Ligand Structure on the Electrochemical Stability of Metal Coordination Complexes

3.1 Background and Approach

NAqRFBs require electroactive molecules with a combination of three features for optimal performance: (1) redox potentials that exceed the potential limits of water, (2) high solubility, and (3) high stability towards electrochemical cycling. Furthermore, ideal materials would maintain these three properties while cycling over multiple redox couples, thereby providing a proportional increase in storage capacity. However, there are currently no electroactive species that possess all these properties. [1] To enable the efficient design of new active materials that meet these demanding criteria, it will be necessary to first understand the aspects of molecular structure that impact electrochemical reversibility, solubility and cycling stability.

In Chapter 2, I discussed the advantages of using metal coordination complexes (MCCs) as active species in NAqRFBs. Further, bis(triazole)pyridine MCCs were used to identify molecular characteristics that influence the electrochemistry (number of redox events, standard potential, reversibility) and solubility of tridentate complexes. However, after significant developmental efforts it was found that these materials are unstable during electrochemical

cycling. This is also the case for the majority of other classes of MCCs that have been investigated, including acetylacetonate (acac), [2–6] dithiolate, [7] and 2,2'-bipyridine (bpy). [8–16] Each of these complexes typically shows >50% capacity fade after <10 cycles and there is limited information available on the degradation mechanisms resulting in the poor cyclability. As a whole, there is a comprehensive understanding of factors that impact the electrochemistry and solubility of MCCs, but there has yet to be a systematic evaluation of MCC electrochemical stability.

A number of structural properties are expected to impact electrochemical stability. Previous work on acetylacetonate MCCs suggests that metal center will play an important role in determining stability. [3,4,17] Additionally, a comparison of the stability of the various classes of MCCs reported in the literature reveals that the ligand and ligand substituents will also have a significant impact. The first step to systematically investigating electrochemical stability was the selection of a model class of materials. Bipyridylimino isoindoline (BPI) ligands were selected for this work as they exhibit desirable electrochemical properties and are expected to demonstrate high stability due their tridentate, anionic ligand structure. [18] The results presented establish a comprehensive design methodology with a focus on stability. In combination with the results presented in Chapter 2, it will be possible to optimize molecules for stability and then utilize established trends to readily improve their solubility and/or electrochemistry.

In this chapter I will first describe the development of MCCs bearing BPI ligands. To understand the impact of metal center on electrochemical stability, a library of BPI MCCs is synthesized with various metal centers and identical ligand structures. Solubility measurements and cyclic voltammetry (CV) experiments are used to characterize the relevant properties of each

material. Bulk electrolysis (BE) experiments are then used to quantify electrochemical stability. A promising BPI MCC is identified and modifications of the ligand substituents affords a stable complex that exhibits multiple redox couples at negative potentials as well as high solubility in acetonitrile (MeCN). Ultimately, the developed trends will inform the rational design of MCCs that exhibit the combination of cyclability, solubility, and redox potential required for NAqRFB applications. I conclude this chapter with a discussion of ligand characteristics that impact electrochemical stability. These considerations can be used in the selection of future ligand classes as an additional tool for the guided design of viable NAqRFB active species.

3.2 Experimental

3.2.1 Material Synthesis

Reaction solvents and reagents were purchased from commercial sources and used as received. Compounds H**L1** and Ni(**L1**)$_2$ were prepared according to a literature procedure. [18] Synthesis of the 1,3-bis(pyridyl-2-imino)-isoindoline ligands was performed under atmospheric conditions. A round bottom flask was charged with the corresponding phthalonitrile (1.0 equiv), the corresponding 2-aminopyridine (2.5-4.0 equiv), freshly-milled $CaCl_2$ (0.50 equiv), solvent, and a magnetic stir bar. A reflux condenser was attached to the flask, and the flask was placed in an oil bath and brought to reflux while vigorously stirring for 36 h. After this time, the solvent was removed under reduced pressure at 100 °C and the residue was purified by flash chromatography. M**L**$_2$ complexes were synthesized under atmospheric conditions. A screw-capped vial was charged with the appropriate BPI ligand (2.0 equiv), a metal(II) salt MX_2 (1.0 equiv), and a magnetic stir bar. To these solids was added an anhydrous solution of Et_3N in MeOH (10% Et_3N in MeOH v/v). The vial was sealed with a Teflon-lined cap and placed in an

oil bath at 100 °C. The vial was removed from the oil bath after 15 min and was allowed to cool to room temperature while stirring. After 1 h, a crystalline solid formed and was isolated by filtration. The solid was washed with cold (0 °C) MeOH followed by diethyl ether. Residual solvent impurities were removed under high vacuum (50 mTorr, 12 h) to yield the title M**L**$_2$ complex. The general procedure is shown in Figure 3.1. All materials were characterized using NMR, IR, mass spectroscopy and elemental analysis. Full details can be found in the supporting information of [19].

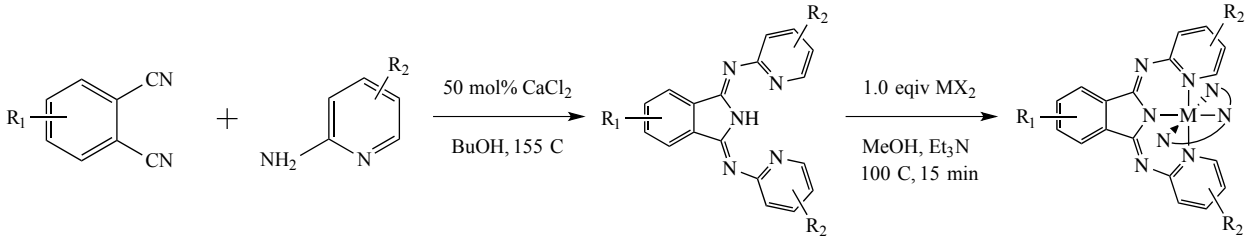

Figure 3.1 General procedure for the modular synthesis of BPI ligands and their metallation.

3.2.2 Solubility Measurements

Solubility studies were performed on the benchtop using a UV-visible method. Stock solutions of each MCC were prepared in MeCN, in triplicate. Serial dilutions of the stock solutions by factors of 2, 4, and 8 were performed in volumetric flasks to prepare standard solutions. A UV-Vis spectrum of the stock solution was recorded and used to determine a suitable wavelength for absorbance measurements. Absorbances of the four solutions were then measured at the determined wavelength and used to prepare a calibration curve of absorbance as a function of concentration. Saturated solutions of the M(BPI)$_2$ complexes were then prepared by portion-wise addition of the desired compound to 500 μL of MeCN, with stirring, until a persistent suspension resulted. This suspension was stirred overnight at room temperature. The

solution was then filtered through cotton wool to remove any undissolved material, and three aliquots were diluted in MeCN to afford absorbances within the range of the calibration curve. The concentration of the dilute solution was calculated based on the absorbances, which allowed for the concentration of the saturated solution to be determined by back-calculation from the Beer-Lambert equation.

3.2.3 Cyclic Voltammetry

Cyclic voltammetry was performed with a BioLogic VSP potentiostat in a three electrode electrochemical cell consisting of a glassy carbon disk working electrode (0.07 cm^2, BASi), a Ag/Ag^+ quasi-reference electrode (BASi) containing 0.01 M $AgBF_4$ (Sigma) in MeCN, and a Pt wire counter electrode. The glassy carbon disk electrode was polished in air using micron aluminum oxide polishing paper (9 micron and 0.3 micron, Fiber Instrument) and water. All experiments were run at a scan rate of 100 mV/s in a MeCN electrolyte containing 2 mM complex and 0.5 M $TBABF_4$.

3.2.4 Bulk Electrolysis

BE studies were carried out in an argon-filled glovebox using a BioLogic VSP potentiostat. Details on the cell configuration can be found in Section 2.2.4. Reticulated vitreous carbon (100 PPI, Duocell) was used as the working electrode with a Pt coil counter electrode and a Ag/Ag^+ quasi-reference electrode that contained 0.01 M $AgBF_4$ in MeCN. BE of the M(**L5**)$_2$ series was performed galvanostatically at a current of 0.54 mA. For the negative studies, potential cutoffs of -2.05 V and -1.4 V were used for charge and discharge, respectively, along with a coulombic cut-off corresponding to 100% SOC. Potential cutoffs for the positive

experiments were selected based on the CVs. The extended cycling study of Ni(**L5**)$_2$ was performed at a constant current of 1.08 mA (2C) with a coulombic cutoff corresponding to 80% SOC. Potential cutoffs were the same as listed previously. A 3 mm diameter GC working electrode (BASi) was used to record CVs before, during and after cycling. Solutions of 2 mM active species in 0.5 M TBABF4 in MeCN were used for all experiments.

3.2.5 Shelf Life Stability

A solution of 0.1 M Ni(**L5**)$_2$ / 0.5 M TBABF$_4$ / MeCN was fully reduced through 2 e^- in a standard BE cell. A constant current of 21.4 mA (1C) was applied with cutoffs of -2.2 V and 100% SOC. After the material was fully charged, it was removed from the cell and placed in a sealed glass vial. Once per day a 200 µL sample was removed and diluted to an active species concentration of 2 mM. A CV of this solution was recorded and the peak height was used to calculate the concentration of Ni(**L5**)$_2$ remaining in solution.

3.3 Results and Discussion

3.3.1 Active Species Selection and Ligand Design

To study the impact of metal center on electrochemical stability it was first necessary to select an appropriate class of MCCs. Most importantly, the MCC needs to have a tridentate ligand scaffold, which has been shown to suppress ligand dissociation (Section 2.3.2). Further, the MCC is required to exhibit multiple, reversible redox events, necessitating the use of a non-innocent ligand. Based on these criteria, BPI MCCs were selected for this study. Prior reports suggest they exhibit electrochemistry of interest for NAqRFB applications. [18] Further, BPI-containing MCCs undergo reduction at the ligand rather than on the metal. [18,20] As such, these

redox-active ligands can serve as reservoirs for multiple electrons and can potentially stabilize the charged complex (since the oxidation state of the metal center remains unchanged during reductive redox processes). Finally, BPI ligands can be prepared via a modular synthesis, which provides rapid access to a diverse library of complexes. Structures of the ligands used in this study are shown in Figure 3.2.

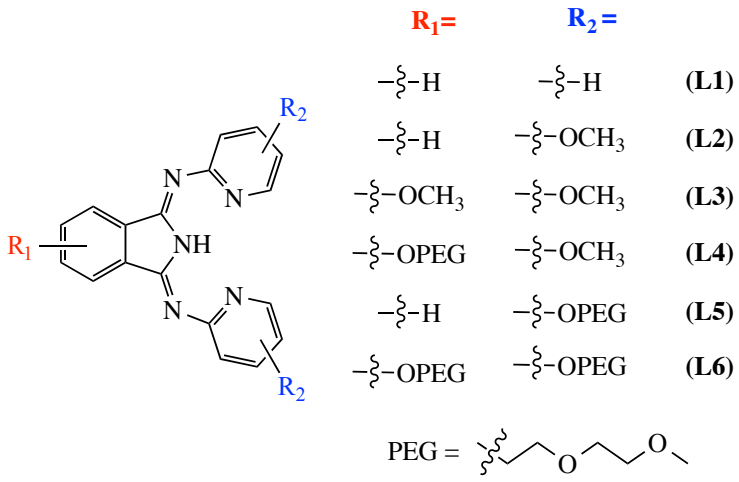

Figure 3.2 Structures of the ligands (**L1 – L6**) studied in this work.

3.3.2 MCC Solubility Measurements

We first evaluated the known compound Ni(**L1**)$_2$ bearing an unsubstituted BPI ligand. [18] As expected for a complex containing a polydentate ligand of high symmetry, [21,22] Ni(**L1**)$_2$ exhibits extremely low solubility (0.42 mM) in MeCN. Our strategy for improving solubility involved decreasing the symmetry of the complexes to disfavor crystal packing [23–26] as well as incorporating alkoxy ether functional groups, which have been shown to enhance the solubility of other MCCs in polar, aprotic solvents (Figure 3.2). [6,15] Notably, in addition to improved solubility, the BPI derivatives functionalized with electron-donating alkoxy substituents exhibit more negative reduction potentials than the parent MCCs, which is

advantageous for applications as anolyte materials.

The solubilities of nickel complexes Ni(**L1-L6**)$_2$ were measured in MeCN and are summarized in Figure 3.3. Modest improvements to solubility were observed upon the incorporation of methoxy substituents (complexes Ni(**L2-3**)$_2$) while derivatives bearing the diethyleneglycoxy (OPEG) substituent (complexes Ni(**L4-6**)$_2$) exhibited solubility enhancements of more than three orders of magnitude versus the parent Ni(**L1**)$_2$. Most notably, Ni(**L6**)$_2$ was isolated as a viscous oil that is miscible with MeCN to form a free-flowing solution of greater than 700 mM concentration. Moreover, a 250 mM solution of Ni(**L6**)$_2$ could be prepared in the presence of 500 mM $TBABF_4$, the concentration of supporting electrolyte required for bulk electrolysis. The presence of supporting electrolyte is known to decrease active species solubility, so it is important to measure solubility at relevant electrolyte compositions (see Section 6.3.2). The dramatic influence of ligand on solubility is exemplified by the low Ni(**L1-3**)$_2$, moderate Ni(**L4-5**)$_2$, and excellent Ni(**L6**)$_2$ solubilities exhibited, which result from only minor perturbations of the peripheral ligand structure.

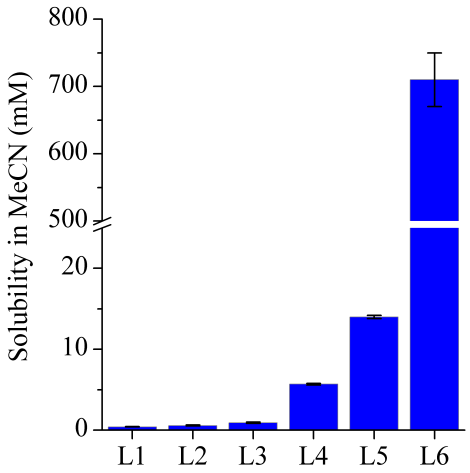

Figure 3.3 Solubility of Ni(**L**)$_2$ complexes in MeCN.

The impact of metal center on MCC solubility was also assessed using a common ligand framework. Comparative studies were performed on complexes of ligands **L4** and **L5**. These were selected because their Ni complexes are only moderately soluble in MeCN (5-15 mM). As such, small variations in solubility as a function of metal cation were easier to detect than with other analogues. MCCs of **L4** and **L5** containing Mg^{2+}, Mn^{2+}, Fe^{2+}, Co^{2+}, Ni^{2+}, and Zn^{2+} were prepared. Single-crystal X-ray structures of the isolated Mn(**L4**)$_2$, Fe(**L4**)$_2$, Ni(**L4**)$_2$, and Zn(**L4**)$_2$ derivatives show pseudo-octahedral geometries with nearly identical unit cells (Figure 3.4).

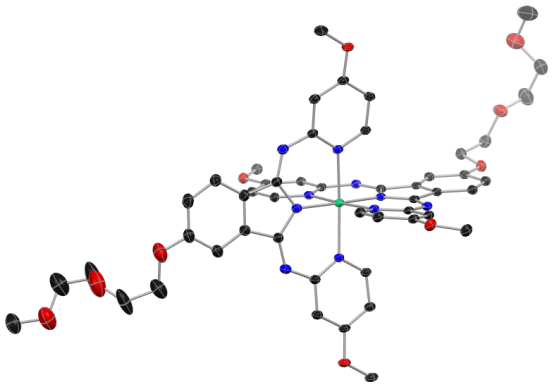

Figure 3.4 Representative crystal structure of Ni(**L4**)$_2$ as determined by x-ray diffraction.

Although these complexes are nearly indistinguishable in the solid-state, their solubilities vary from 8 to 28 mM (Figure 3.5a). A similar trend was observed for complexes of **L5**, in which the Zn and Ni complexes were less soluble than the Mn and Fe analogues by nearly an order of magnitude (Figure 3.5b). The impact of the metal center on the solubility of this MCC series can be rationalized based on the extent of charge shielding by the ligand. [27] Shielding of the metal ion is typically weaker for early versus late transition metals. [28] As a result, MCCs of earlier transition metals are expected to be more polar and thus exhibit higher solubility in polar

solvents like MeCN.

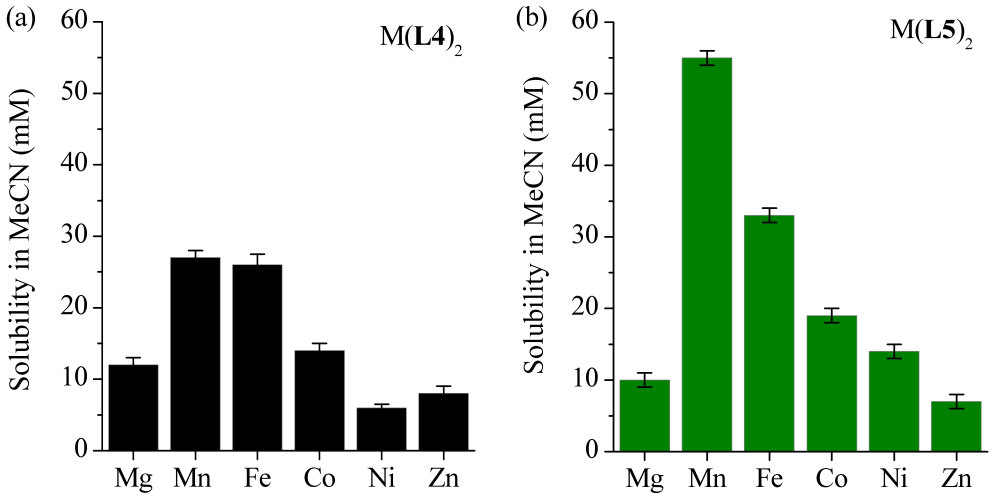

Figure 3.5 Effect of metal center on solubility of complexes with **(a) L4** or **(b) L5**.

3.3.3 Cyclic Voltammetry

We next evaluated the M(**L5**)$_2$ series via CV in MeCN. Each complex exhibits 2 quasi-reversible reductions at approximately -1.7 and -1.9 V vs. Ag/Ag$^+$ (Figure 3.6). These occur at nearly identical redox potentials for all of the MCCs, regardless of the metal center, which is consistent with the reduction involving a ligand-based orbital. Coulometry experiments confirm that each couple corresponds to a single electron transfer. Voltammetry to positive potentials revealed quasi-reversible redox couples for Mn(**L5**)$_2$, Fe(**L5**)$_2$, Co(**L5**)$_2$, and Ni(**L5**)$_2$ at varying potentials. These redox processes are consistent with metal-based M^{II}/M^{III} oxidations. As expected, no analogous couples at positive potentials were observed for complexes of metals that have filled valence shells (e.g., Mg(**L5**)$_2$ and Zn(**L5**)$_2$).

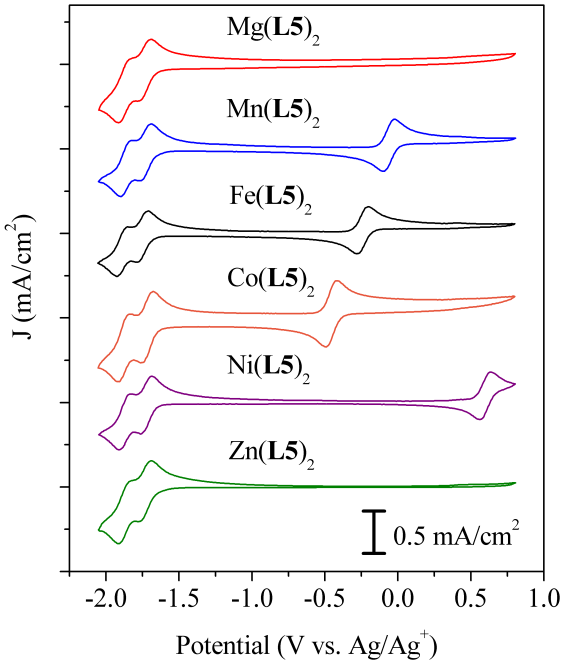

Figure 3.6 Cyclic voltammograms of M(**L5**)$_2$ analogues. Conditions: 2 mM M(**L5**)$_2$ / 0.5 M $TBABF_4$ / MeCN, scan rate of 100 mV/s.

3.3.4 Bulk Electrolysis – Negative Electrochemistry

While the solubility and CV data suggest that the BPI MCCs are promising anolyte candidates, bulk cycling is required to assess their electrochemical stability. To this end, galvanostic charging and discharging of the M(**L5**)$_2$ series was performed in a glass H-cell with an ultrafine glass frit as the separator. A representative data set for Zn(**L5**)$_2$ is shown in Figure 3.7. Voltage cutoffs were selected based on CV (Figure 3.7a) to ensure that only the desired redox couples were accessed during cycling. Charge/discharge cycling was performed through two negative redox couples to 100% state-of-charge (SOC) at 1C (0.54 mA) using 2 mM solutions of the MCCs. The potential curve (Figure 3.7b) during charging exhibits two plateaus (I and II) that are consistent with the redox potentials measured by CV. Discharge occurs with a high voltaic efficiency (90%) at plateaus III and IV. Figure 3.7c displays capacity retention and

coulombic efficiency (CE) as a function of cycle. Zn(**L5**)$_2$ exhibits only moderate stability with fairly rapid capacity fade observed over the first few cycles. The CE increases over the length of the experiment as the capacity, and therefore cycle time, decreases. The average coulombic efficiency (CE) is 94 ± 3%, with losses resulting from degradation and/or crossover of the charged material through the glass frit. Higher CE (97%) was observed using a faster charge rate (2C) due to the reduced time for degradation and/or crossover of the charged species.

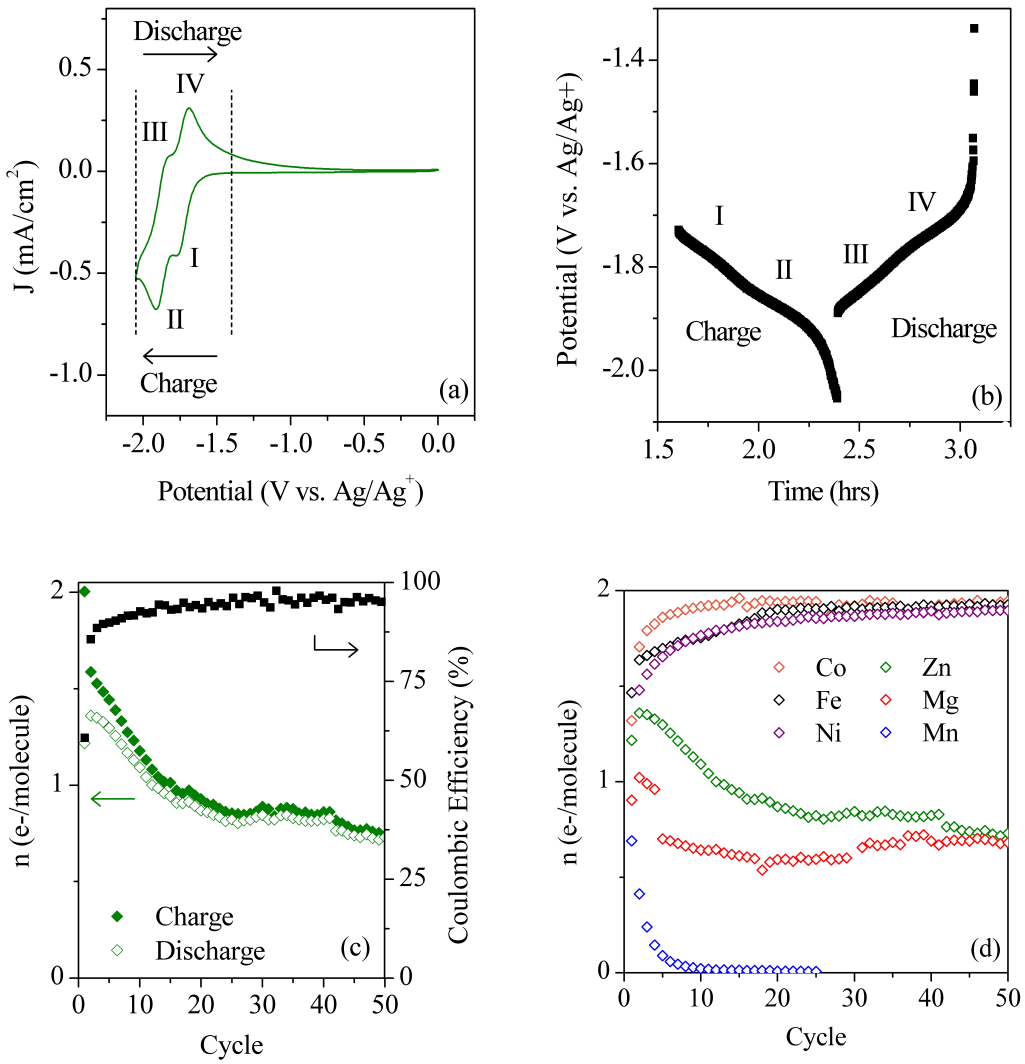

Figure 3.7 (a) CV of Zn(**L5**)$_2$. Dashed lines represent the cutoff potentials used during BE. **(b)** Potential curves for cycle 2 of Zn(**L5**)$_2$ with charge and discharge plateaus labeled I-IV for comparison to the CV half-wave potentials. **(c)** Charge and discharge capacities for Zn(**L5**)$_2$ along with coulombic efficiency as a function of cycle. **(d)** Discharge capacity, normalized to the theoretical number of electrons charged, for each complex in the M(**L5**)$_2$ series. All experiments were performed in MeCN at an active species concentration of 2 mM.

Identical BE studies were performed on the remainder of the M(**L5**)$_2$ series to assess the contribution of metal center on the charge/discharge stability of MCCs. It was found that the identity of the metal has a profound effect on electrochemical stability (Figure 3.7d). For

example, while the filled shell Zn(**L5**)$_2$ and Mg(**L5**)$_2$ complexes showed only modest stability (~50% decomposition over 50 cycles), complexes of metals with partially-filled d-orbitals exhibited dramatically different cycling profiles. The early transition metal complex Mn(**L5**)$_2$ showed extremely rapid fade of energy storage capacity (complete decomposition in less than 10 cycles). In contrast, complexes of the later transition metals Ni(**L5**)$_2$, Co(**L5**)$_2$, and Fe(**L5**)$_2$ exhibited no detectable loss of storage capacity over 50 charge-discharge cycles to 100% SOC through two electrons. These complexes provide the first examples of stable, multielectron cycling of MCC electrolytes for NAqRFBs. The dramatic changes in stability as a function of metal are particularly noteworthy because (i) the negative redox events are believed to be ligand-based and (ii) these complexes exhibit nearly identical electrochemical behavior at negative potentials when evaluated by CV.

A preliminary investigation on the impact of ligand substituent on electrochemical stability was also performed. Figure 3.8 compares the performance of Ni(**L4**)$_2$ and Ni(**L5**)$_2$ through two negative e^- under identical conditions. This data reveals that variation of the ligand had a minimal impact on capacity retention. Interestingly, this illustrates that it is possible to enhance solubility while still maintaining excellent electrochemical stability. However, it should be noted that the ligand structures are substantially similar. More dramatic changes are expected with the introduction of different types of functionalities.

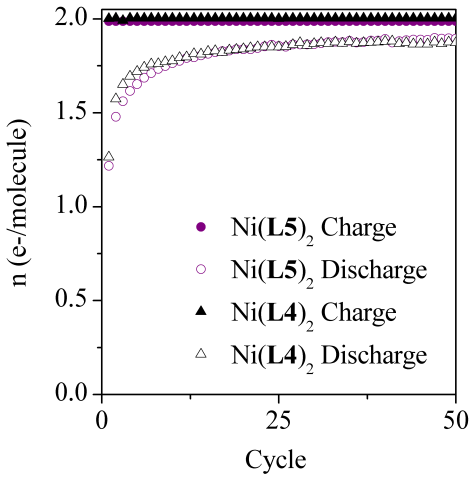

Figure 3.8 Comparative BE of Ni(**L4**)$_2$ (▲) and Ni(**L5**)$_2$ (●) through two negative e$^-$ showing both charge (open) and discharge (filled) capacities.

3.3.5 Degradation Mechanisms and Stability Trends

To gain further insight into the decomposition pathways, CVs of the relatively unstable Zn, Mg and Mn complexes were measured before (dashed traces) and after (solid traces) 25 BE cycles. After cycling, all CVs exhibit an irreversible oxidation at approximately +0.5 V (Figure 3.9). It is highly unlikely that this new peak results from a metal-based oxidation of a decomposed Mg^{2+} or Zn^{2+} species as oxidation of Mg(II) or Zn(II) is unlikely to occur at such low potentials. Instead, we hypothesize that it involves oxidation of the free ligand or a ligand fragment, as BPI ligands are electrochemically active.

The immediate organic product of ligand dissociation under the anhydrous conditions of BE would be anionic **L5**$^-$ with a TBA^+ (TBA = tetrabutylammonium) counterion derived from the supporting electrolyte. To generate a sample of this material, we subjected the free ligand (**HL5**) to reductive electrolysis in a $TBA^+BF_4^-$ supporting electrolyte, which is expected to form **TBA$^+$L5**$^-$ with concomitant loss of H_2. Complete consumption of **HL5** was confirmed by CV based on the disappearance of the cathodic peak at -1.7 V (Figure 3.9 trace *iv* to *v*). A CV of the

species formed after bulk electrolysis shows a peak at -2.3 V, which we attribute to reduction of **L5**$^{-}$ to **L5**$^{2-}$. The corresponding oxidation of **L5**$^{2-}$ occurs at a much higher potential of -1.3 V. Most importantly, an additional irreversible peak is observed at positive potential (+0.5 V), corresponding to the **L5**$^{-}$/**L5**$^{\bullet}$ couple. This peak is the same as that observed in the CVs following cycling of the Zn and Mg MCCs. Furthermore, when a CV of **L5**$^{-}$ was measured with an identical voltage window to the MCCs, only the irreversible peak at +0.5 V was recorded (Figure 3.9 trace *vi*). Collectively, these data suggest that the oxidative peak observed after MCC decomposition results from oxidation of the free ligand **L5**$^{-}$ to neutral **L5**$^{\bullet}$, while oxidation of the neutral **HL5** requires potentials beyond the measured CV window (Figure 3.9 trace *iv*).

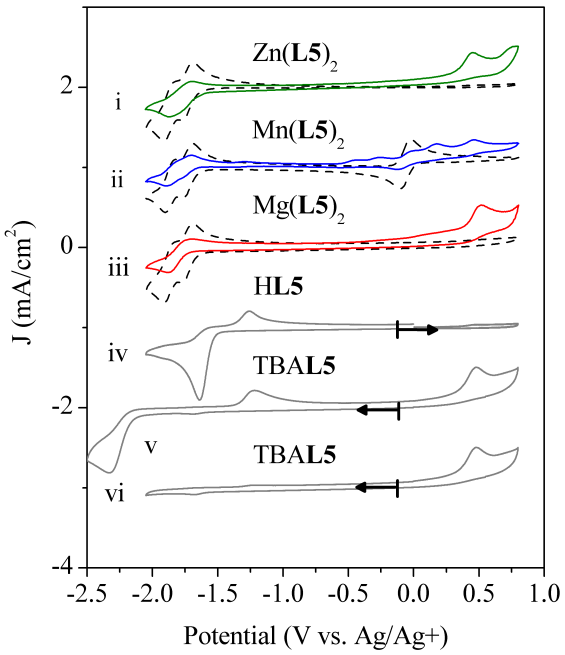

Figure 3.9 CVs of unstable MCCs before (dashed, black traces) and after (solid, colored traces) cycling studies compared to free ligand. Gray dashed lines represent the axis of origin. Arrows denote starting point and scanning direction.

These results provide evidence for the presence of free ligand in solution, and thus support the hypothesis that ligand shedding plays a major role in MCC decomposition. An

understanding of the decomposition mechanism and rate as a function of metal will guide the design of future generations of anolyte materials. Our cycling studies reveal that complexes of Fe^{2+}, Co^{2+}, and Ni^{2+} are significantly more stable anolytes than those of Mg^{2+}, Mn^{2+}, and Zn^{2+}. The large effect of metal on stability correlates well with the rates of ligand exchange at divalent transition and main group metals. [29] Metals with filled shells such as Mg^{2+} or Zn^{2+} lack ligand-field interactions, resulting in rapid rates of dissociative ligand substitution. [30] Conversely, metals with partially-filled orbitals such as Mn^{2+}, Fe^{2+}, Co^{2+}, or Ni^{2+} form complexes that are far less susceptible to dissociative ligand substitution. However, unlike the complexes of the late transition metals, ligand substitution at many octahedral complexes of Mn^{2+} has been shown to occur predominantly by an associative mechanism. [31] As a result, the exchange of MeCN at $Mn(MeCN)_6^{2+}$ is 10,000 times faster than at $Ni(MeCN)_6^{2+}$, and the rates of ligand exchange increase in the order $Ni^{2+} < Co^{2+} < Fe^{2+} <<< Mn^{2+}$. [29] Overall, our results highlight an inverse correlation between the rate of ligand exchange and stability during cycling. More generally, because the predominant mechanisms of ligand exchange at different metals have been extensively studied, [29,32–34] these insights provide a guide to improving the electrochemical stability of a given MCC by targeting and inhibiting the known pathway for ligand exchange at that specific metal.

3.3.6 Extended Cycling and Shelf-Life Stability

With the identification of a stable MCC, the next step was to conduct extended cycling studies to more thoroughly assess the lifetime. Our stability studies provided invaluable guidance in selecting a MCC for the extended cycling experiment. Ligand exchange at octahedral Ni^{2+} occurs with relatively slow rates via a dissociative mechanism, which suggests that $Ni(BPI)_2$

complexes should exhibit particularly high cycling stability. Thus, Ni(**L5**)$_2$ was chosen for extended cycling to the commercial standard of 80% SOC. [35] The results from these studies are summarized in Figure 3.10a and demonstrate that this complex can be cycled through two electrons with <5% capacity fade after 200 cycles. Charge and discharge curves after 100 cycles, illustrated in Figure 3.10b, indicate that the Ni(**L5**)$_2$ complex is charging through two couples at the expected potentials and discharging with high CE (97%).

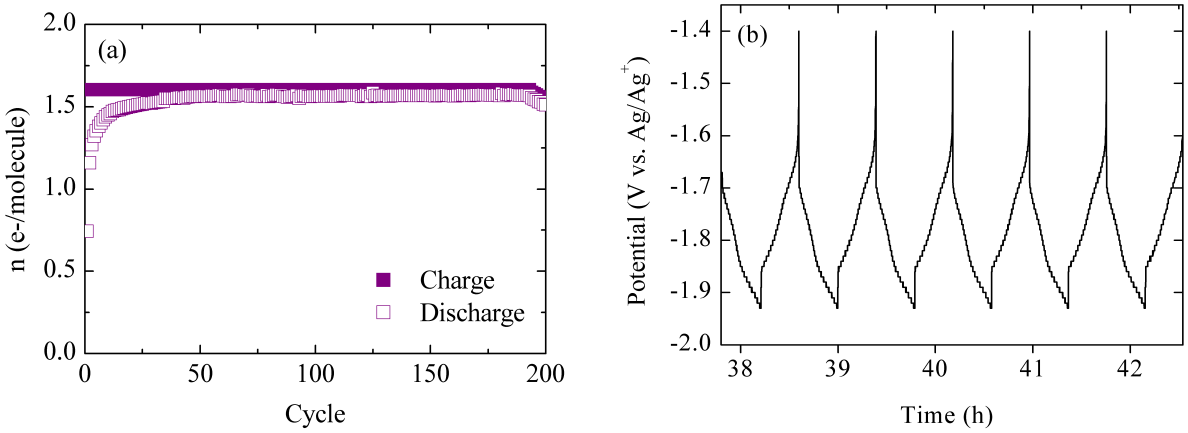

Figure 3.10 (a) Capacity retention of Ni(**L5**)$_2$ at a concentration of 2 mM. **(b)** Potential curves for cycles 100-105.

In parallel with these multi-electron cycling studies, we investigated the shelf-stability of the charged MCC at high concentration. A 0.1 M solution of Ni(**L6**)$_2$ in MeCN was prepared with 0.5 M $TBABF_4$ supporting electrolyte. This concentration is comparable to high concentration studies performed on NAqRFB chemistries in flow. [36,37] Galvanostatic charging of this high-concentration solution was used to generate a solution of fully reduced Ni(**L6**)$_2$. As shown in Figure 3.11a, the charging occurred at potentials that correlate well with peaks observed by CV (-1.8 V, -2.0 V). An ohmic resistance contribution of 4 Ω was measured

by electrochemical impedance spectroscopy, which is consistent with the low overpotentials observed during electrolysis. Once charged, the solution was removed from the H-cell and stored in a separate glass container under inert conditions at room temperature. The concentration of the charged MCC was then measured as a function of time. The results are plotted in Figure 3.11b. The doubly-reduced MCC remains stable and soluble in the electrolyte solution for weeks at high concentration (0.1 M) without significant degradation or precipitation. Further, the CVs used to measure the concentration of Ni(**L6**)$_2$ in solution (Figure 3.11c) reveal that the electrochemical behavior of the material is consistent over the two week period.

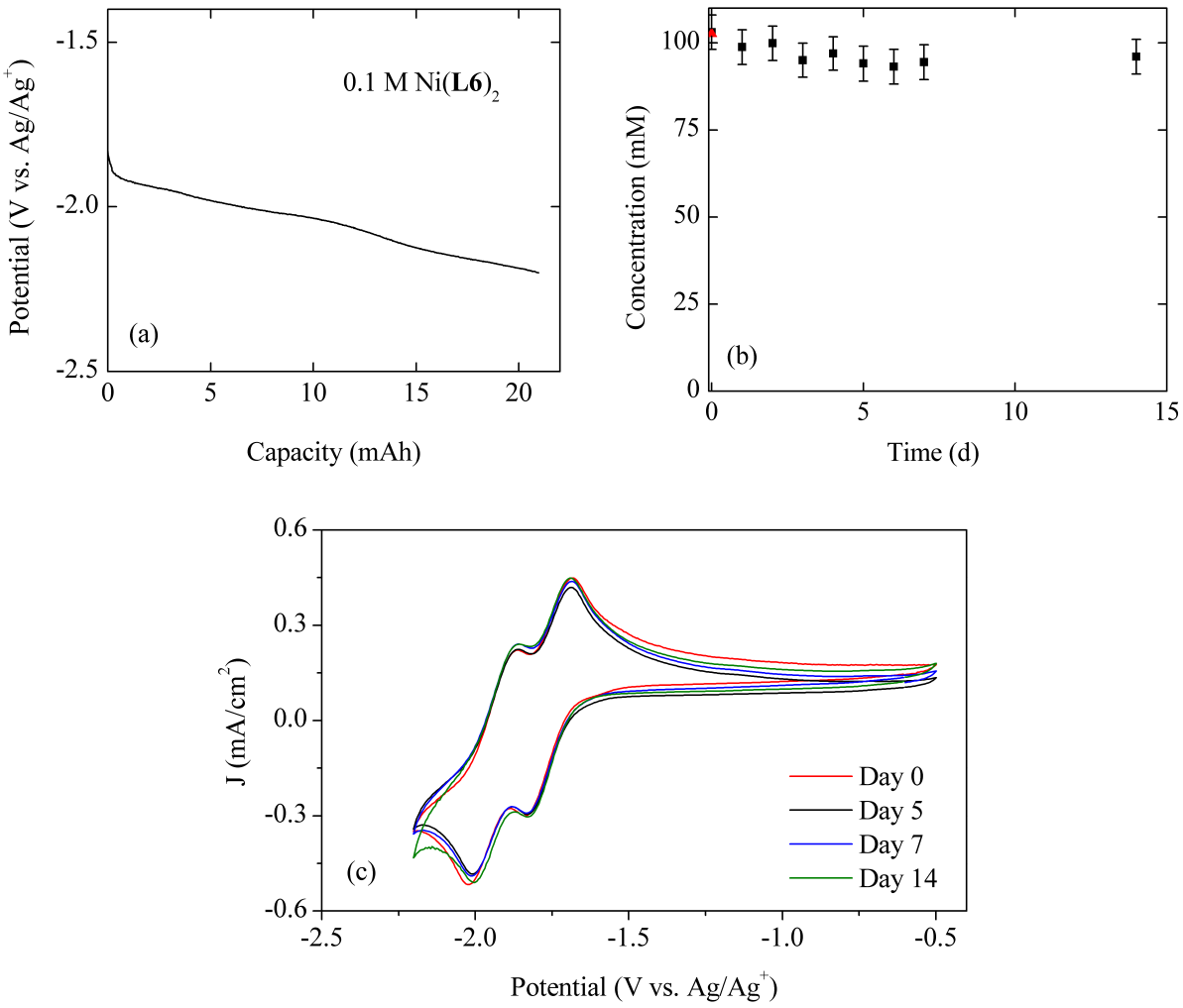

Figure 3.11 (a) Charging potential curve for the $2e^-$ reduction of a 0.1 M solution of Ni(**L6**)$_2$. **(b)** Concentration of the charged Ni(**L6**)$_2$ as a function of time as measured by CV. The red triangle represents the concentration of the neutral solution before cycling. **(c)** CVs of the charged solution over time.

3.3.7 Bulk Electrolysis - Positive Couple

To provide a comprehensive analysis of BPI performance, the electrochemical stability of the most positive couple for each MCC was also quantified using BE. These experiments were performed at a current identical to that for the negative studies, but the potential cutoffs were varied to cycle the appropriate couple. Results are shown in Figure 3.12 for Mn, Fe, Co and Ni. Zn and Mg did not exhibit a positive redox event and are therefore not included in this study.

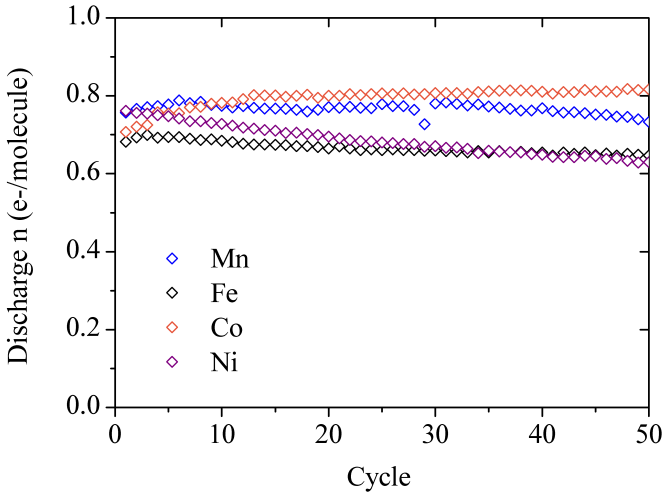

Figure 3.12 Capacity retention of the M(**L5**)$_2$ series through the positive-most redox event. Experiments were performed at a constant current of 0.54 mA (2C) with potential cutoffs selected based on the standard potential observed by CV. Mn: -0.25 V and 0.35 V, Fe: -0.5 V and 0.1 V, Co: -0.7 V and - 0.1 V, Ni: 0.4 V and 0.8 V.

Analysis of the capacity retention plot reveals that the positive-most couple of each M(**L5**)$_2$ complex exhibits high stability through 50 cycles. In all cases the capacity is limited to <80% of the theoretical capacity as a result of the relatively fast charging rate. To maintain an equivalent current, these studies were performed at a C-rate of 2C, instead of the 1C used for the negative studies. The capacity retention after 50 cycles is displayed in Table 3.1 along with the standard potential of each couple being cycled. A comparison of these values reveals a general correlation between electrochemical stability and redox potential. As the standard potential increases, the electrochemical stability decreases. Since a high cell potential is attractive for NAqRFB applications this trend is not ideal, however, the stability of Co, Fe and Mn are excellent and all are promising catholyte materials. The poor performance of Ni(**L5**)$_2$ can be further explained by the instability of Ni(III) complexes. [38]

Table 3.1 Standard potential and capacity retention for the M(**L5**)$_2$ series.

	Standard Potential (V vs. Ag/Ag$^+$)	**Capacity Retention 50 Cycles (%)**
Co(**L5**)$_2$	-0.33	99
Fe(**L5**)$_2$	-0.20	93
Mn(**L5**)$_2$	0.03	96
Ni(**L5**)$_2$	0.60	82

3.3.8 Stability Across All Ligand Classes

Over the past few years, significant efforts have focused on the development of MCCs as NAqRFB active species. While these studies offer an assessment of the stability of each individual material, it would be highly useful to identify general ligand characteristics that afford high electrochemical stability. This understanding could then be used in conjunction with the stability relationships previously discussed to quickly identify promising new MCCs. A few ligand related factors that are expected to impact electrochemical stability include denticity, metal-ligand bond strength, heteroatom and charge distribution. Figure 3.13 shows the structures of the ligands that will be used in this work to investigate the relationship between ligand structure and electrochemical stability. Table 3.2 lists the cycle life of each material, measured using bulk electrolysis. Each entry reports the cycling stability through one or two negative electron transfers. These redox events are associated primarily with ligand-centered processes and should therefore represent the impact of the ligand on cycling stability. It should be noted that the identified trends hold for both cases, with the electrochemical stability decreasing as the number of e^- transfers increases. Fe was selected as the metal center as data was available for all of the ligand classes.

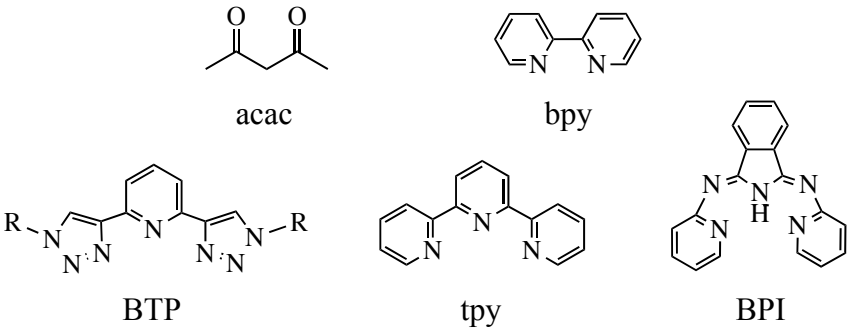

Figure 3.13 Ligand structures.

Table 3.2 Cycle life of studied Fe MCCs through one or two negative redox events.

	Cycles to 80% Capacity ($1e^-$)	**Cycles to 80% Capacity ($2e^-$)**	**Concentration (mM)**
$Fe(bpy)_3(BF_4)_2$	8	5	5
$Fe(tpy)_2(BF_4)_2$	> 50	-	5
$Fe(BTP)_2(BF_4)_2$	18	8	5
$Fe(BPI)_2$	-	> 100	2
$Fe(acac)_3$ [39]	97	-	10

As discussed in Section 2.3.2, higher denticity ligands afford higher electrochemical stability. This relationship is demonstrated with the first two entries in Table 3.2, where tridentate $Fe(tpy)_2(BF_4)_2$ is significantly more stable than its bidentate counterpart, $Fe(bpy)_3(BF_4)_2$. $Fe(tpy)_2(BF_4)_2$ has a shorter average Fe-N bond length, [40] indicating that the ligand is more strongly bound to the metal center, which helps suppress ligand dissociation. A comparison of the stabilities of all the studied tridentate ligands (tpy, BTP, BPI) reveals that they are all more stable than bpy. However, there are considerable variations within the stabilities of the tridentate ligands, indicating there are other structural factors to consider. It is also important to note that not all the MCCs align with this trend. The final entry in Table 3.2 shows the stability of

bidentate $Fe(acac)_3$, which is more stable than a majority of the tridentate MCCs. This discrepancy is reconciled when considering the degradation mechanism of acac MCCs. Although not well understood, it has been established that ligand shedding is not the primary degradation mechanism for $Fe(acac)_3$. [39] As a result, the binding strength of the ligand likely plays a less dominant role in determining stability. This emphasizes that to develop meaningful relationships between structure and cycling stability, it will initially be necessary to group MCCs by their degradation pathways. Once a more detailed understanding of MCC decomposition is available, it may be possible to reconcile these data sets and develop a comprehensive structure-stability relationship. For this work, bpy, tpy, BTP, and BPI have all been shown to suffer from ligand shedding during electrochemical cycling and the remainder of this discussion will focus on those four classes of materials.

With ligand dissociation acting as the primary degradation pathway, high electrochemical stability is expected to correlate with more strongly bound ligands. A comparison of the cycling stability of BTP and tpy reveals that tpy is more stable. This variation can be explained by considering the bond strength differences between pyridine and triazole rings. Measured bond dissociation energies for the ring and alkali metal ions reveal that pyridine has a notably higher energy than triazole in all cases. [41,42] Although not specifically for transition metals, these trends would be expected to hold for Fe and help explain the higher stability observed for tpy. Continuing through the table, BTP provides even higher stability than tpy. BTP is an anionic ligand and the charge on the ligand provides a 'charge assisted' component to the bond, strengthening it even further. [43] Additionally, BPI ligands form six-membered chelate rings, which for small metal ions are more stable than the five-membered chelate rings formed by tpy and BTP. [44]

As a whole, these results start to reveal the structural characteristics required for an MCC to achieve high cycling stability. In general, high denticity, anionic ligands composed of rings with high bond dissociation energies are desirable. However, the data set used was small and only relevant for MCCs that decompose through ligand dissociation. Further investigation would provide valuable insight and result in more general design guidelines. To expand these studies it would be of interest to investigate ligands of even higher denticity. Further, it would be valuable to include a wider variety of heteroatoms, such as S and O. A more comprehensive, systematic investigation of various ligand structures could provide extremely valuable information on the structural characteristics that contribute to high cycling stability.

3.4 Conclusions

In summary, this chapter described the development of a series of tridentate BPI MCCs. Systematic modification of the BPI metal center revealed strong correlations between MCC electrochemical stability and structural characteristics. At negative potentials, the stability trends were explained using known rates of ligand substitution at divalent metal centers. As these properties are dependent solely on the metal center, these trends are expected to be widely applicable to all class of MCCs. In regards to the viability of these materials, BPI complexes of nickel were remarkably stable and completed 200 charge and discharge cycles through two reductions with <5% capacity fade. Ultimately these studies led to the identification of Ni(**L6**)$_2$, a complex that possesses the previously unprecedented combination of high solubility, multiple electron transfers at low redox potentials, and high stability in the charged state, even at high concentration. Overall, the studies described herein have delivered a promising anolyte candidate for NAqRFBs and have also provided key insights into chemical design principles for future

classes of MCC-based active species.

3.5 Acknowledgements

I would like to thank Dr. Christo Sevov from Dr. Melanie Sanford's group at the University of Michigan for his collaborative efforts on this project. He was responsible for synthesizing all of the active species tested in this chapter as well as the solubility measurements.

3.6 References

[1] G.L. Soloveichik, Flow batteries: current status and trends, Chem. Rev. 115 (2014) 11533–11558.

[2] D. Zhang, H. Lan, Y. Li, The application of a non-aqueous bis(acetylacetone)ethylenediamine cobalt electrolyte in redox flow battery, J. Power Sources. 217 (2012) 199–203.

[3] Q. Liu, A.E.S. Sleightholme, A.A. Shinkle, Y. Li, L.T. Thompson, Non-aqueous vanadium acetylacetonate electrolyte for redox flow batteries, Electrochem. Commun. 11 (2009) 2312–2315.

[4] A.E.S. Sleightholme, A.A. Shinkle, Q. Liu, Y. Li, C.W. Monroe, L.T. Thompson, Non-aqueous manganese acetylacetonate electrolyte for redox flow batteries, J. Power Sources. 196 (2011) 5742–5745.

[5] T. Yamamura, Y. Shiokawa, H. Yamana, H. Moriyama, Electrochemical investigation of uranium b-diketonates for all-uranium redox flow battery, Electrochim. Acta. 48 (2002) 43–50.

[6] J.A. Suttil, J.F. Kucharyson, I.L. Escalante-Garcia, P.J. Cabrera, B.R. James, R. F. Savinell, M.S. Sanford, L. Thompson, Metal acetylacetonate complexes for high energy density non-aqueous redox flow batteries, J. Mater. Chem. A. 3 (2015) 7929–7938.

[7] P.J. Cappillino, H.D. Pratt, N.S. Hudak, N.C. Tomson, T.M. Anderson, M.R. Anstey, Application of redox non-innocent ligands to non-aqueous flow battery electrolytes, Adv. Energy Mater. 4 (2014) 1300566.

[8] X. Xing, D. Zhang, Y. Li, A non-aqueous all-cobalt redox flow battery using 1,10-phenanthrolinecobalt (II) hexafluorophosphate as active species, J. Power Sources. 279 (2015) 205–209.

[9] M.S. Park, N.J. Lee, S.W. Lee, K.J. Kim, D.J. Oh, Y.J. Kim, High-energy redox-flow batteries with hybrid metal foam electrodes, ACS Appl. Mater. Interfaces. 6 (2014)

10729–35.

[10] M.H. Chakrabarti, R.A.W. Dryfe, E.P.L. Roberts, Evaluation of electrolytes for redox flow battery applications, Electrochim. Acta. 52 (2007) 2189–2195.

[11] M.H. Chakrabarti, L.E.P. Roberts, M. Saleem, Charge-discharge performance of a novel undivided redox flow battery for renewable energy storage, Int. J. Green Energy. 7 (2010) 445–460.

[12] M. Morita, Y. Tanaka, K. Tanaka, Y. Matsuda, T. Matsumura-Inoue, Electrochemical oxidation of ruthenium and iron complexes at rotating ring disk electrode in acetonitrile solution, Chem. Soc. Japan. 61 (1988) 2711–2714.

[13] Y. Matsuda, K. Tanaka, M. Okada, U. Takasu, M. Morita, A rechargeable redox battery utilizing ruthenium complexes with non-aqueous organic electrolyte, J. Appl. Electrochem. 18 (1988) 909–914.

[14] J. Mun, M.J. Lee, J.W. Park, D.J. Oh, D.Y. Lee, S.G. Doo, Non-aqueous redox flow batteries with nickel and iron tris(2,2′-bipyridine) complex electrolyte, Electrochem. Solid-State Lett. 15 (2012) A80–A82.

[15] P.J. Cabrera, X. Yang, J.A. Suttil, R.E.M. Brooner, L.T. Thompson, M.S. Sanford, Evaluation of tris-bipyridine chromium complexes for flow battery applications: Impact of bipyridine ligand structure on solubility and electrochemistry, Inorg. Chem. 54 (2015) 10214–10223.

[16] P.J. Cabrera, X. Yang, J.A. Suttil, K.L. Hawthorne, R.E.M. Brooner, M.S. Sanford, L.T. Thompson, Complexes containing redox noninnocent ligands for symmetric, multielectron transfer nonaqueous redox flow batteries, J. Phys. Chem. C. 119 (2015) 15882–15889.

[17] Q. Liu, A.A. Shinkle, Y. Li, C.W. Monroe, L.T. Thompson, A.E.S. Sleightholme, Non-aqueous chromium acetylacetonate electrolyte for redox flow batteries, Electrochem. Commun. 12 (2010) 1634–1637.

[18] R.R. Gagne, W.A. Marritt, D.N. Marks, W. Siegllb, Mononuclear and binuclear metal complexes of 1,3-bis(2-pyridylimino)isoindolines, Inorg. Chem. 20 (1981) 3260–3267.

[19] C.S. Sevov, S.L. Fisher, L.T. Thompson, M.S. Sanford, Mechanism-based development of a low-potential, soluble, and cyclable multielectron anolyte for nonaqueous redox flow batteries, J. Am. Chem. Soc. 138 (2016) 15378–15384.

[20] R. Csonka, G. Speier, J. Kaizer, Isoindoline-derived ligands and applications, RSC Adv. 5 (2015) 18401–18419.

[21] D.H. Freeman, I.D. Swahn, P. Hambright, Spectrophotometry and solubility properties of nickel and vanadyl porphyrin complexes, Energy & Fuels. 4 (1990) 699–704.

[22] X. Huang, K. Nakanishi, N. Berova, Porphyrins and metalloporphyrins: Versatile circular dichroic reporter groups for structural studies, Chirality. 12 (2000) 237–255.

[23] M. Ishikawa, Y. Hashimoto, Improvement in aqueous solubility in small molecule drug discovery programs by disruption of molecular planarity and symmetry, J. Med. Chem. 54

(2011) 1539–1554.

[24] T. Takeuchi, S. Oishi, M. Kaneda, H. Ohno, S. Nakamura, I. Nakanishi, M. Yamane, J. Sawada, A. Asai, N. Fujii, Kinesin spindle protein inhibitors with diaryl amine scaffolds: crystal packing analysis for improved aqueous solubility, ACS Med. Chem. Lett. 5 (2014) 566–571.

[25] R. Docherty, K. Pencheva, Y.A. Abramov, Low solubility in drug development: de-convoluting the relative importance of solvation and crystal packing, J. Pharm. Pharmacol. 67 (2015) 847–856.

[26] S. Ozaki, Y. Nakagawa, O. Shirai, K. Kano, Substituent effect on the thermodynamic solubility of structural analogs: relative contribution of crystal packing and hydration, J. Pharm. Sci. 103 (2014) 3524–3531.

[27] W.H. Teoh, R. Mammucari, N.R. Foster, Solubility of organometallic complexes in supercritical carbon dioxide: A review, J. Organomet. Chem. 724 (2013) 102–116.

[28] O. Aschenbrenner, S. Kemper, N. Dahmen, K. Schaber, E. Dinjus, Solubility of β-diketonates, cyclopentadienyls, and cyclooctadiene complexes with various metals in supercritical carbon dioxide, J. Supercrit. Fluids. 41 (2007) 179–186.

[29] L. Helm, A.E. Merbach, Inorganic and bioinorganic solvent exchange mechanisms, Chem. Rev. 105 (2005) 1923–1959.

[30] S. Nakamura, S. Meiboom, Proton magnetic resonance studies of the solvation shell of Mg2+ in methanol. Solvation number and exchange rate, J. Am. Chem. Soc. 89 (1967) 1765–1772.

[31] Y. Inada, T. Sugata, K. Ozutsumi, S. Funahashi, Solvation structures and kinetics of solvent exchange reactions of the manganese(II) ion in six nitriles as studied by X-ray diffraction, EXAFS, and NMR techniques, Inorg. Chem. 37 (1998) 1886–1891.

[32] S.F. Lincoln, A.E. Merbach, Substitution reactions of solvated metal ions, in: Adv. Inorg. Chem., Academic Press, 1995.

[33] R. Hogg, R.G. Wilkins, Exchange studies of certain chelate compounds of the transitional metals. Part VIII. 2,2′,2″-terpyridine complexes, J. Chem. Soc. 0 (1962) 341–350.

[34] R.H. Holyer, C.D. Hubbard, S.F.A. Kettle, R.G. Wilkins, The kinetics of replacement reactions of complexes of the transition ,metals with 1,10-phenanthroline and 2,2'-bipyridine, Inorg. Chem. 4 (1965) 929–935.

[35] L. Li, S. Kim, W. Wang, M. Vijayakumar, Z. Nie, B. Chen, J. Zhang, G. Xia, J. Hu, G. Graff, J. Liu, Z. Yang, A stable vanadium redox-flow battery with high energy density for large-scale energy storage, Adv. Energy Mater. 1 (2011) 394–400.

[36] X. Wei, W. Xu, M. Vijayakumar, L. Cosimbescu, T. Liu, V. Sprenkle, W. Wang, TEMPO-based catholyte for high-energy density nonaqueous redox flow batteries, Adv. Mater. 26 (2014) 7649–7653.

[37] X. Wei, L. Cosimbescu, W. Xu, J.Z. Hu, M. Vijayakumar, J. Feng, M.Y. Hu, X. Deng, J.

Xiao, J. Liu, V. Sprenkle, W. Wang, Towards high-performance nonaqueous redox flow electrolyte via ionic modification of active species, Adv. Energy Mater. 5 (2014) 1400678.

[38] R.I. Haines, A. McAuley, Synthesis and reactions of Ni(III) complexes, Coord. Chem. Rev. 39 (1981) 77–119.

[39] J. Kucharyson, Structure-function relationships of metal coordination complexes for non-aqueous redox flow batteries, University of Michigan, 2017.

[40] J. England, C.C. Scarborough, T. Weyhermüller, S. Sproules, K. Wieghardt, Electronic structures of the electron transfer series [M(bpy)3]n , [M(tpy)2]n, and [Fe(t-bpy)3] n (M = Fe, Ru; n = 3+, 2+, 1+, 0, 1-): a mössbauer spectroscopic and DFT study, Eur. J. Inorg. Chem. 29 (2012) 4605–4621.

[41] M.T. Rodgers, P.B. Armentrout, Absolute alkali metal ion binding af nities of several azoles determined by threshold collision-induced dissociation, Int. J. Mass Spectrom. 187 (1999) 359–380.

[42] R. Amunugama, M.T. Rodgers, Periodic trends in the binding of metal ions to pyridine studied by threshold collision-induced dissociation and density functional theory, J. Phys. Chem. A. 105 (2001) 9883–9892.

[43] A. Nimmermark, L. Öhrström, J. Reedijk, Metal-ligand bond lengths and strengths: Are they correlated? A detailed CSD analysis, Cryst. Mater. 288 (2013) 311–317.

[44] R.D. Hancock, Chelate ring size and metal ion selection. The basis of selectivity for metal ions in open-chain ligands and macrocycles, J. Chem. Educ. 69 (1992) 615–621.

Chapter 4

Effect of Electrode Material on ATEMPO Stability and Flow Cell Performance

4.1 Background and Approach

The development of electrochemically stable active materials is a critical issue in the advancement of non-aqueous redox flow batteries (NAqRFBs). [1] A number of factors are expected to impact stability, including active species structure, [2,3] electrolyte composition, [4] and flow cell components (membrane/separator, electrode, cell hardware). [5] Work to date has focused extensively on the improvement of active species and electrolytes as both have a major impact on stability. While component interactions have received less attention, they have been shown to cause premature capacity fade. The most prevalent examples are the deleterious interactions between membranes and non-aqueous active species/electrolytes. [5–7] It is therefore necessary to develop active species that exhibit inherent electrochemically stability and to ensure all cell components are optimized to maintain high stability in a full flow configuration.

The optimization of flow cell components will improve stability while also providing a route for enhancing cell performance. [8] In this study, power density (limiting current density), and areal specific resistance (ASR) are used to quantify flow cell performance. Power density is a metric commonly used to compare fuel cells and batteries. [9,10] Increasing power density decreases the necessary cell/stack size providing a route for cost savings. [8,11] ASR

encompasses cell losses due to ohmic, mass transfer, and charge transfer resistances, which are directly related to all aspects of flow cell performance. Decreasing ASR enables operation at the high current and power densities relevant for large scale applications. [12]

Of the mentioned cell components, the electrode is expected to have the greatest influence on NAqRFB performance. [13] The most common RFB electrodes are carbon based felts or papers. Carbon is an ideal electrode material as it is inert, has a wide operating potential range and is highly conductive. [14] In the field of aqueous RFBs, electrode material has been shown to have a significant impact on reaction kinetics, and therefore cell performance. [15] Significant efforts have been made to improve performance of aqueous RFBs through electrode modification, including electrochemical, chemical and thermal treatments. [16] These treatments have also been shown to affect reaction kinetics, impacting maximum power density and ASR. While similar trends are expected in non-aqueous systems, limited research has been conducted in this area. [17] As promising active species are identified for NAqRFBs, the optimization of cell components to enhance flow cell performance and stability is becoming increasingly relevant.

In this chapter I will discuss the effect of electrode material on the cycling stability and flow cell performance of a NAqRFB employing 4-acetamido-2,2,6,6-tetramethylpiperidine-1-oxyl (ATEMPO) as a model active species. Experiments are performed on a variety of carbon based electrode materials: three papers (GFD29AA, AvCarb190, Toray060), one cloth (NuVant) and one felt (GFD3). First, single electrolyte cells are used to run EIS and polarization curves at varying flow rates. From these experiments, cell ASR and limiting current densities are calculated. Next, symmetric flow cells are assembled to measure the electrochemical stability of A-TEMPO on each material, using capacity retention after 100 cycles as a performance metric.

Finally, a techno-economic model is used to quantify the potential cost savings associated with minimizing flow cell ASR. Overall, this work offers an assessment of the impact of electrode material on flow cell stability and performance in non-aqueous media and demonstrates the importance of component optimization for NAqRFB development.

4.2 Experimental

4.2.1 Flow Cells

Flow cells are devices used to assess the cell level performance of a given active species. They offer a convenient method for testing materials at high concentrations, which is increasingly relevant for NAqRFBs with the continued identification of highly soluble materials. [2,18–20] In addition, these studies reveal any deleterious interactions between the active species, separator/membrane and cell components. One drawback of flow cell experiments is the quantity of active material and electrolyte that are necessary, especially for high concentration studies. Further, there are no reference electrodes present in a flow cell, so results can be difficult to interpret without supplementary stability studies. [21]

Flow cell experiments provide information on active species electrochemical stability as well as overall cell performance. Charge-discharge studies can be used to quantify cycle life and efficiencies (coulombic, voltaic and energy). In this work, cycle life is defined as the number of cycles to reach 80% of the initial capacity. Coulombic efficiency (CE) is the ratio of discharge to charge capacity, commonly reported as a percentage. This value encompasses losses due to active species degradation, crossover, and component interactions. Voltaic efficiency (VE) is the ratio of the average discharge to charge potential. VE is affected by cell overpotentials, which are a direct result of resistive losses. Energy efficiency (EE) is the product of CE and VE. [7]

Flow cells can also be used to characterize system performance. Electrochemical impedance spectroscopy (EIS) provides overall cell ASR as well as individual resistive components for ohmic, charge transfer and mass transfer losses. Additionally, polarization curves can be used to determine achievable power densities and limiting current densities at different conditions.

The lab scale flow cell used in this work is shown in Figure 4.1a. Backing plates were machined from polypropylene, and flow fields were machined from 3.18 mm thick impregnated graphite (G347B graphite, MWI, Inc.). Interdigitated flow fields (Figure 4.1b) were used for all studies. The alternating inlets and outlets of this design force the electrolyte to flow through the electrode and it has been suggested that this layout is well suited for scale-up. [22] Teflon gaskets (McMaster-Carr) were used to seal the cell. The gasket thickness was tailored for each electrode material to achieve a constant electrode compression of 20%. All cell component materials were selected for their compatibility with MeCN.

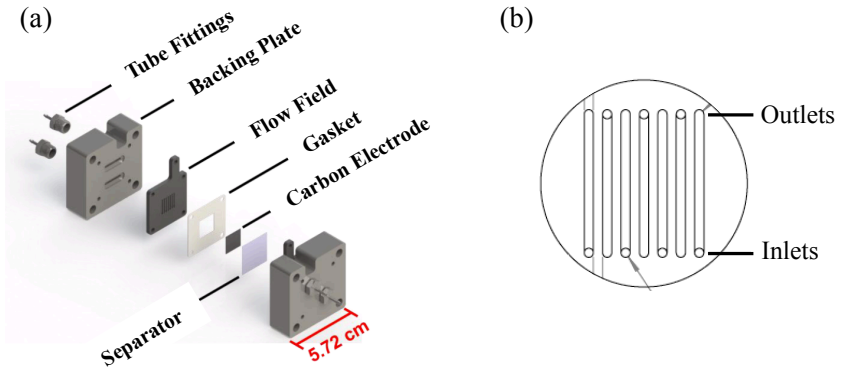

Figure 4.1 Schematics of **(a)** the flow cell and **(b)** an interdigitated flow field.

4.2.2 Flow Cell Configurations

There are a number of different flow cell configurations that can be used to characterize system performance. Figure 4.2 summarizes three possible flow cell setups.

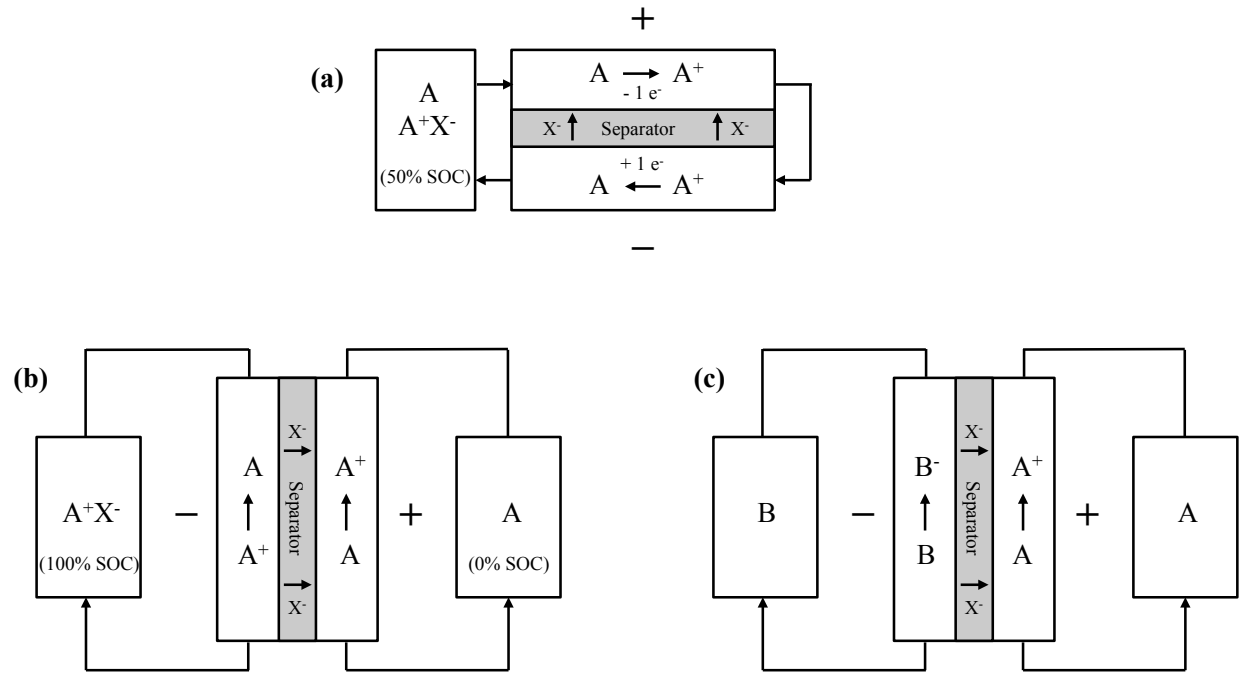

Figure 4.2 Flow cell schematics for **(a)** a single electrolyte flow cell during charge, **(b)** a symmetric flow cell during charge and **(c)** a full flow cell during charge. X represents a monovalent charge carrying anion while A and B are the catholyte and anolyte active materials, respectively.

The first is a single electrolyte flow cell (Figure 4.2a). [22,23] In this configuration there is only a single reservoir that contains one active species at 50% state of charge (SOC). During operation, the mixture is charged at the cathode as it enters the cell and then immediately fed to the anode where it is subsequently discharged. In this setup, the reservoir always remains at 50% SOC. This configuration is excellent for running EIS and polarization curve studies as it requires minimal active material and sustains a constant SOC. Further, it enables characterization of a

single redox event in a flow cell environment. However, these studies do not provide any information on cycling stability, assessable capacity, crossover rates or cell efficiencies.

To assess any of these parameters it is necessary to run full cell experiments. The first full cell option is a symmetric flow cell (Figure 4.2b). [23,24] In this system there are two reservoirs, each containing the same active species. Before cycling, one reservoir contains a solution at 0% SOC and the other a solution at 100% SOC. Upon cycling, the reservoirs cyclically alternate between 0 and 100% SOC. This results in a 0 V cell, which means the VE and EE are irrelevant. This configuration also requires generating a solution at both 0% and 100% SOC, which can be difficult. A major advantage of this configuration is the ability to assess the cycling performance of a single active species in a flow cell setup. Additionally, capacity retention, assessable capacity and CE can all be measured.

The final configuration is a traditional full flow cell (Figure 4.2c). [7,21] In a full flow cell different redox events are utilized as the catholyte and the anolyte. This requires either a species with multiple redox couples or the combination of a suitable catholyte and anolyte material. As these redox events will have different standard potentials, VE and EE are now meaningful values. All other parameters can also be measured using this cell, including capacities, efficiencies and crossover rates. As a whole, this technique provides a method for testing materials in an environment similar to that of a practical application. This configuration does require a significant amount of active species and the results can be difficult to interpret. Therefore, it is preferable to have a comprehensive understanding of the electrochemical behavior of each species before performing a full flow cell study.

4.2.3 Experimental Details

For these studies, electrodes were cut from GDL 29AA (190 μm, SGL Group), AvCarb MGL190 (190 μm, AvCarb Material Solutions, Fuel Cell Store), TGP-H-060 (190 μm, Toray, Fuel Cell Store), Nuvant ELAT hydrophilic plain cloth (406 μm, NuVant Systems) or GFD3 (3 mm, SGL Group). To maintain a similar electrode thickness, cells were assembled using two layers of carbon paper or one layer of carbon cloth or felt. A single layer of Daramic 175 served as the battery separator. Teflon gaskets were used to achieve 20% electrode compression and seal the separator into the cell. The assembled flow cells were tightened to a torque of 10 in-lbs. All flow cells were initially assembled outside the glove box, and were then dried under vacuum at room temperature for at least 1 h before beginning flow cell experiments. ATEMPO (97%, Sigma Aldrich), $ATEMPO^+$ (97%, Sigma Aldrich) and tetraethylammonium tetrafluoroborate ($TEABF_4$, 99.5%, BASF) were used as received. MeCN was stored over molecular sieves for >24 h prior to use to remove any residual water. Each reservoir was filled with 10 mL of electrolyte. Electrolyte was pumped through the flow cell using a peristaltic pump (Masterflex L/S series) with Tygon tubing (Saint-Gobain, 1.6 mm inner diameter). All flow cell studies were performed using a Biologic-VMP3 potentiostat.

Polarization curves and EIS measurements were performed using a single electrolyte flow cell configuration. The electrolyte was composed of 25 mM ATEMPO / 25 mM $ATEMPO^+$ / 0.5 M $TEABF_4$ / MeCN and pumped through the cell at rates of 2.5, 5 and 10 mL/min. Polarization curves were performed at constant potential over a range of 0.05 V to 0.6 V with a step size of 0.05 V. Each potential was held for 45 s to allow the system sufficient time to

achieve a steady state current response. Flow cell impedance measurements were recorded about OCV over a frequency range of 10 mHz to 1 MHz with a potential amplitude of 10 mV.

Cycling experiments were performed in a symmetric flow cell configuration. The catholyte and anolyte were composed of 50 mM ATEMPO / 0.5 M $TEABF_4$ / MeCN and 50 mM $ATEMPO^+$ / 0.5 M $TEABF_4$ / MeCN, respectively. Electrolyte was pumped through the flow cell at a rate of 10 mL/min. Cycling was performed at a constant current of 15 mA/cm^2 with potential cutoffs of 0.3 V and -0.3 V for charge and discharge, respectively. A 100% SOC coulombic cutoff was also employed to prevent overcharging.

4.3 Results and Discussion

4.3.1 Active Species Selection

Several criteria were established to aid in the selection of a model active species for these studies. First, the material needs to exhibit reversible electrochemistry as well as relatively high solubility and stability in MeCN. Most importantly, the material needs to be commercially available or easy to synthesize in both the neutral and charged states. Based on these considerations, ATEMPO was selected as a model active species (Figure 4.3).

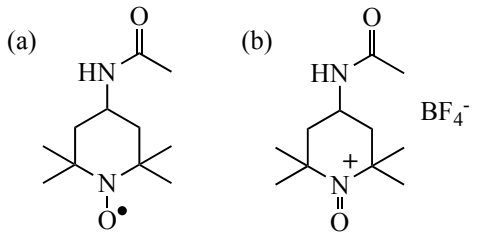

Figure 4.3 Structures of (a) ATEMPO and (b) $ATEMPO^+$.

ATEMPO is commercially available at both 0% SOC (ATEMPO) and 100% SOC ($ATEMPO^+$). As such it is convenient to utilize both the single electrolyte and symmetric cell configurations shown in Figure 4.2. Additionally, TEMPO and its derivatives have been investigated as active species for NAqRFBs and have been shown to exhibit high reversibility, solubility and electrochemical stability. [19,25] ATEMPO has also been well characterized in propylene carbonate (PC) and proposed as a model active species for quantifying the performance characteristics of NAqRFBs. [23]

4.3.2 Electrochemical Impedance Spectroscopy

EIS is a technique commonly used to quantify flow cell resistance. [8,23,26,27] Nyquist plots can be used to estimate the individual contributions of ohmic, mass transfer and charge transfer resistances. Figure 4.4a shows a representative example of the impendence spectra measured in this study.

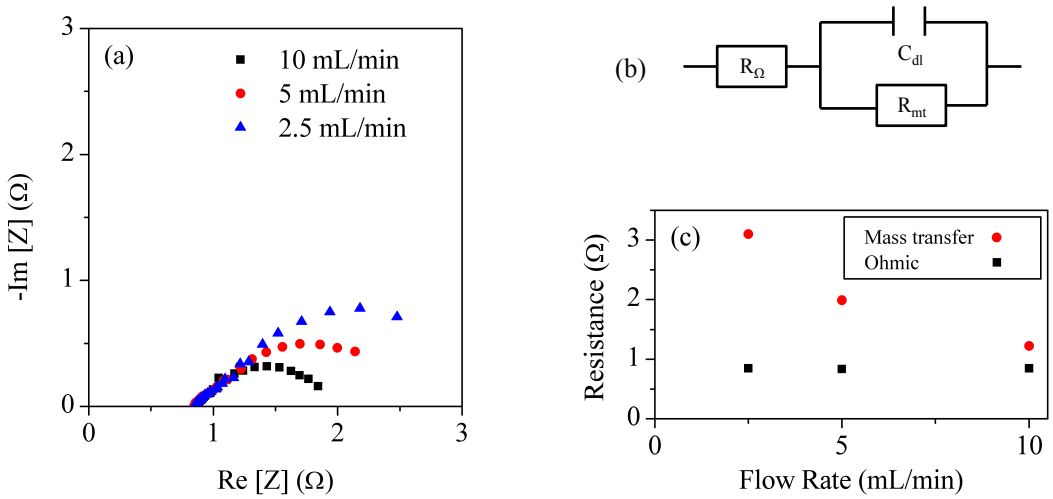

Figure 4.4 EIS data for Toray paper. **(a)** EIS spectra at different flow rates. **(b)** Equivalent circuit used to model the data. **(c)** Ohmic and mass transfer contributions to the cell resistance.

EIS spectra are analyzed by fitting the data to an equivalent circuit model (Figure 4.4b). In this case, the high frequency intercept with the real (x) axis provides the ohmic resistance of the flow cell (R_Ω). [8,26] As show in Figure 4.4c, this value remains constant with flow rate. In an electrochemical cell, charge transfer and mass transfer resistances are both represented by a single semi-circle, with the diameter of the semi-circle corresponding to the magnitude of the resistance. The kinetics of non-aqueous chemistries are generally fast, and therefore no charge transfer resistance is expected to be observed. To confirm that the observed semi-circle is a result of a diffusive process, experiments were performed at different flow rates. As expected, the resistance decreases with increasing flow rate (Figure 4.4c), confirming that the observed semi-circle represents the mass transfer resistance. Modeling the diameter of the semi-circle provides the mass transfer resistance (R_{mt}). Finally, the low frequency intercept with the real axis for a system with a bounded semi-circle represents the total direct current cell resistance and is a good measure of cell ASR. [27]

EIS experiments for each electrode material were performed at flow rates of 10, 5, and 2.5 mL/min. Results are shown in Figure 4.5. Orange bars represent the ohmic resistance, grey the charge transfer resistance and blue the mass transfer resistance. A summation of these values (the total height of the bar) represents the total cell resistance.

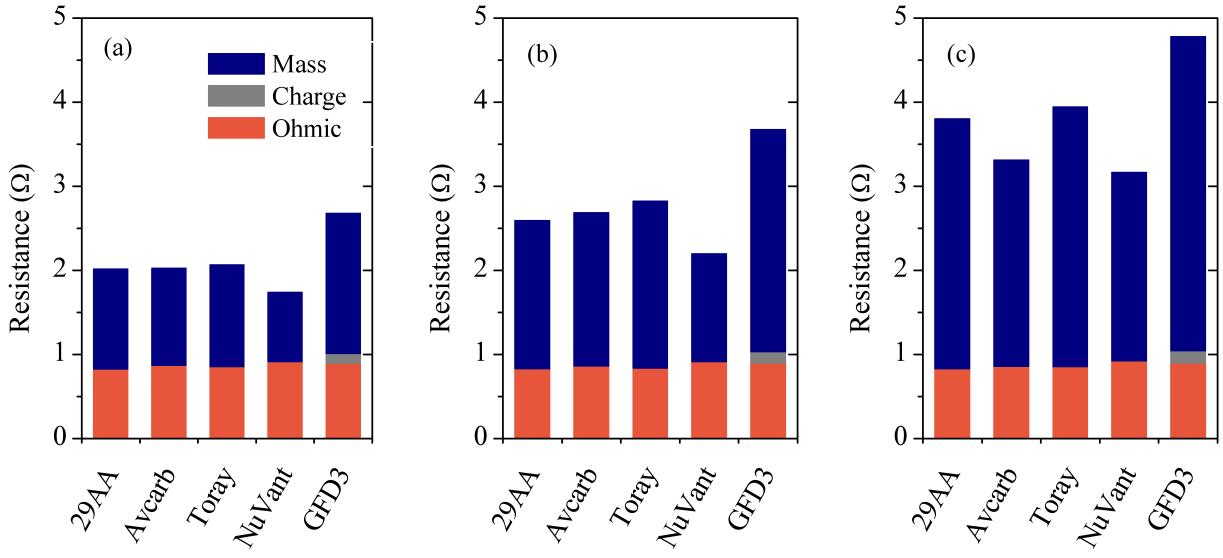

Figure 4.5 Cell resistance as measured by EIS, separated into ohmic, mass transfer and charge transfer contributions at flow rates of **(a)** 10 mL/min, **(b)** 5 mL/min and **(c)** 2.5 mL/min.

A comparison of the ohmic resistance of each cell across all flow rates reveals a similar contribution in all cases. Each cell employs the same electrolyte and hardware, as well as identical electrode compression, with variations only in the electrode material. These results indicate that contact resistances, as well as the bulk resistance of the cell components dominate the ohmic losses. This is expected since all of the electrode materials are highly conductive. GFD3 is the only material that exhibits any charge transfer resistance. As expected, this value is constant across all flow rates. This resistance is a result of the relative thickness of the material, which leads to an increased charge transfer distance within the flow cell. [28]

A comparison of the mass transfer resistances reveals that the electrode material has a clear impact on this value. It should be noted that it was difficult to obtain clean EIS spectra at 2.5 mL/min, resulting in greater variation in the calculated mass transfer resistances. The observed trends hold at this flow rate, but comparisons will be discussed in terms of the data for

flow rates of 5 and 10 mL/min. At these flow rates each carbon paper (29AA, AvCarb, Toray) performs in a similar manner. This was anticipated as these materials all have similar porosity and thickness. Greater variations are observed between the different types of carbon materials. In agreement with prior literature, the carbon felt (GFD3) exhibits a significantly higher mass transfer resistance. This has been attributed to the difference in porosity between carbon paper (~80%) and carbon felt (~98%). [28] The relative thickness of the carbon felt in this study also contributes to the high resistance. NuVant exhibits the lowest diffusive resistance of all the tested materials. This is attributed to the use of only a single layer of cloth during cell assembly.

Overall, GFD3 shows the highest ASR primarily as a result of the relative thickness of the material. [26] These results in are agreement with AqRFB literature where carbon paper electrodes have been shown to dramatically improve power density over traditional felt electrodes. [29] The carbon cloth provides a further increase in overall performance offering the lowest ASR at all studied conditions.

4.3.3 Polarization Curves

Polarization curves, coupled with EIS experiments, are an excellent technique for identifying the main limitations to flow cell performance. [30] Polarization curves consist of three distinct regions, each dominated by a specific type of polarization loss. The first region exists at low current densities where the behavior is dominated by kinetic activation polarization. These losses result from slow charge transfer reactions at the electrode/electrolyte interface. In non-aqueous systems these losses are typically negligible due to facile kinetics. At moderate current densities, ohmic losses dominate the polarization curve resulting in linear behavior. The slope of this linear region corresponds to the ASR measured by EIS. The third region

corresponds to concentration polarization losses. This behavior occurs at high current densities when mass transport of the reactants limits the current density of the cell. As a result, the current density plateaus and a limiting current can be measured for a specific set of conditions. [30] In this study, polarization curves were used to measure the limiting current of each cell at flow rates between 2.5 and 10 mL/min. A representative example is shown in Figure 4.6.

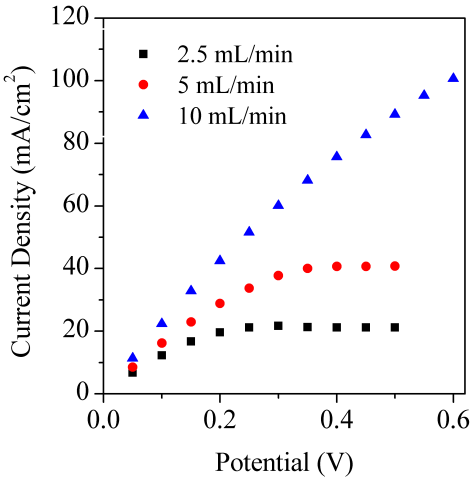

Figure 4.6 Polarization curves for Toray paper at various flow rates.

Regions dominated by ohmic losses and concentration polarization losses are apparent at low flow rates (2.5 and 5 mL/min). As the flow rate increases, the onset of the concentration polarization region shifts to higher potentials and the limiting current increases. At a flow rate of 10 mL/min, a limiting current is no longer observed within the measured potential window. This indicates that the flow rate is sufficient enough to overcome any mass transport limitations. All flow cell cycling studies were performed at 10 mL/min.

To compare the performance of the different electrode materials, limiting currents are reported at 2.5 mL/min and 5 mL/min. In all cases a limiting current was not reached at 10 mL/min. As shown in Figure 4.7 the limiting current is similar for all materials studied. At 2.5

mL/min, the lowest limiting currents are observed for NuVant and 29AA. This behavior is due to the lower surface area of these two materials.

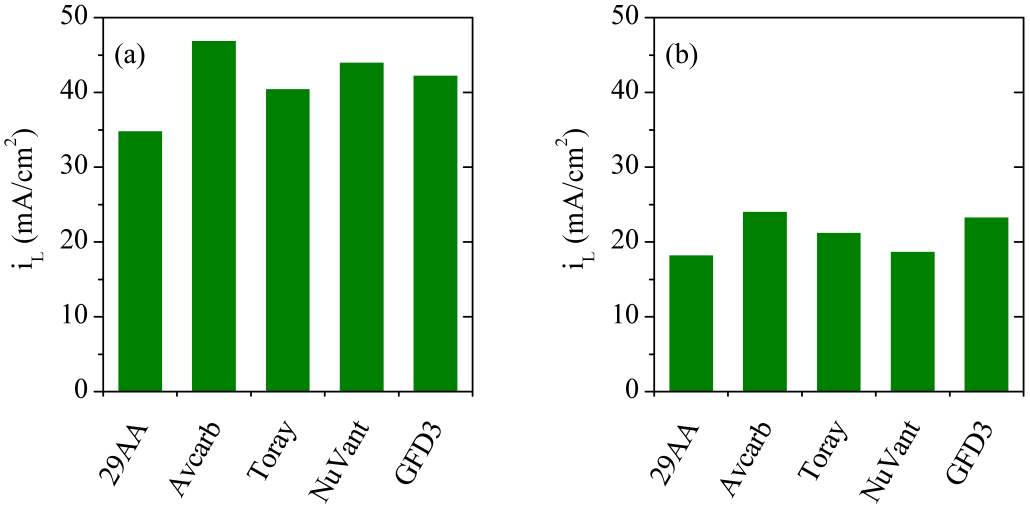

Figure 4.7 Limiting currents for all electrode materials calculated from polarization curves measured at **(a)** 5 mL/min and **(b)** 2.5 mL/min.

4.3.4 Flow Cell Performance

An ideal electrode material will exhibit a low ASR and a high limiting current. A compilation of the relevant values for the studied electrode materials is shown in Figure 4.8.

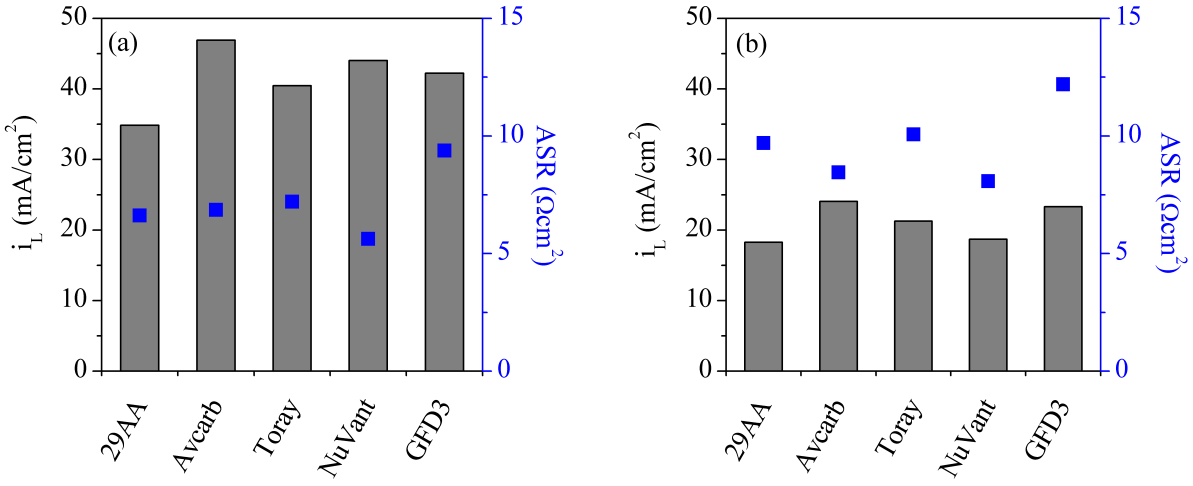

Figure 4.8 Limiting current (grey) and ASR (blue) for each electrode material at a flow rate of **(a)** 5 mL/min and **(b)** 2.5 mL/min.

At both 2.5 mL/min and 5 mL/min the NuVant cloth and AvCarb paper offer the best performance, exhibiting high limiting currents and low ASRs. The carbon felt (GFD3) exhibits the worst performance, mainly as a result of the high ASR of this material, and these findings are in agreement with current aqueous literature. [29] In general, for small-scale flow cell testing which utilizes relatively low current densities, any of these materials will offer comparable performance. However, when moving to large-scale systems the observed variations will start to have noticeable effects and then these findings can be used to guide the selection of cell components.

4.3.5 Flow Cell Stability

The final step in comparing each electrode material involved symmetric flow cell studies to assess the impact of electrode material on ATEMPO cycling stability. Figure 4.9 displays discharge capacity as a function of cycle for each electrode material.

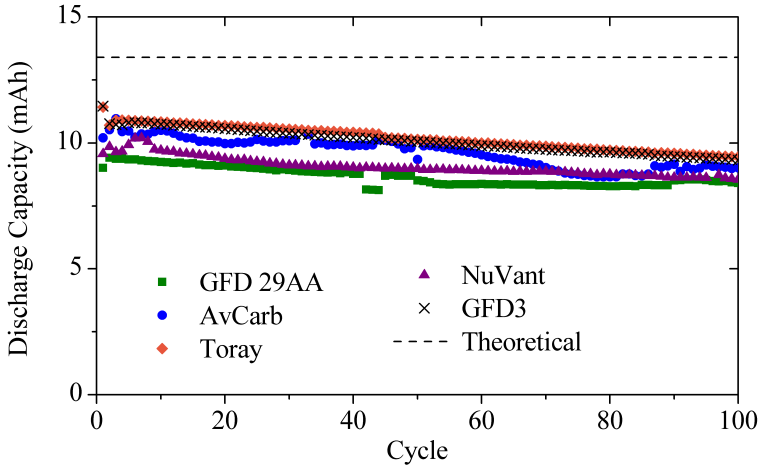

Figure 4.9 Discharge capacity of a symmetric A-TEMPO flow cell over 100 cycles for different electrode materials. Flow cell were cycled at a current density of 15 mA/cm^2 and a flow rate of 10 mL/min. The dashed line represents the theoretical capacity.

All cells have a similar accessed capacity, with the minor differences attributed to variations in cell assembly. The deviation from the theoretical capacity is a result of the relatively high (15 mA/cm^2) current density employed for these studies. In each case, the cycling curve displays a comparable slope, indicating a consistent degradation mechanism. To quantify the stability of ATEMPO on each electrode material, capacity retention after 100 cycles was calculated (Table 4.1). In all cases, the capacity retention is within experimental error.

Table 4.1 Capacity retention of ATEMPO after 100 cycles on different electrode materials.

Electrode Material	% Initial Capacity (100 cycles)
GFD 29AA	82%
Toray	83%
AvCarb	82%
NuVant	81%
GFD 3	81%

Overall, these results suggest that the electrochemical stability of ATEMPO is unaffected by changes in the electrode material. This is a desirable trait for an active species as the electrode material can be optimized independently without negatively affecting electrochemical stability. This behavior is expected to be highly active species dependent. For example, vanadium acetylacetonate has been shown to be sensitive to the presence of oxygen and water. [31] It is possible the electrode materials contain different surface functional group that would impact the cycling stability of a more sensitive system.

4.3.6 Techno-economic Analysis

Although the observed changes in ASR were small, it is expected that these variations will still have an impact on total system price. To confirm, a simple techno-economic analysis was used to relate the ASR to the total system price at different cell potentials (Figure 4.10). A full discussion of the equations and variables used for the techno-economic analysis can be found in Section 6.3.7.1.

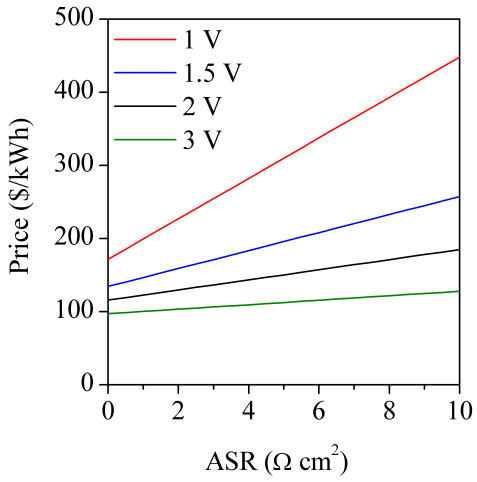

Figure 4.10 Techno-economic analysis showing the sensitivity of system price ($/kWh) to area specific resistance for different cell potentials.

This analysis was adopted from [11] and calculations were performed using the parameters reported therein. An optimistic solubility of 1 kg/kg was assumed, with a more realistic solubility just shifting the y-intercept to higher values with no impact on the slope. The slope of the line scales with $1/U^2$, where U is the cell potential, with lower cell potentials showing significantly higher variations in price. At an optimistic cell potential of 3 V the price savings per ASR unit are ~$3/kWh, increasing to ~$7/kWh for a cell potential of 2 V. These results demonstrate the importance of decreasing ASR and verify that the small variations observed for different electrode materials have a measurable impact on system price. It should be noted that differences in the cost of the electrode materials were not considered.

4.4 Conclusions

The goal of this work was to study the impact of electrode material on the electrochemical stability and flow cell performance of ATEMPO. Polarization curves and EIS measurements provide a clear understanding of NAqRFB performance limitations in each case. Kinetics losses are negligible for this system, with ohmic and mass transport losses dominating in different current density regimes. Comparative studies of the ASR and limiting current for different electrode materials revealed only minor differences in performance. In general, carbon papers perform better than carbon felt and overall NuVant and AvCarb offer the best performance. It should be noted that the slight variations observed in performance will have a negligible impact on lab scale flow cell studies, but they will become relevant for large scale studies. A simple techno-economic analysis was used to demonstrate this point by presenting the price savings that can be achieved with small changes in ASR. In terms of stability, A-TEMPO is

shown to be insensitive to changes in the electrode material. While this is an excellent trait for an active species to possess, further studies on a more sensitive active species would be required to fully understand the impact of electrode material on electrochemical stability. Since this behavior will be active species dependent, it will be necessary to first identify promising active materials that require performance improvement studies. Overall, this work offers a comparative study of the performance of different electrode materials that will be valuable for the future development and optimization of large scale NAqRFBs.

4.5 Acknowledgements

I would like to thank Dr. Jarrod Milshtein from Dr. Fikile Brushett's group at the Massachusetts Institute of Technology for providing the flow cell design.

4.6 References

[1] G.L. Soloveichik, Flow batteries: current status and trends, Chem. Rev. 115 (2014) 11533–11558.

[2] C.S. Sevov, S.L. Fisher, L.T. Thompson, M.S. Sanford, Mechanism-based development of a low-potential, soluble, and cyclable multielectron anolyte for nonaqueous redox flow batteries, J. Am. Chem. Soc. 138 (2016) 15378–15384.

[3] J. Huang, L. Su, J. a. Kowalski, J.L. Barton, M. Ferrandon, A.K. Burrell, F.R. Brushett, L. Zhang, A subtractive approach to molecular engineering of dimethoxybenzene-based redox materials for non-aqueous flow batteries, J. Mater. Chem. A. 3 (2015) 14971–14976.

[4] X. Wei, W. Xu, J. Huang, L. Zhang, E. Walter, C. Lawrence, M. Vijayakumar, W. a. Henderson, T. Liu, L. Cosimbescu, B. Li, V. Sprenkle, W. Wang, Radical compatibility with nonaqueous electrolytes and its impact on an all-organic redox flow battery, Angew. Chemie Int. Ed. 54 (2015) 8684–8687.

[5] S.H. Shin, S.H. Yun, S.H. Moon, A review of current developments in non-aqueous redox flow batteries: characterization of their membranes for design perspective, RSC Adv. 3 (2013) 9095-9116.

[6] N.S. Hudak, L.J. Small, H.D. Pratt, T.M. Anderson, Through-plane conductivities of membranes for nonaqueous redox flow batteries, J. Electrochem. Soc. 162 (2015) A2188–

A2194.

[7] I. Escalante-Garcia, J. Wainright, L. Thompson, R. Savinell, Performance of a non-aqueous vanadium acetylacetonate prototype redox flow battery: examination of separators and capacity decay, J. Electrochem. Soc. 162 (2015) A363–A372.

[8] C.N. Sun, F.M. Delnick, D.S. Aaron, A.B. Papandrew, M.M. Mench, T.A. Zawodzinski, Probing electrode losses in all-vanadium redox flow batteries with impedance spectroscopy, ECS Electrochem. Lett. 2 (2013) A43–A45.

[9] G.L. Soloveichik, Battery technologies for large-scale stationary energy storage, Annu. Rev. Chem. Biomol. Eng. 2 (2011) 503–527.

[10] A. Kirubakaran, S. Jain, R.K. Nema, A review on fuel cell technologies and power electronic interface, Renew. Sustain. Energy Rev. 13 (2009) 2430–2440.

[11] R. Darling, K.G. Gallagher, J.A. Kowalski, S. Ha, F.R. Brushett, Pathways to low-cost electrochemical energy storage: a comparison of aqueous and nonaqueous flow batteries, Energy Environ. Sci. 7 (2014) 3459–3477.

[12] K. Gong, Q. Fang, S. Gu, S.F.Y. Li, Y. Yan, Nonaqueous redox-flow batteries: organic solvents, supporting electrolytes, and redox pairs, Energy Environ. Sci. 8 (2015) 3515-3530.

[13] K.J. Kim, M.-S. Park, Y.-J. Kim, J.H. Kim, S.X. Dou, M. Skyllas-Kazacos, A technology review of electrodes and reaction mechanisms in vanadium redox flow batteries, J. Mater. Chem. A. 3 (2015) 16913–16933.

[14] W. Wang, Q. Luo, B. Li, X. Wei, L. Li, Z. Yang, Recent progress in redox flow battery research and development, Adv. Funct. Mater. 23 (2013) 970–986.

[15] M.H. Chakrabarti, N.P. Brandon, S.A. Hajimolana, F. Tariq, V. Yufit, M.A. Hashim, M.A. Hussain, C.T.J. Low, P. V. Aravind, Application of carbon materials in redox flow batteries, J. Power Sources. 253 (2014) 150–166.

[16] A. Bourke, M.A. Miller, R.P. Lynch, J.S. Wainright, R.F. Savinell, D.N. Buckley, Effect of cathodic and anodic treatments of carbon on the electrode kinetics of V^{IV} /V^{V} oxidation-reduction, J. Electrochem. Soc. 162 (2015) A1547–A1555.

[17] M.S. Park, N.J. Lee, S.W. Lee, K.J. Kim, D.J. Oh, Y.J. Kim, High-energy redox-flow batteries with hybrid metal foam electrodes, ACS Appl. Mater. Interfaces. 6 (2014) 10729–35.

[18] C.S. Sevov, R.E.M. Brooner, E. Chénard, R.S. Assary, J.S. Moore, J. Rodríguez-López, M.S. Sanford, Evolutionary design of low molecular weight organic anolyte materials for applications in nonaqueous redox flow batteries, J. Am. Chem. Soc. 137 (2015) 14465–14472.

[19] X. Wei, W. Xu, M. Vijayakumar, L. Cosimbescu, T. Liu, V. Sprenkle, W. Wang, TEMPO-based catholyte for high-energy density nonaqueous redox flow batteries, Adv. Mater. 26 (2014) 7649–7653.

[20] J. Huang, B. Pan, W. Duan, X. Wei, R.S. Assary, L. Su, F.R. Brushett, L. Cheng, C. Liao, M.S. Ferrandon, W. Wang, Z. Zhang, A.K. Burrell, L.A. Curtiss, I.A. Shkrob, J.S. Moore, L. Zhang, The lightest organic radical cation for charge storage in redox flow batteries, Sci. Rep. 6 (2016) 32102.

[21] S.M. Laramie, J.D. Milshtein, T.M. Breault, F.R. Brushett, L.T. Thompson, Performance and cost characteristics of multi-electron transfer, common ion exchange non-aqueous redox flow batteries, J. Power Sources. 327 (2016) 681–692.

[22] R.M. Darling, M.L. Perry, The Influence of electrode and channel configurations on flow battery performance, J. Electrochem. Soc. 161 (2014) A1381–A1387.

[23] J.D. Milshtein, J.L. Barton, R.M. Darling, F.R. Brushett, 4-acetamido-2,2,6,6-tetramethylpiperidine-1-oxyl as a model organic redox active compound for nonaqueous flow batteries, 327 (2016) 151–159.

[24] J.D. Milshtein, A.P. Kaur, M.D. Casselman, J.A. Kowalski, S. Modekrutti, P. Zhang, N.H. Attanayake, C.F. Elliott, S.R. Parkin, C. Risko, F.R. Brushett, S.A. Odom, High current density, long duration cycling of soluble organic active species for non-aqueous redox flow batteries, Energy Environ. Sci. 9 (2016) 3531–3543.

[25] S.K. Park, J. Shim, J. Yang, K.H. Shin, C.S. Jin, B.S. Lee, Y.S. Lee, J.D. Jeon, Electrochemical properties of a non-aqueous redox battery with all-organic redox couples, Electrochem. Commun. 59 (2015) 68–71.

[26] C.N. Sun, F.M. Delnick, D.S. Aaron, A.B. Papandrew, M.M. Mench, T.A. Zawodzinski, Resolving losses at the negative electrode in all-vanadium redox flow batteries using slectrochemical impedance spectroscopy, J. Electrochem. Soc. 161 (2014) A981–A988.

[27] J. Milshtein, S. Fisher, T. Breault, L. Thompson, F. Brushett, Feasibility of a supporting salt free non-aqueous redox flow battery utilizing ionic active materials, ChemSusChem. 10 (2017) 2080–2088.

[28] Q.H. Liu, G.M. Grim, A.B. Papandrew, A. Turhan, T.A. Zawodzinski, M.M. Mench, High performance vanadium redox flow batteries with optimized electrode configuration and membrane selection, J. Electrochem. Soc. 159 (2012) A1246–A1252.

[29] D.S. Aaron, Q. Liu, Z. Tang, G.M. Grim, A.B. Papandrew, A. Turhan, T.A. Zawodzinski, M.M. Mench, Dramatic performance gains in vanadium redox flow batteries through modified cell architecture, J. Power Sources. 206 (2012) 450–453.

[30] D. Aaron, Z. Tang, A.B. Papandrew, T.A. Zawodzinski, Polarization curve analysis of all-vanadium redox flow batteries, J. Appl. Electrochem. 41 (2011) 1175–1182.

[31] A.A. Shinkle, A.E.S. Sleightholme, L.D. Griffith, L.T. Thompson, C.W. Monroe, Degradation mechanisms in the non-aqueous vanadium acetylacetonate redox flow battery, J. Power Sources. 206 (2012) 490–496.

Chapter 5

Active Species Compatibility Analysis for the Development of Asymmetric Non-aqueous Redox Flow Batteries

5.1 Background and Approach

Recent efforts to increase the energy density and decrease the cost of NAqRFBs have focused on improving active species solubility via molecular modifications and developing active species with low molecular weights. [1,2] With the continued identification of promising NAqRFB active materials, it is of increasing importance to consider how these materials could be utilized in a full flow system. Mainly, NAqRFB applications require an equivalent number of redox events on the positive and negative side of the cell. However, only a few active materials demonstrate balanced redox events, and in general those materials are relatively unstable. [3–6] A vast majority of the materials that have been identified as promising active species exhibit multiple redox events at only positive or negative potentials, [7–10] or only have a single redox couple. [1,11–16] Demonstrative examples for each case are shown in Figure 5.1. It will therefore be necessary to develop methodologies to utilize these types of materials in ways that are relevant for NAqRFB applications.

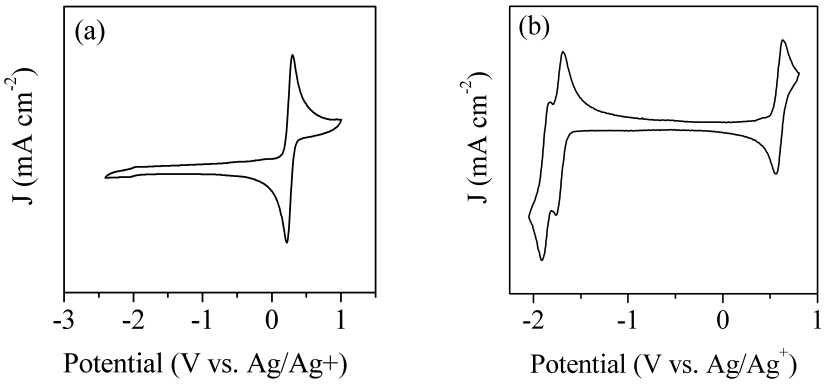

Figure 5.1 CVs in MeCN of (a) Fc-1N112-BF_4 that only exhibits a single redox event and (b) $Ni(BPI)_2$ with multiple, unbalanced redox couples.

To study the cell level performance of materials with single redox couples a few groups have developed hybrid flow systems that utilize a Li metal anode. [11,17] While useful for lab scale studies, employing a metal anode nullifies a major advantage of RFBs, which is the ability to decouple power and energy. Furthermore, this type of system can only be used to study catholyte molecules. A more attractive approach is to pair a promising anolyte and catholyte molecule on either side of a RFB. In this configuration, each molecule can be tuned independently to optimize performance. These types of systems have been used to study bipyridine MCCs employing different concentrations of active species as the anolyte and catholyte. [18,19] However, even with state-of-the-art non-aqueous membrane/separator technology, crossover is inevitable and active species mixing will occur. [20,21] To mitigate capacity loss due to crossover, fully mixed electrolyte systems are increasing in popularity. [9,13] Based on current trends in molecular development, mixed systems will become increasingly relevant for NAqRFB design. In both cases it is critical to understand any interactions that will occur between the catholyte and anolyte molecules at all charge states accessed during cycling. The goal of this work is to establish a method to efficiently identify

compatible chemistries to facilitate the extension of active species studies to full flow cell development.

In this chapter, I will discuss the design and demonstration of a series of experiments to examine the compatibility of asymmetric NAq chemistries. Iron (II) tris(2,2'-bypridine) tetrafluoroborate ($Fe(bpy)_3(BF_4)_2$) and ferrocenylmethyl dimethyl ethyl ammonium tetrafluoroborate (Fc1N112-BF_4) serve as model active species, and are examined via a progression of electrochemical techniques. This includes cyclic voltammetry (CV), bulk electrolysis, small volume H-type cells with reference electrodes, and flow cells. Flow cell cycling experiments characterize both the one electron ($1e^-$) and, for the first time, two electron ($2e^-$) variations of the $Fe(bpy)_3(BF_4)_2$/Fc1N112-BF_4 system, revealing the complexity of multi-electron transfer cells. Taken as a whole, this work develops an extensive compatibility analysis for asymmetric NAqRFB chemistries that minimizes the use of active material and also offers a route to easily interpreting complex flow cell cycling behavior. The systematic approach and suite of electrochemical techniques utilized here can be easily extended to other promising active species, including organics, metal coordination complexes (MCCs), and mixed MCC/organic systems. This versatility is demonstrated with the development of a stable, multi-electron $Co(BPI)_2$/ferrocene cell.

5.2 Experimental

5.2.1 Syntheses and Materials

All reagents and starting materials (iron(II) tetrafluoroborate hexahydrate (97%), (dimethylaminomethyl)ferrocene (96%), bromoethane (98%), sodium tetrafluoroborate (98%), ferrocene (98%), 4-acetamido TEMPO (97%)) for active species synthesis were purchased from

Sigma-Aldrich, except for 2,2'-bipyridine (98%, Alfa Aesar). Ferrocene was sublimated before use, while all other materials were used as received. Materials were synthesized according to the following procedures: $Fe(bpy)_3(BF_4)_2$ [9,22], Fc1N112-BF_4 [9,23], cobalt bipyridylimino isoindoline. [8] 2,5-di-*tert*-butyl-1,4-bis(2-methoxyethoxy)benzene (DBBB) was provided by the Zhang group at Argonne National Laboratory. [24] All electrochemical experiments were performed in acetonitrile (MeCN, 99.9%, Acros Organics), which was stored over molecular sieves to remove any residual water. Electrochemical grade tetrabutylammonium tetrafluoroborate ($TBABF_4$, 99%, Sigma Aldrich) was dried under vacuum at 80°C overnight before use. All solution preparation and electrochemical measurements were performed inside argon filled glove boxes (O_2 < 5 ppm, H_2O < 1 ppm). Daramic 175 microporous separator, with a thickness of 175 μm, porosity of 58%, and average pore size of 100 nm, was employed during battery cycling experiments.

5.2.2 Cyclic Voltammetry

Cyclic voltammograms were recorded at a scan rate of 100 mV s^{-1} using a glassy carbon working electrode (BASi), a coiled Pt wire counter, and a Ag/Ag^+ quasi-reference electrode. Solutions for the $Fe(bpy)_3(BF_4)_2$/Fc-1N112-BF_4 studies contained 0.5 M $TBABF_4$/MeCN with either 5 mM of the individual active species or an equi-molar mixture containing 5 mM of each. Experiments for the Co(**L5**)$_2$/Fc system were performed in 0.5 M $TBABF_4$/MeCN with 2 mM of the individual species or an equi-molar mixture containing 2 mM of each.

5.2.3 Bulk Electrolysis

Details on the cell setup can be found in Section 2.2.4. Studies for the $Fe(bpy)_3(BF_4)_2$/Fc1N112-BF_4 system were performed at a constant current of 1.32 mA (2C). Potential cutoffs and a 100% SOC coulombic cut-off were used during cycling. Solutions of 5 mM active species in 0.5 M $TBABF_4$/MeCN were used for the single species experiments and for the mixed species tests; 5 mM of both active species in 0.5 M $TBABF_4$/MeCN. Experiments for the Co(**L5**)$_2$/Fc system were performed with solutions containing 2 mM of the individual active species or an equi-molar mixture containing 2 mM of each species in 0.5 M $TBABF_4$/MeCN. These cells were cycled at a constant current of 0.27 mA (C/2) with potential cutoffs and a 100% SOC cutoff.

5.2.4 H-cell Cycling

H-cell cycling is a charge-discharge technique that can be used to study the full cell performance of a selected chemistry. A typical cell consists of two 5 mL chambers separated by a separator or membrane (Figure 5.2). Each chamber has a port for a working electrode and a reference electrode. H-cells are static with electrolyte mixing accomplished by continuously stirring each chamber. The major advantage of this technique is the ability to use a reference electrode to continually monitor the potential of the catholyte and the anolyte chambers independently. This provides a more complete understanding of the limitations of a full cell, as compared to a flow cell where only the overall cell potential is measured. Additionally, there is a separator or membrane present, which offers insight on any deleterious interactions between the electrolytes and the separator or membrane. There are a number of drawbacks to using H-cells. Mainly, the distance between the electrodes is significant and results in high overpotentials

during cycling. Furthermore, static cells have limited mass transport, so they are not useful for high concentration studies.

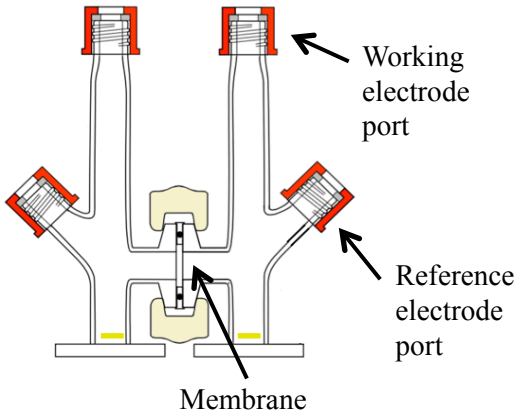

Figure 5.2 Schematic of the H-cells used in this work.

During cycling a constant current is applied between the two working electrodes and the overall cell potential is monitored. The potential between the cathode and the reference, and the anode and the reference, are also monitored simultaneously. Potential and state-of-charge cutoffs are used to control the experiment and cyclically switch between charge and discharge. Graphite rods are used as the working electrodes and are heat treated under argon before use to remove surface oxygen groups. Metrics of interest include capacity retention/cycle life, coulombic efficiency and voltaic efficiency. Cycle life is defined as the number of cycles before reaching 80% of the initial capacity. Coulombic efficiency is the ratio of the discharge capacity to charge capacity, typically reported as a percentage. Similarly, voltaic efficiency is the ratio of the average discharge potential to the average charge potential. As discussed previously, this value is expected to be low for H-cells due to high overpotentials. Potential curves for the cathode and anode can also be analyzed after cycling to determine which redox events each side of the cell is accessing.

For these experiments, two layers of Daramic 175 were stacked together as the separator. Graphite electrodes (3.6 cm^2, iso-molded, ground finish, Graphite Store) were heat treated at 500 °C for 5 h under argon before use. Cycling experiments were performed at a constant c-rate of C/2 to 100% SOC, with anolyte and catholyte potential cutoffs based on CV potentials. Cells used a solution of 0.5 M $TBABF_4$/MeCN with 50 mM of both $Fe(bpy)_3(BF_4)_2$/Fc1N112-BF_4 as the anolyte and catholyte or 2 mM of both Co(**L5**)$_2$/Fc.

5.2.5 Flow Cell Cycling

Custom cells with flow through electrodes were used for flow cell cycling experiments (see Section 4.2.1 for additional details). Electrodes were cut from 6 mm thick carbon felt (GFA6, SGL Group) and compressed by 12.4% in the assembled flow cell, providing a geometric active area of 4.63 cm^2. Two layers of Daramic 175 separator were stacked together to serve as the battery separator. Teflon gaskets sealed the separator into the cell. All flow cells were initially assembled outside the glove box, and were then dried under vacuum (-27 kPa_g) at room temperature for at least 1 h before beginning flow cell experiments. Electrolyte was pumped through the flow cell at 20 mL min^{-1} using a peristaltic pump (Masterflex L/S series) with Tygon tubing (Saint-Gobain, 1.6 mm inner diameter). Galvanostatic cycling experiments were performed using a Biologic-VMP3 potentiostat at a constant current density of 5 mA cm^{-2} (23.2 mA). Electrolytes were comprised of 0.1 M $Fe(bpy)_3(BF_4)_2$/0.1 M Fc1N112-BF_4/0.5 M $TBABF_4$/MeCN. 10 mL of electrolyte was added to each of the two flow cell reservoirs. During cycling experiments, cell potential cutoffs were 1.0 – 2.01 V and 1.0 – 2.45 V for the 1e- and $2e^-$ cells, respectively.

5.3 Results and Discussion

5.3.1 Compatibility Analysis

The methodology developed to assess the compatibility of asymmetric chemistries is composed of a series of electrochemical techniques. First, cyclic voltammetry (CV) of the individual species and the mixture offers a rapid check of the compatibility of the selected materials. Next, bulk electrolysis of both the individual species and the mixture examines the compatibility and stability of each redox event at time scales and charge states relevant for full cell studies. These initial tests provide a comprehensive understanding of possible interactions while only requiring a minimal amount of active material. If these tests indicate that the materials are compatible, then the method progresses to studies at higher concentrations. A small volume H-type cell with reference electrodes evaluates full cell performance while confirming that the cell accesses the desired redox events, and these studies culminate in a full flow cell study. While flow cell results can be difficult to interpret, the behavior can be easily understood using knowledge gained from the previous steps of the study.

5.3.2 Active Species Selection

Several criteria guided the selection of electrochemical couples for the asymmetric compatibility analysis. The first, and most important, criterion was to exhibit multiple electron transfers, which should result in significant energy density gains. Second, the active species have to be soluble and stable in the same solvent at all relevant oxidation states. Third, the active species need to be commercially available or easy to synthesize in large quantities, facilitating use in a lab-scale flow cell.

Based on these considerations $Fe(bpy)_3(BF_4)_2$ was selected as the low potential active material. $Fe(bpy)_3(BF_4)_2$ exhibits four reversible redox events [25] and has moderate solubility in MeCN. Although $Fe(bpy)_3(BF_4)_2$ undergoes relatively quick capacity fade, this active material is one of only a few rigorously characterized anolyte NAqRFB species capable of multiple electron transfers, [26] and thus is suitable for the demonstration of a $2e^-$ cell over relatively short cycling experiments.

A number of active materials were identified as possible catholyte candidates, including 2,5-di-*tert*-butyl-1,4-bis(2-methoxyethoxy)benzene (DBBB), 4-acetamido-2,2,6,6-tetramethylpiperidine 1-oxyl (A-TEMPO) and Fc1N112-BF_4 (Figure 5.3). Each of these complexes exhibits a single, reversible, positive redox couple and has been well characterized for NAqRFB applications. [14,16,23] To select a catholyte material suitable for a demonstration cell, CV experiments were performed on the individual species and an equi-molar mixture of each active species and $Fe(bpy)_3(BF_4)_2$ (Figure 5.4).

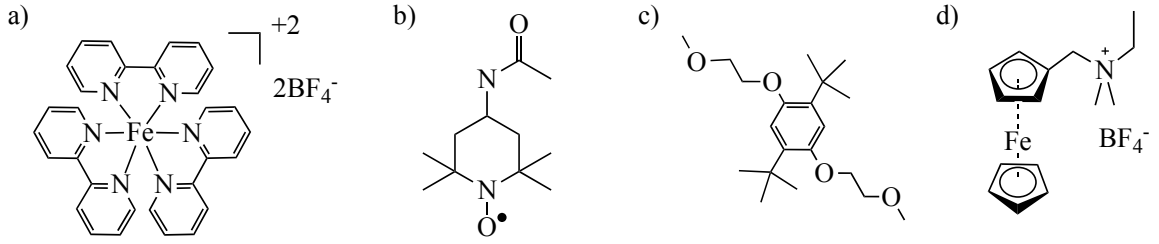

Figure 5.3 Structures of (a) $Fe(bpy)_3(BF_4)_2$ (b) A-TEMPO (c) DBBB and (d) Fc1N112-BF_4.

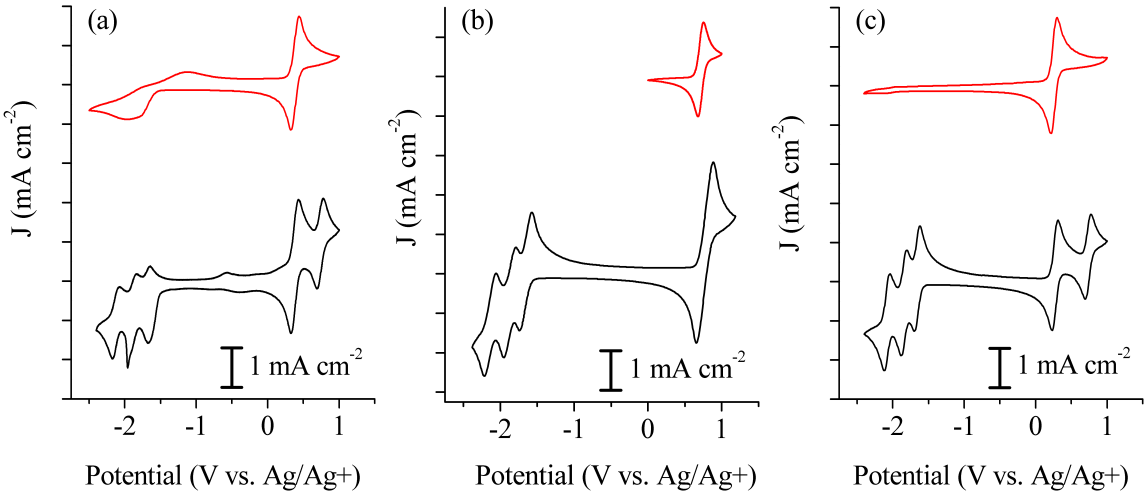

Figure 5.4 CVs of the individual catholyte species (red) and a mixture of $Fe(bpy)_3(BF_4)_2$ and (a) A-TEMPO, (b) DBBB and (c) Fc1N112-BF_4 (black).

A catholyte material suitable for further study will exhibit CV behavior identical to the individual species, indicating no deleterious side reactions with $Fe(bpy)_3(BF_4)_2$, and distinct redox events. A-TEMPO exhibits a single reversible redox event at positive potentials with an irreversible redox event at negative potentials (Figure 5.4a). When mixed with $Fe(bpy)_3(BF_4)_2$ this negative behavior interferes with the negative redox events of $Fe(bpy)_3(BF_4)_2$, resulting in decreased reversibility and side reactions as evidenced by new redox activity at -0.5 V. DBBB is compatible with $Fe(bpy)_3(BF_4)_2$ on the timescale of CV, as the mixture maintains the reversibility of all redox events with no additional side reactions (Figure 5.4b). However, the positive couple of DBBB and $Fe(bpy)_3(BF_4)_2$ are at the same potential. As CV is used to monitor degradation, it would be difficult to separate the behavior of each individual species. Fc1N112-BF_4 exhibits a single reversible redox event at positive potentials with no other redox activity within the relevant window (Figure 5.4c). When mixed with $Fe(bpy)_3(BF_4)_2$ there is no evidence of any interactions, each redox event is distinct and a multi-electron cell can be constructed using these active species. Therefore, Fc1N112-BF_4 was selected as the high potential active material.

Previous reports have demonstrated that this material exhibits excellent electrochemical stability and solubility, making it a promising candidate for NAqRFB applications. [11,23]

5.3.3 Compatibility and Stability of $Fe(bpy)_3(BF_4)_2$ and Fc1N112-BF_4

5.3.3.1 Cyclic Voltammetry

A more detailed CV study of the selected species is shown in Figure 5.5, with CVs of both the individual species and the equi-molar mixture. $Fe(bpy)_3(BF_4)_2$ demonstrates four quasi-reversible redox couples (-2.08, -1.85, -1.65, and 0.74 V vs. Ag/Ag^+) with the single positive redox event (V) associated with the Fe^{II}/Fe^{III} transition and the three negative couples (I, II, III) corresponding to ligand-based processes. [27] Fc1N112-BF_4 exhibits a single redox couple (IV) at 0.28 V vs. Ag/Ag^+, with no other redox activity within the potential window where $Fe(bpy)_3(BF_4)_2$ is active. The redox potentials of the five electron transfer events agree with previous literature reports. [11,23,28] The CV of the mixture is essentially a combination of those for the individual species, indicating that these materials are chemically and electrochemically compatible; at least for the time scale of this CV experiment.

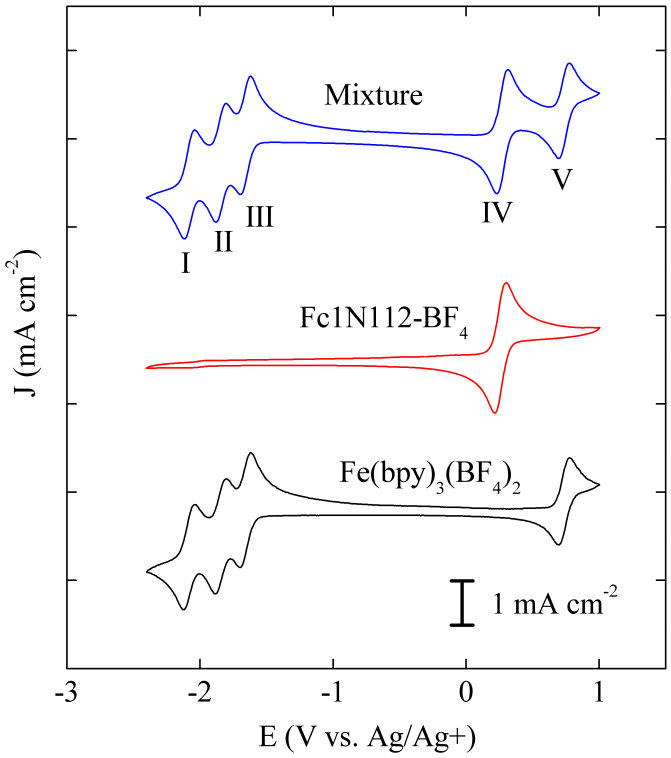

Figure 5.5 CV of 5 mM $Fe(bpy)_3(BF_4)_2$ (black), 5 mM Fc-1N112-BF_4 (red), and an equi-molar mixture of both (blue).

Pairing couple III of $Fe(bpy)_3(BF_4)_2$ with Fc1N112-BF_4 (IV) produces a $1e^-$, 1.92 V cell. This cell offers an increased cell potential over aqueous systems, but NAqRFBs will require even higher voltages (≥ 3 V) for economic feasibility. [29] One of the most promising strategies to increase the energy density of NAqRFBs is to utilize multiple electron transfers. For this system, pairing two of the negative couples of $Fe(bpy)_3(BF_4)_2$ (II and III) with the positive couples of both Fc1N112-BF_4 and $Fe(bpy)_3(BF_4)_2$ (IV and V) results in a $2e^-$ transfer cell. The use of Fc1N112-BF_4 provides the additional capacity required on the catholyte side to afford a multi-electron transfer cell. Additionally, the positive redox couples are easily distinguishable, aiding in visualization of charge/discharge events. The average cell potential for this $2e^-$ system is 2.25 V, which when coupled with the use of multiple redox events, provides a cell with more than twice the theoretical energy density of the analogous single electron system.

5.3.3.2 *Bulk Electrolysis*

Bulk electrolysis experiments were used to further characterize the electrochemical compatibility of $Fe(bpy)_3(BF_4)_2$ and Fc1N112-BF_4 and to assess the feasibility of employing these species in an asymmetric flow cell. Cycling experiments on each individual component establish the baseline stability before cycling a mixture of the two species helps identify any interactions between $Fe(bpy)_3(BF_4)_2$ and Fc1N112-BF_4.

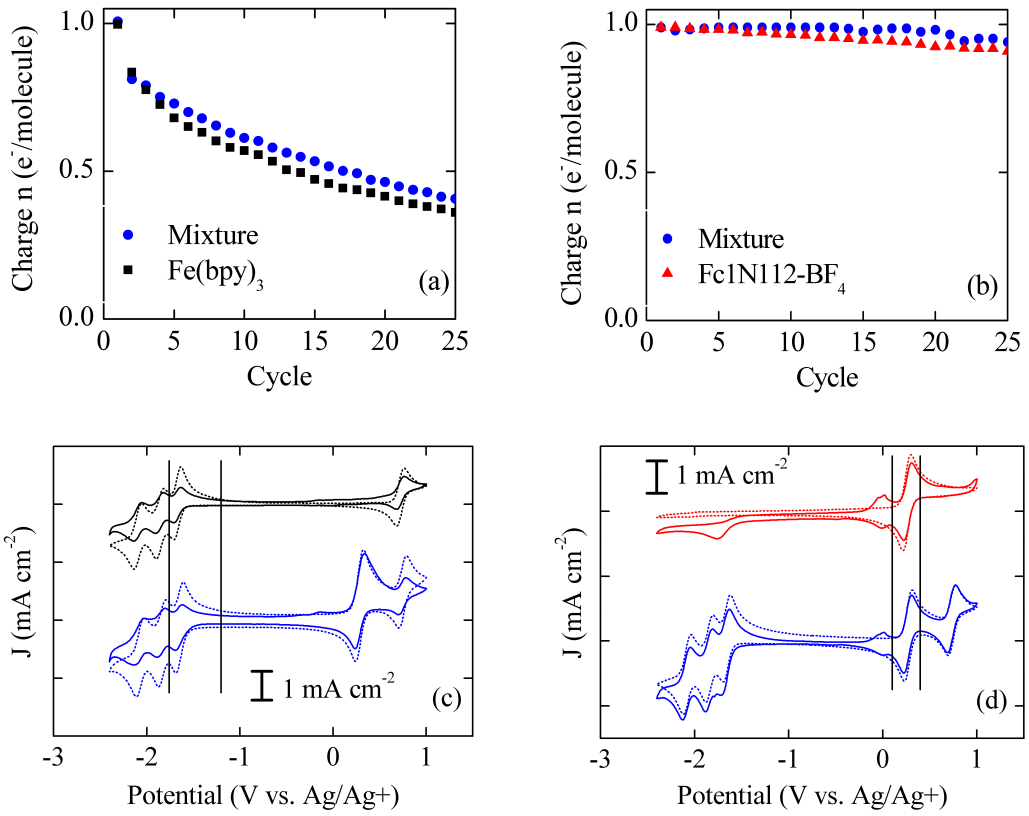

Figure 5.6 Capacity retention measured by bulk electrolysis for $Fe(bpy)_3(BF_4)_2$ (black), Fc1N112-BF_4 (red), and an equi-molar mixture of $Fe(bpy)_3(BF_4)_2$/Fc1N112-BF_4 (blue) through **(a)** a single negative e^- and **(b)** a single positive e^-. **(c, d)** CVs before (dashed) and after cycling (solid) are shown for each case. Black vertical lines denote the potential cutoffs used during cycling: **(c)** -1.2 V, -1.76 V and **(d)** 0.1 V, 0.4 V.

Figure 5.6 shows capacity retention plots and CVs for the $1e^-$ system (III and IV). Through a single negative electron transfer (III), $Fe(bpy)_3(BF_4)_2$ shows significant capacity fade (Figure 5.6a), which is in agreement with previous reports. [26] Examination of the CV after cycling (Figure 5.6c) reveals a decrease in peak heights for all couples associated with $Fe(bpy)_3(BF_4)_2$, supporting the observed capacity fade. No new redox processes arise, suggesting that the reaction byproducts are either electrochemically inactive within the potential window of interest or insoluble in the electrolyte solution. A comparison with the mixture, cycled under identical conditions, reveals near identical capacity fade and similar degradation (indicated by CV), suggesting minimal interactions between the active species; the majority of the capacity fade arises from $Fe(bpy)_3(BF_4)_2$ instability. The Fc1N112-BF_4 couple does lose some peak intensity, indicating minor interactions with the $Fe(bpy)_3(BF_4)_2$, however, this couple does not play a role in the anolyte cell chemistry and should have minimal effect on cell performance. Analysis of the electrochemical stability of the single positive couple of Fc1N112-BF_4 (IV) reveals highly stable cycling behavior (Figure 5.6b), as expected based on previous reports. [11] CVs after cycling (Figure 5.6d) show a minimal decrease in peak height for the Fc1N112-BF_4, which correlates well with the observed capacity fade. For both the single species and the mixture, electrochemically active degradation products are observed at 0 and -1.7 V vs. Ag/Ag^+. These peaks could be due to detachment of the pendant ionic group from Fc1N112-BF_4 as the peak at 0 V vs. Ag/Ag^+ matches the redox potential of ferrocene. [30] No substantial changes are observed for the peaks associated with $Fe(bpy)_3(BF_4)_2$. In all cases, the potential curves match the potentials expected based on the initial CV. Taken as a whole, the near identical capacity fade and degradation products observed after cycling for both the single active species and the

mixture establish that Fc1N112-BF_4 and $Fe(bpy)_3(BF_4)_2$ are compatible chemistries for use in a $1e^-$ asymmetric NAqRFB.

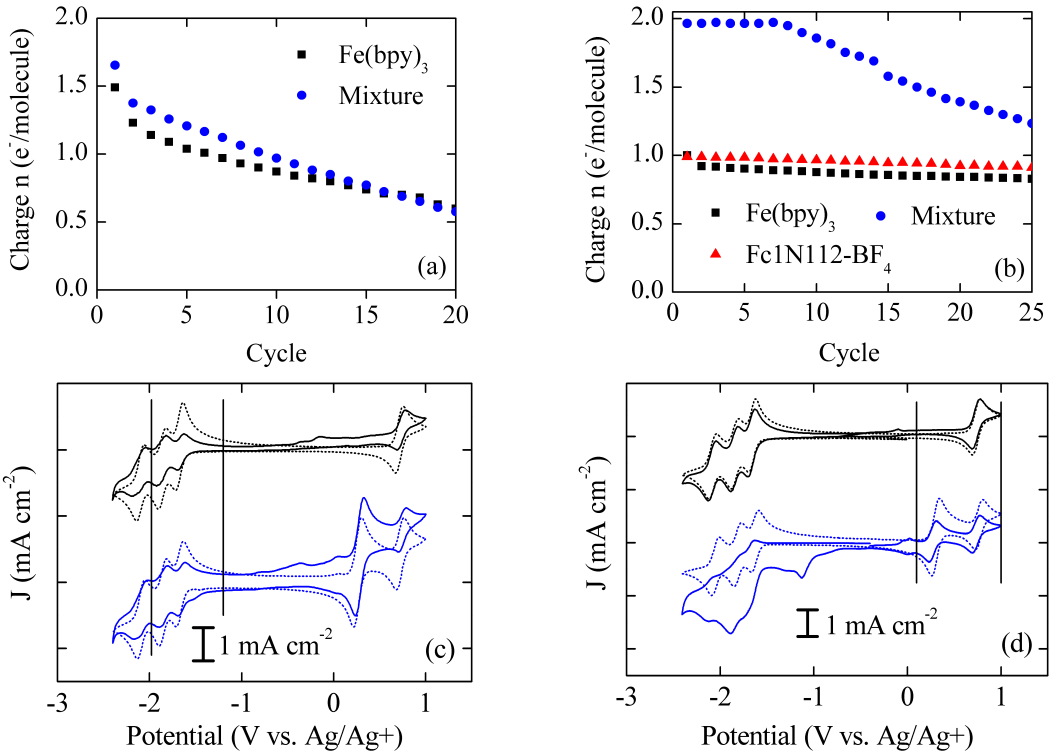

Figure 5.7 Capacity retention measured by bulk electrolysis for $Fe(bpy)_3(BF_4)_2$ (black), Fc1N112-BF_4 (red) and an equi-molar mixture of $Fe(bpy)_3$/Fc1N112-BF_4 (blue) through **(a)** two negative e^- and **(b)** both one and two positive e^-. **(c, d)** CVs before (dashed) and after cycling (solid) are shown for each case. Black vertical lines denote the potential cutoffs used during cycling: **(c)** -1.2 V, -1.98 V and **(d)** 0.1 V, 1.0 V.

The $2e^-$ system utilizes two negative couples (II and III) from $Fe(bpy)_3(BF_4)_2$ and the positive couples (IV and V) of both Fc1N112-BF_4 and $Fe(bpy)_3(BF_4)_2$. Figure 5.7 presents cycling data and CVs for the $2e^-$ bulk electrolysis experiments. Cycling through the two negative couples (II and III) reveals minimal interactions between the active species (Figure 5.7a and Figure 5.7c). For both $Fe(bpy)_3(BF_4)_2$ and a mixture of the two species, the capacity fade profile is very similar (Figure 5.7a). In both cases, cycling never reaches the theoretical capacity due to

the close proximity of couple I; a voltage cutoff ensured that the cell cycled primarily through couples II and III, subsequently limiting charge capacity. Examination of the CV after cycling (Figure 5.7c) shows a decrease in the peak height of the $Fe(bpy)_3(BF_4)_2$ couples, similar to that observed for the $1e^-$ transfer. In the case of the mixture, evidence of minor degradation products appear in the CV at the same potentials as for Fc1N112-BF_4 (Figure 5.6d), which suggests that the active species interact to an extent. Despite the development of these new irreversible electrochemical processes, the cycling behavior confirms that these two redox couples are compatible for use on the negative side of a multi-electron transfer cell.

Cycling data through the two positive redox couples shows the highest degree of interactions observed for these two chemistries. Bulk electrolysis through the single positive couple of each individual species reveals stable cycling behavior (Figure 5.7b), and CVs after cycling show minimal degradation for both Fc1N112-BF_4 (Figure 5.6d) and $Fe(bpy)_3(BF_4)_2$ (Figure 5.7d). The mixed positive couples, however, exhibit significant capacity fade after the first 8 cycles (Figure 5.7b). Analysis of the CV after cycling shows clear evidence of degradation (Figure 5.7d). Peak heights for both positive couples decrease while those for the negative couples of $Fe(bpy)_3(BF_4)_2$ degrade completely. Despite the significant capacity fade and interactions observed over time for the mixture at positive potentials, the cell maintains a constant capacity for at least the first 8 cycles, and therefore, affords a cell to demonstrate a multi-electron system.

5.3.4 Full Cell Performance of $Fe(bpy)_3(BF_4)_2$ and Fc1N112-BF_4

The full cells (H-cell and flow) in this study employ a stable Daramic separator. Although this separator has poor selectivity, due to the limited stability of anion exchange

membranes in non-aqueous solvents, [20,31] this selection minimizes interactions between the separator and the active species, eliminating separator degradation as a performance decay mechanism.

5.3.4.1 H-cell Cycling

Stationary H-type cell cycling experiments demonstrate cell cycling of the $1e^-$ and $2e^-$ $Fe(bpy)_3(BF_4)_2$/Fc1N112-BF_4 systems at non-dilute concentrations in the absence of flow. These H-cell experiments utilize quasi-reference electrodes in each chamber to monitor electrode potentials and confirm the accessed redox couples during cycling. Both sides of the cell contained an identical mixture of $Fe(bpy)_3(BF_4)_2$/Fc1N112-BF_4 to ensure any capacity fade is due primarily to degradation of the active species, not irreversible crossover. Crossover will occur due to the formation of concentration gradients during cycling, but should only lead to decreased coulombic efficiency, not capacity fade. Figure 5.8a and Figure 5.8b show potential curves for the $1e^-$ and $2e^-$ H-cell cycling experiments, respectively. Figure 5.8c and Figure 5.8d display electrode potentials for the $1e^-$ and $2e^-$ cells, respectively.

For the $1e^-$ system, the negative electrode potential matches the potential of couple III, while the positive electrode potential matches that for couple IV. These results confirm that the $Fe(bpy)_3(BF_4)_2$/Fc1N112-BF_4 cell accesses only the desired couples, further establishing the compatibility of the selected active species. Figure 5.8a does reveal a large cell overpotential (~0.45 V) during cycling, comparable to other H-cell cycling reports. [4] Ohmic losses constitute a majority (~0.4 V) of the observed overpotential, due to the wide inter-electrode separation, and the remaining overpotential is due to activation and concentration polarization losses. Because of these significant overpotentials, the average voltaic efficiency is only 60%. The coulombic

efficiency is also relatively low (69%) due to the high permeability of the Daramic separator.

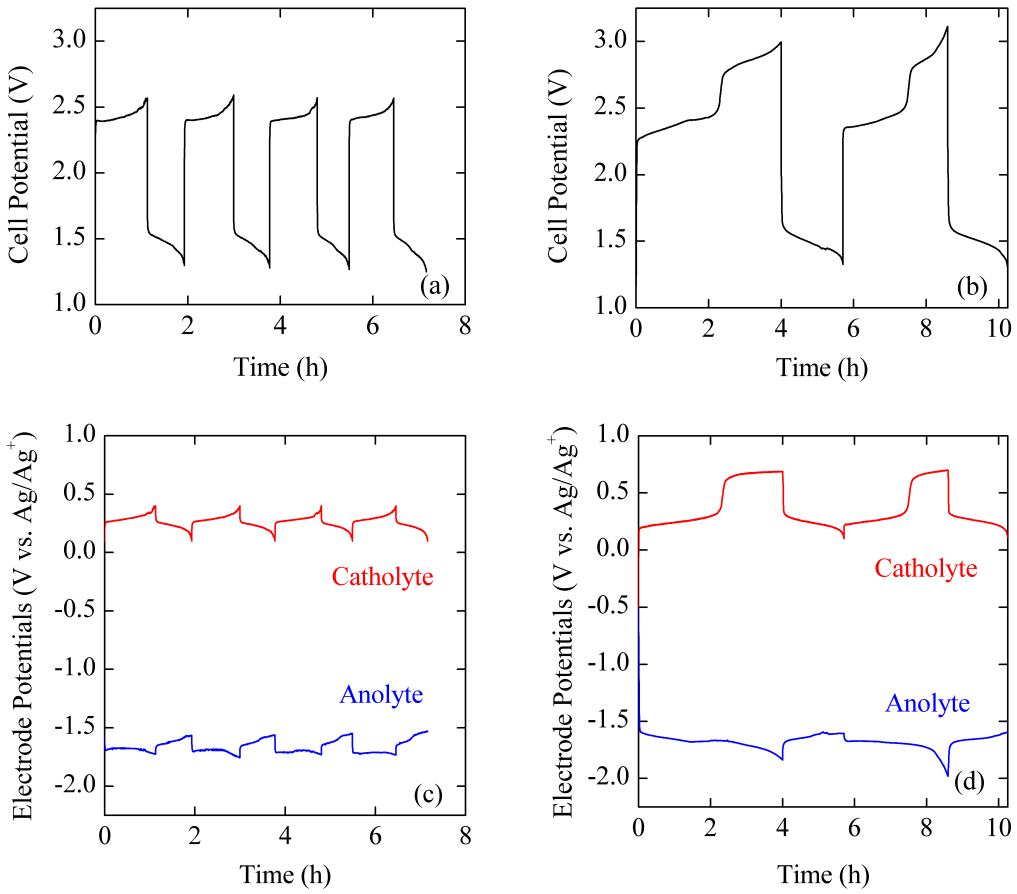

Figure 5.8 H-cell cycling data for the $Fe(bpy)_3(BF)_4$/Fc1N112-BF_4 system showing the total cell potential for the **(a)** $1e^-$ and **(b)** $2e^-$ experiments, and the catholyte (red) and anolyte (blue) potentials for the **(c)** $1e^-$ and **(d)** $2e^-$ H-cells, measured using Ag/Ag^+ quasi-reference electrodes in each chamber.

Quasi-reference electrodes in the $2e^-$ H-cell experiment confirm that the cell accesses all of the desired couples (II, III, IV, and V) upon charging. Considering Figure 5.8d, the catholyte first charges through the positive couple IV of Fc1N112-BF_4 at 0.28 V vs. Ag/Ag^+, and once couple IV is exhausted, the cell activates couple V of $Fe(bpy)_3(BF_4)_2$ at 0.75 V vs. Ag/Ag^+. Both plateaus are visible in the charging profile and match with the potentials expected based on CV. For the negative side, the switch from couples III to II of $Fe(bpy)_3(BF_4)_2$ is less pronounced due

to the proximity of these couples, but a change in the slope of the charging curve after ~2 h indicates that the cell accesses both of these redox couples. Unfortunately, on discharge the cell only accesses the positive couple IV of Fc1N112-BF_4. The separator allows significant self-discharge, and a high rate of crossover caused the charged $Fe(bpy)_3(BF_4)_3$ to fully self-discharge before partaking in an electrode reaction. The average coulombic efficiency for the $2e^-$ cell is 50%, due to the high rate of crossover, and the voltaic efficiency is 58%. Similar to the $1e^-$ cell, this is primarily due to a large cell overpotential. For the $2e^-$ cell, however, the inability to discharge through both couples results in an even lower coulombic efficiency. Despite the inability of this cell to fully discharge, these results demonstrate that the system can access the desired electrons from each of the active species.

5.3.4.2 Flow Cell Studies

Our electrochemical studies culminate in flow cell cycling experiments, transitioning the vetted active materials to a laboratory prototype. Flow cells achieve higher current densities than H-cells, due to a significantly lower ASR, overcoming crossover limitations and offering higher voltaic efficiencies. A small-scale flow cell demonstrates $1e^-$ cycling for a battery employing redox couples III and IV. Charge/discharge profiles in Figure 5.9a exhibit a single potential plateau that corresponds to the expected $1e^-$ process. The theoretical capacity of the $1e^-$ transfer cell was 26.8 mAh, and the flow cell accesses 66% of this capacity during the first cycle. This relatively low depth-of-charge is a result of the upper cell potential cutoff of 2.01 V, selected to minimize accessing additional redox couples (II or V).

Figure 5.9b illustrates the charge and discharge capacities as a function of cycle number. Over the first 5 cycles, the charge capacity is significantly greater than the discharge capacity,

resulting in coulombic efficiencies < 80%, as depicted in Figure 5.9c. Active species crossover and subsequent self-discharge through the Daramic separator, combined with active species degradation, led to the low coulombic efficiencies. The coulombic efficiency improves from 70% to 90% over 20 cycles, with a mean value of 81%, due to decreasing depths-of-charge as the experiment progresses. A prior NAqRFB study employing a Daramic separator with similar active species concentrations and current densities reported comparable coulombic efficiencies. [32] The voltaic efficiency is nearly constant as a function of cycle number, with a mean value of 91 ± 0.2%. The voltaic efficiency is relatively high due to two factors. First, the Daramic separator exhibits a lower ASR compared to other NAqRFB separators [11,13,16,33–35] as a result of its high porosity and the high conductivity of the electrolyte phase. Second, the voltaic efficiency is high in comparison to many AqRFBs due to lower current densities and a higher cell voltage; overpotential losses constitute a smaller fraction of the total cell potential.

Capacity fade for the flow cell experiment agrees with the limited stability of $Fe(bpy)_3(BF_4)_2$ observed during bulk electrolysis experiments. For couple III of $Fe(bpy)_3(BF_4)_2$, the capacity fades to 47% of its initial charge capacity after 20 bulk electrolysis cycles. Since the flow cell never reaches the theoretical capacity, flow cell cycling demonstrates slightly slower fade to only 62% of its initial charge capacity over 20 cycles.

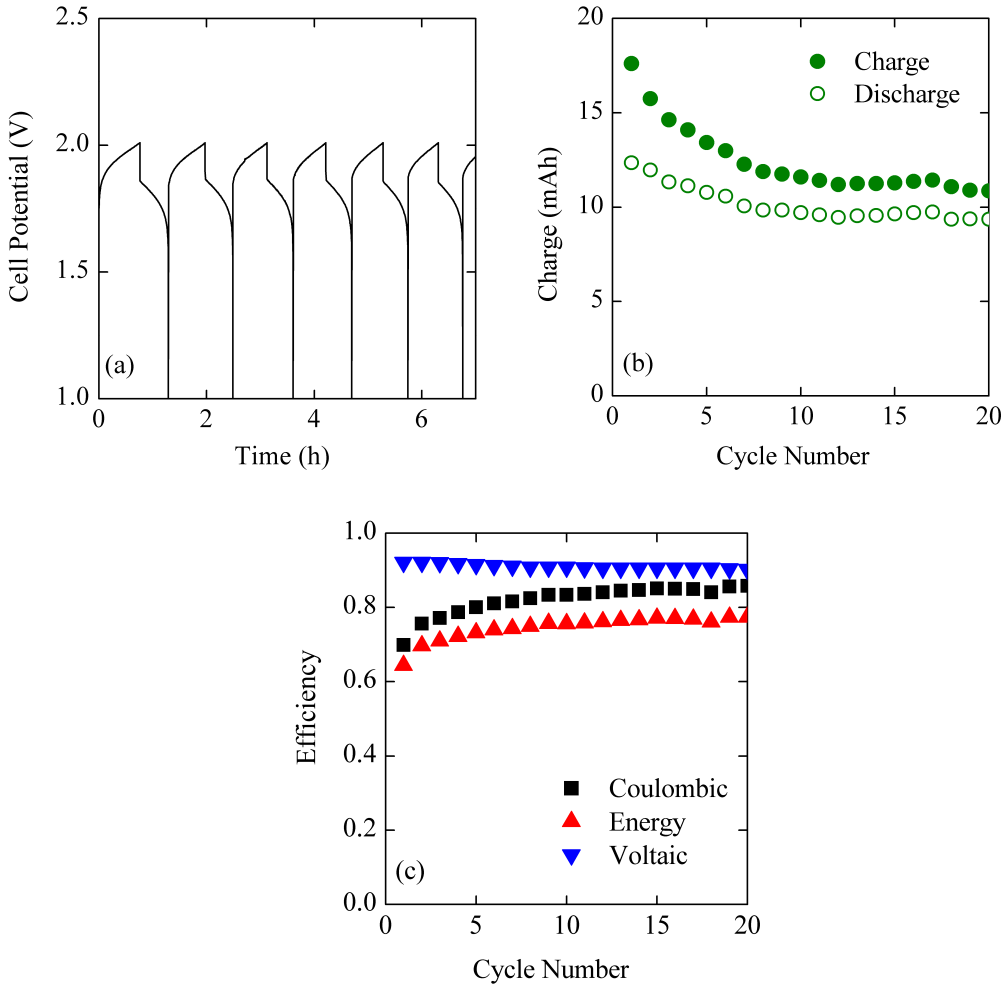

Figure 5.9 $Fe(bpy)_3(BF)_4$/Fc1N112-BF_4 1e- transfer flow cell cycling performance: **(a)** charge and discharge potential curves as a function of time, **(b)** charge (●) and discharge (○) capacities as a function of cycle number, and **(c)** coulombic (■), energy (▲), and voltaic (▼) efficiencies as a function of cycle number. The theoretical cell capacity is 26.8 mAh.

A $2e^-$ flow cell study completes the electrochemical analysis of the $Fe(bpy)_3(BF_4)_2$/Fc1N112-BF_4 system. As shown in Figure 5.10a, the $2e^-$ flow cell accesses all available redox processes during both charge and discharge, and cycle 1 displays a unique charging profile due to the 4 accessible redox couples in the $Fe(bpy)_3(BF_4)_2$/Fc1N112-BF_4 $2e^-$ system. Consider Figure 5.10b, which plots cell potential as a function of capacity for only the first charging process. The initial charging plateau accesses redox couples III and IV. This

behavior is consistent with observations during charging of the $1e^-$ transfer flow cell. As the cell continues to charge, however, a second plateau appears; a non-differentiable decrease in cell potential characterizes the start of the second plateau. As the electrodes continue to polarize, redox couples II, III, and IV become thermodynamically accessible, but *not* couple V. Eventually, couple IV is exhausted, and a sharp increase in cell potential marks the start of a third plateau. The third plateau then accesses couples II, III, and V. Finally, for a fourth plateau, only couples II and IV participate in charge transfer reactions because all other couples have been completely exhausted. Upon cell discharge, two major plateaus appear (Figure 5.10a), corresponding to the reduction of couple V, followed by the reduction of couple IV, but detailed processes are indistinguishable.

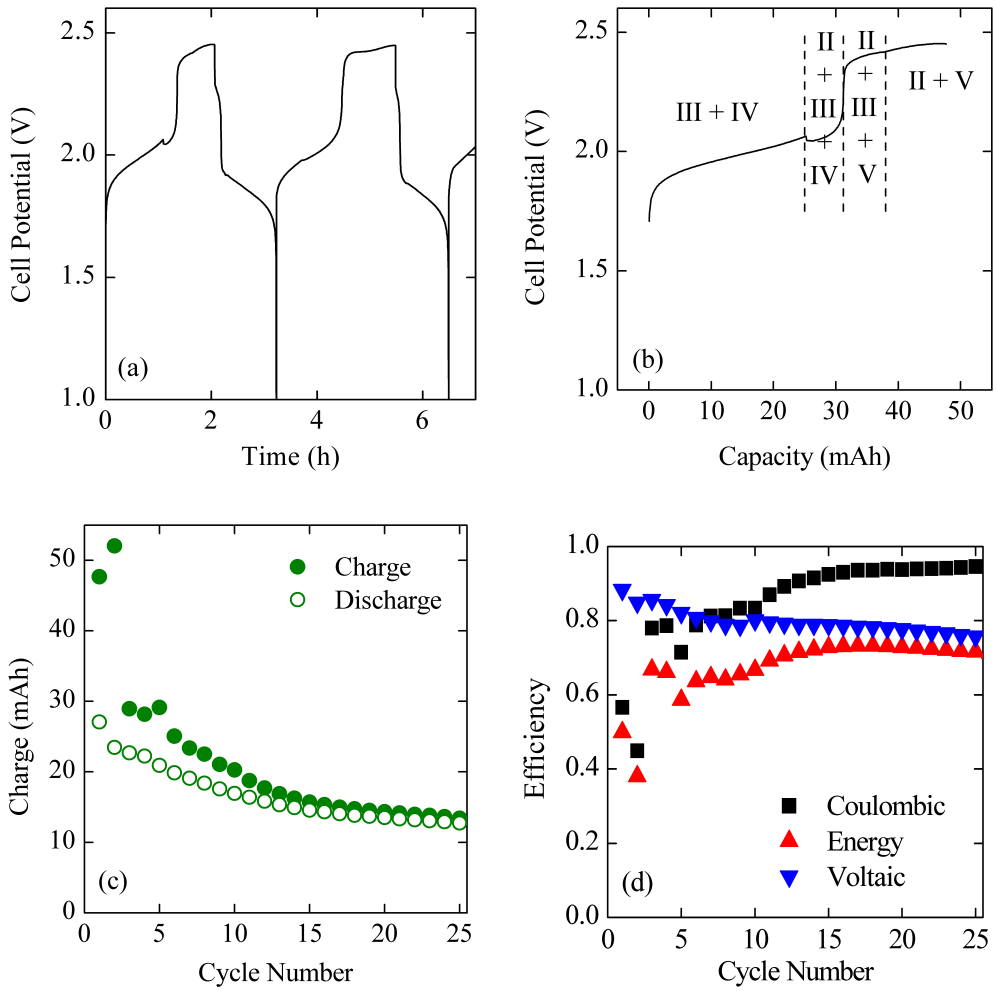

Figure 5.10 $Fe(bpy)_3(BF_4)_2$/Fc1N112-BF_4 $2e^-$ transfer flow cell cycling performance: **(a)** Charge and discharge curves as a function of time, **(b)** Charging voltage profile as a function of capacity for the 1st cycle, **(c)** Charge (●) and discharge (○) capacities as a function of cycle number, and **(d)** Coulombic (■), energy (▲), and voltaic (▼) efficiencies as a function of cycle number. The theoretical cell capacity is 53.6 mAh.

The unconventional $2e^-$ charge behavior results from the presence of two pairs of unequally separated redox couples. The decrease in cell potential at ~25 mAh during cycle 1 charging (see Figure 5.10b) is unusual, but an associated decrease in concentration overpotential reconciles the behavior. During the first charge plateau, the negative electrode continuously consumes reactant for couple III, and the negative electrode overpotential increases to maintain constant current, subsequently increasing the total cell potential. Unique to this multi-electron

transfer system, at a significantly large overpotential on the negative electrode, couple II becomes nearly instantaneously accessible. During the second plateau, the negative electrode could reduce *either* couple II *or* III, increasing reactant concentration as compared to the end of the first plateau. With an increase in available reactant, the negative electrode concentration overpotential decreases, subsequently decreasing the overall cell potential instantaneously at ~25 mAh. Bulk electrolysis cycling curves confirm this behavior.

The theoretical capacity of the $2e^-$ flow cell is 53.6 mAh. The upper cell potential cutoff of 2.45 V prohibits accessing the unstable couple I, but also prohibits the cell from accessing 100% of its theoretical capacity. Figure 5.10b indicates that the first two charge cycles accessed 89% and 97% of the theoretical cell capacity, respectively. Despite the high depth-of-charge during the first two cycles, the coulombic efficiencies for these cycles are 57% and 45% (Figure 5.10c). The low coulombic efficiencies are a result of crossover through the Daramic separator and rapid active species degradation. The short discharge plateau for cycle 1 (Figure 5.10a), demonstrates that discharge processes incorporating redox couple V are short-lived. During cycling, a large volume (~2 mL) of electrolyte migrates from the catholyte to the anolyte, suggesting that active material migration plays a significant role in crossover. The higher cell potential of the $2e^-$ system relative to the 1e- system provides a large driving force for active species migration during cycling. Diffusive crossover of active material also likely plays a significant role in the low coulombic efficiency during cycles 1 and 2.

Beyond cycle 2, charge capacities decrease significantly, likely caused by active material degradation and low depths-of-charge. Bulk electrolysis experiments over 20 cycles exhibit rapid capacity degradation down to 71% and 36% for the $2e^-$ catholyte and anolyte redox couples, respectively. Further, the distinct charge plateaus identified in cycle 1 merge in subsequent

cycles, convoluting specific redox processes in late cycle charge plateaus. This $2e^-$ transfer system suffers from poor active material stability and high crossover rates, but, nonetheless, demonstrates for the first time the unique charging characteristics associated with multi-electron RFBs.

5.3.5 Compatibility Analysis Applied to $Co(BPI)_2$ and Fc

The ultimate application of the developed compatibility analysis would be the use of this procedure to design a stable, high concentration, multi-electron transfer NAqRFB. While further active species development is necessary to achieve all of these criteria, this procedure can be extended beyond the demonstration system to identify a more stable multi-electron transfer cell. As discussed in Chapter 3, BPI metal complexes exhibit impressive stability through two negative electron transfers. The last section of this chapter will discuss the development of a multi-electron full cell utilizing Co(**L5**)$_2$ as the anolyte material.

To select which metal center to pair with the BPI ligand, the stability of both the positive and negative couples were considered. As shown in Section 3.3.4, Co, Fe and Ni all exhibit excellent negative stability (Figure 3.7d). Of these materials, Co(**L5**)$_2$ demonstrates the best positive stability (Figure 3.12) and was therefore selected as the anolyte material. It was then necessary to identify a suitable catholyte material for this system. Ferrocene (Fc) is an organometallic complex that is commonly used as a standard in non-aqueous electrochemistry. While it has limited solubility in acetonitrile, it exhibits high reversibility and electrochemical stability. [36] Structures of both molecules are shown in Figure 5.11.

A CV of a mixture of Co(**L5**)$_2$ and Fc demonstrates the compatibility of these materials on short time scales (Figure 5.11c), with redox couples I-III representative of Co(**L5**)$_2$ and IV

associated with Fc. No interactions are observed, and each redox event is distinct and reversible. It should be noted that the peak height of the Fc couple (IV) is significantly larger than the peak heights for the Co(**L5**)$_2$ couples due to the smaller size and therefore increased diffusivity of Fc. A multi-electron cell can be constructed with these chemistries by utilizing the negative couples of Co(**L5**)$_2$ (I and II) as the anolyte and the positive couples of both Co(**L5**)$_2$ and Fc (III and IV) as the catholyte. This configuration requires a mixed electrolyte, motivating the use of the developed compatibility analysis to fully assess and understand the full cell cycling performance.

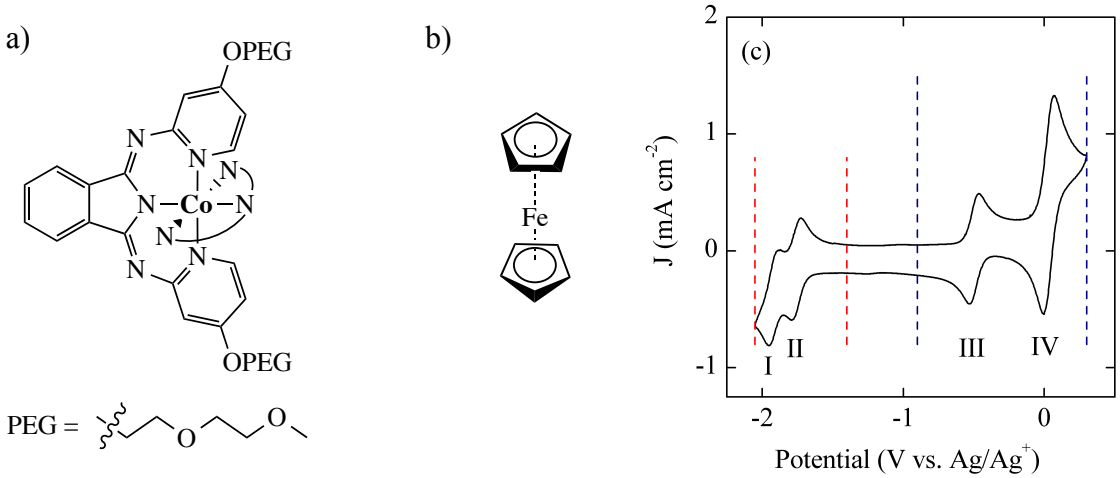

Figure 5.11 Structures of **(a)** Co(**L5**)$_2$ and **(b)** Fc. **(c)** CV of an equi-molar mixture of Co(**L5**)$_2$/Fc with dashed lines representing the couples access by the anolyte (red) and the catholyte (blue). Redox couples I-III correspond to Co(**L5**)$_2$ and IV to Fc.

Bulk electrolysis performance of Co(**L5**)$_2$ can be found in Sections 3.3.4 and 3.3.7. This material exhibits no capacity fade over 50 cycles at either positive or negative potentials. Fc exhibits similarly high stability, reaching 100 cycles before fading to 80% of the initial charge capacity. [37] Individually, each of these materials exhibits high stability, and an initial CV test of the mixture indicates that they are compatible, so the next step was to perform bulk

electrolysis of the mixture. Figure 5.12b reveals that the mixture also displays excellent stability, with no fade observed over 50 cycles. Potential curves (Figure 5.12c) indicate that the material is fully accessing both the positive couple of Co(**L5**)$_2$ (III) and that of Fc (IV) with high reversibility. Furthermore, a CV after cycling (Figure 5.12c) reveals no significant changes to the electrochemistry, which corresponds well to the excellent capacity retention.

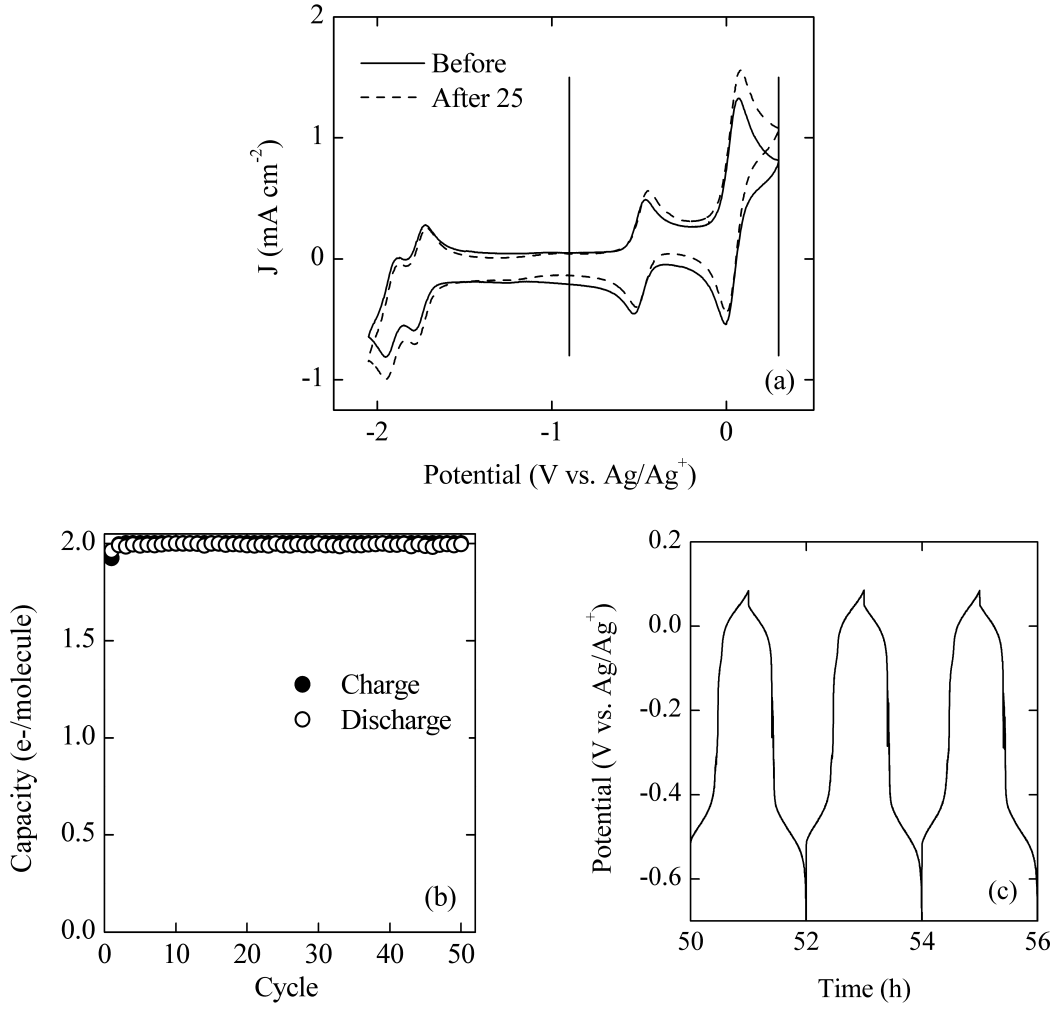

Figure 5.12 Co(**L5**)$_2$/Fc 2e$^-$ transfer bulk electrolysis performance: **(a)** CV of a 2 mM equi-molar mixture of Co(**L5**)$_2$ and Fc before and after cycling. Solid vertical lines represent the potential cutoffs used during cycling: -0.9 V, 0.3 V. **(b)** Capacity retention over 50 cycles. **(c)** Potential curves for cycles 25-27.

The bulk electrolysis experiments confirm that these materials are compatible at the charge states that will be accessed during cycling, motivating the demonstration of a full 2e$^-$

transfer cell. Results from a static H-cell test are shown in Figure 5.13. An analysis of the capacity retention reveals that this cell cycles an impressive 45 times before reaching 80% of the initial capacity. Potential curves (Figure 5.13b) reveal that the positive side of the cell is only partially accessing couple III, resulting in the observed capacity fade. This fade can be partially reconciled with the bulk electrolysis results by considering the relatively slow kinetics of Co oxidation. [37,38] In a bulk electrolysis experiment the counter electrode has no limitations on the potentials it can access to drive the reaction. In a full cell experiment, however, the counter electrode is limited to the potential range of the anolyte reactions. Therefore, in the full cell studies the reaction is not driven fast enough to access the full $Co(L5)_2$ positive couple. Experiments at higher currents exhibit no plateau for $Co(L5)_5$ in the catholyte, confirming this behavior.

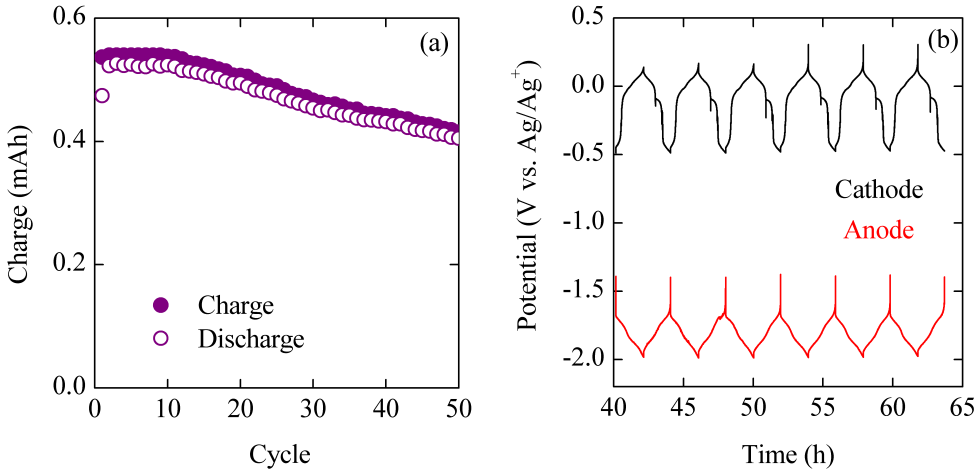

Figure 5.13 Co(**L5**)$_2$/Fc 2e$^-$ full cell cycling: **(a)** Capacity retention. **(b)** Electrode potentials for both the cathode (black) and anode (red) for cycles 25-30. Theoretical capacity for 2e$^-$ is 0.54 mAh.

These results successfully demonstrate the versatility of the developed analysis and how it can be used to develop stable, multi-electron transfer NAqRFBs. Due to the limited availability of Co(**L5**)$_2$ and its low solubility, these studies were not transferred to a full flow system.

5.4 Conclusions

In this chapter, I established a systematic electrolyte compatibility study to investigate possible interactions between different active species by examining the stability of both active materials, across all relevant oxidation states, both individually and as mixtures. After establishing criteria for the selection of the active materials and performing initial CV studies, a proof of concept multi-electron NAqRFB was designed employing Fe(bpy)$_3$(BF$_4$)$_2$ and Fc1N112-BF$_4$ as the anolyte and catholyte, respectively. CV, bulk electrolysis, and H-cell experiments confirmed the feasibility of 1e$^-$ and 2e$^-$ transfer cycling prior to engaging a flow cell study. The 1e$^-$ flow cell cycled as predicted from the bulk electrolysis and H-cell experiments. The 2e$^-$ NAqRFB successfully accessed all desired redox couples, revealing a unique progression of charge and discharge plateaus. Results from the systematic electrochemical studies were used to explain the complex charging phenomena, and each plateau correlated to specific redox processes observed by CV. This concept was then extended to develop a more stable 2e$^-$ system using Co(**L5**)$_2$ and Fc. Overall, the developed methodology was successfully applied to demonstrate the first 2e$^-$ full flow NAqRFB. It can be easily extended to other promising redox chemistries as they emerge, including all-organic, all-MCC, and mixed MCC/organic systems, to facilitate the development of stable, soluble, multi-electron NAqRFBs.

5.5 Acknowledgements

I would like to thank Dr. Jarrod Milshtein from Prof. Fikile Brushett's group at MIT for his collaborative efforts on this project. Jarrod performed the flow cell studies shown in this chapter. I would also like to thank Dr. Tanya Breault who established and assisted with the synthetic efforts. This work was funded by the Joint Center for Energy Storage Research (JCESR) with additional support from the National Science Foundation Graduate Research Fellowship Program.

5.6 References

[1] C.S. Sevov, R.E.M. Brooner, E. Chénard, R.S. Assary, J.S. Moore, J. Rodríguez-López, M.S. Sanford, Evolutionary design of low molecular weight organic anolyte materials for applications in nonaqueous redox flow batteries, J. Am. Chem. Soc. 137 (2015) 14465–14472.

[2] P.J. Cabrera, X. Yang, J.A. Suttil, R.E.M. Brooner, L.T. Thompson, M.S. Sanford, Evaluation of tris-bipyridine chromium complexes for flow battery applications: Impact of bipyridine ligand structure on solubility and electrochemistry, Inorg. Chem. 54 (2015) 10214–10223.

[3] Q. Liu, A.E.S. Sleightholme, A. a. Shinkle, Y. Li, L.T. Thompson, Non-aqueous vanadium acetylacetonate electrolyte for redox flow batteries, Electrochem. Commun. 11 (2009) 2312–2315.

[4] P.J. Cabrera, X. Yang, J.A. Suttil, K.L. Hawthorne, R.E.M. Brooner, M.S. Sanford, L.T. Thompson, Complexes containing redox noninnocent ligands for symmetric, multielectron transfer nonaqueous redox flow batteries, J. Phys. Chem. C. 119 (2015) 15882–15889.

[5] R.A. Potash, J.R. McKone, S. Conte, H.D. Abruña, On the benefits of a symmetric redox flow battery, J. Electrochem. Soc. 163 (2016) A338–A344.

[6] X. Xing, Y. Zhao, Y. Li, A non-aqueous redox flow battery based on tris(1,10-phenanthroline) complexes of iron(II) and cobalt(II), J. Power Sources. 293 (2015) 778–783.

[7] C.G. Armstrong, K.E. Toghill, Cobalt(II) complexes with azole-pyridine type ligands for non-aqueous redox-flow batteries: tunable electrochemistry via structural modification, J. Power Sources. 349 (2017) 121–129.

[8] C.S. Sevov, S.L. Fisher, L.T. Thompson, M.S. Sanford, Mechanism-based development of a low-potential, soluble, and cyclable multielectron anolyte for nonaqueous redox flow

batteries, J. Am. Chem. Soc. 138 (2016) 15378–15384.

[9] S.M. Laramie, J.D. Milshtein, T.M. Breault, F.R. Brushett, L.T. Thompson, Performance and cost characteristics of multi-electron transfer, common ion exchange non-aqueous redox flow batteries, J. Power Sources. 327 (2016) 681–692.

[10] P.J. Cappillino, H.D. Pratt, N.S. Hudak, N.C. Tomson, T.M. Anderson, M.R. Anstey, Application of redox non-innocent ligands to non-aqueous flow battery electrolytes, Adv. Energy Mater. 4 (2014) 1300566.

[11] X. Wei, L. Cosimbescu, W. Xu, J.Z. Hu, M. Vijayakumar, J. Feng, M.Y. Hu, X. Deng, J. Xiao, J. Liu, V. Sprenkle, W. Wang, Towards high-performance nonaqueous redox flow electrolyte via ionic modification of active species, Adv. Energy Mater. 5 (2014) 1400678.

[12] J.D. Milshtein, A.P. Kaur, M.D. Casselman, J.A. Kowalski, S. Modekrutti, P. Zhang, N.H. Attanayake, C.F. Elliott, S.R. Parkin, C. Risko, F.R. Brushett, S.A. Odom, High current density, long duration cycling of soluble organic active species for non-aqueous redox flow batteries, Energy Environ. Sci. 9 (2016) 3531–3543.

[13] X. Wei, W. Xu, J. Huang, L. Zhang, E. Walter, C. Lawrence, M. Vijayakumar, W.A. Henderson, T. Liu, L. Cosimbescu, B. Li, V. Sprenkle, W. Wang, Radical compatibility with nonaqueous electrolytes and its impact on an all-organic redox flow battery, Angew. Chemie Int. Ed. 54 (2015) 8684–8687.

[14] J.D. Milshtein, J.L. Barton, R.M. Darling, F.R. Brushett, 4-acetamido-2,2,6,6-tetramethylpiperidine-1-oxyl as a model organic redox active compound for nonaqueous redox flow batteries, J. Power Sources. 327 (2016) 151–159.

[15] C.S. Sevov, S.K. Samaroo, M.S. Sanford, Cyclopropenium salts as cyclable, high-potential catholytes in nonaqueous media, Adv. Energy Mater. 7 (2016) 1602027.

[16] F.R. Brushett, J.T. Vaughey, A.N. Jansen, An all-organic non-aqueous lithium-ion redox flow battery, Adv. Energy Mater. 2 (2012) 1390–1396.

[17] W. Wang, W. Xu, L. Cosimbescu, D. Choi, L. Li, Z. Yang, Anthraquinone with tailored structure for a nonaqueous metal-organic redox flow battery, Chem. Commun. 48 (2012) 6669–71.

[18] J. Mun, M.J. Lee, J.W. Park, D.J. Oh, D.Y. Lee, S.G. Doo, Non-aqueous redox flow batteries with nickel and iron tris(2,2′-bipyridine) complex electrolyte, Electrochem. Solid-State Lett. 15 (2012) A80-A82.

[19] N.S. Hudak, L.J. Small, H.D. Pratt, T.M. Anderson, Through-plane conductivities of membranes for nonaqueous redox flow batteries, J. Electrochem. Soc. 162 (2015) A2188–A2194.

[20] S.H. Shin, S.H. Yun, S.H. Moon, A review of current developments in non-aqueous redox flow batteries: characterization of their membranes for design perspective, RSC Adv. 3 (2013) 9095–9116.

[21] L. Su, R.M. Darling, K.G. Gallagher, W. Xie, J.L. Thelen, A.F. Badel, J.L. Barton, K.J. Cheng, N.P. Balsara, J.S. Moore, F.R. Brushett, An investigation of the ionic conductivity

and species crossover of lithiated Nafion N117 in nonaqueous electrolytes, J. Electrochem. Soc. 163 (2016) A5253–A5262.

[22] J. Park, M. Lee, S. Hwang, D. Lee, D. Oh, Redox flow battery: US2012/0171541 A1, 2012.

[23] L. Cosimbescu, X. Wei, M. Vijayakumar, W. Xu, M.L. Helm, S.D. Burton, C.M. Sorensen, J. Liu, V. Sprenkle, W. Wang, Anion-tunable properties and electrochemical performance of functionalized ferrocene compounds, Sci. Rep. 5 (2015) 14117.

[24] L. Zhang, Z. Zhang, P.C. Redfern, L.A. Curtiss, K. Amine, Molecular engineering towards safer lithium-ion batteries: a highly stable and compatible redox shuttle for overcharge protection, Energy Environ. Sci. 5 (2012) 8204.

[25] M. Morita, Y. Tanaka, K. Tanaka, Y. Matsuda, T. Matsumura-Inoue, Electrochemical oxidation of ruthenium and iron complexes at rotating ring disk electrode in acetonitrile solution, Chem. Soc. Japan. 61 (1988) 2711–2714.

[26] M.H. Chakrabarti, R.A.W. Dryfe, E.P.L. Roberts, Evaluation of electrolytes for redox flow battery applications, Electrochim. Acta. 52 (2007) 2189–2195.

[27] J. England, C.C. Scarborough, T. Weyhermüller, S. Sproules, K. Wieghardt, Electronic structures of the electron transfer series $[M(bpy)_3]^n$, $[M(tpy)_2]^n$, and $[Fe(t\text{-}bpy)_3]^n$ (M = Fe, Ru; n = 3+, 2+, 1+, 0, 1-): a mössbauer spectroscopic and DFT study, Eur. J. Inorg. Chem. 2012 (2012) 4605–4621.

[28] J. Mun, M. Lee, J. Park, D. Oh, D. Lee, S. Doo, Non-aqueous redox flow batteries with nickel and iron tris (2, 2′-bipyridine) complex electrolyte, Electrochem. Solid-State Lett. 15 (2012) A80–A82.

[29] R.M. Darling, K.G. Gallagher, J.A. Kowalski, S. Ha, F.R. Brushett, Pathways to low-cost electrochemical energy storage: a comparison of aqueous and nonaqueous flow batteries, Energy Environ. Sci. 7 (2014) 3459–3477.

[30] B. Hwang, M.S. Park, K. Kim, Ferrocene and cobaltocene derivatives for non-aqueous redox flow batteries, ChemSusChem. 8 (2015) 310–314.

[31] N.S. Hudak, L.J. Small, H.D. Pratt, T.M. Anderson, Through-plane conductivities of membranes for nonaqueous redox flow batteries, J. Electrochem. Soc. 162 (2015) A2188–A2194.

[32] I. Escalante-Garcia, J.S. Wainright, L.T. Thompson, R.F. Savinell, Performance of a non-aqueous vanadium acetylacetonate prototype redox flow battery: Examination of separators and capacity decay, J. Electrochem. Soc. 162 (2015) A363–A372.

[33] X. Wei, W. Xu, M. Vijayakumar, L. Cosimbescu, T. Liu, V. Sprenkle, W. Wang, TEMPO-based catholyte for high-energy density nonaqueous redox flow batteries, Adv. Mater. 26 (2014) 7649–7653.

[34] M. Park, N. Lee, S. Lee, K.J. Kim, D. Oh, Y. Kim, High-energy redox-flow batteries with hybrid metal foam electrodes, ACS Appl. Mater. Interfaces. 6 (2014) 10729–10735.

[35] S.H. Oh, C.W. Lee, D.H. Chun, J.D. Jeon, J. Shim, K.H. Shin, J.H. Yang, A metal-free and all-organic redox flow battery with polythiophene as the electroactive species, J. Mater. Chem. A. 2 (2014) 19994–19998.

[36] Y. Ding, Y. Zhao, Y. Li, J.B. Goodenough, G. Yu, A high-performance all-metallocene-based, non-aqueous redox flow battery, Energy Environ. Sci. 10 (2017) 491–497.

[37] J. Kucharyson, Structure-function relationships of metal coordination complexes for non-aqueous redox flow batteries, University of Michigan, 2017.

[38] N.M. Shavaleev, F. Kessler, M. Grätzel, M.K. Nazeeruddin, Redox properties of cobalt (II) complexes with azole-pyridines, Inorganica Chim. Acta. 407 (2013) 261–268.

Chapter 6

Design of a Supporting Salt Free, Common Ion Exchange Non-aqueous Redox Flow Battery

6.1 Background and Approach

Despite the myriad advantages RFBs offer for energy storage devices, high system prices (>\$500 kWh^{-1} in 2014) [1,2] have severely limited their commercial deployment. To facilitate integration of a 4 h energy storage system, the United States Department of Energy Office of Electricity Delivery and Energy Reliability set a target price of \$150 kWh^{-1}, including installation and power-conditioning equipment costs. [3,4] Recent techno-economic analyses predicted that NAqRFBs could reach this aggressive target by decreasing manufacturing costs, advancing materials performance, and improving cell architecture. [1,5] In conjunction with these strategies, it will also be necessary to develop new design concepts to further drive down costs.

Future-state prices for NAq supporting electrolytes (solvent + 1 M salt) are anticipated to be relatively high (~\$5 kg^{-1}), as compared to their aqueous counterparts (~\$0.10 kg^{-1}), [1] so decreasing the costs and / or quantities of both the solvent and supporting salt will be critical. [5] A number of studies have focused on enhancing active species solubility, [6–11] which serves to decrease the total amount of solvent required. [5] The supporting salt, however, especially the

fluorinated derivatives typically employed in NAq systems (e.g., lithium hexafluorophosphate, tetrabutylammonium tetrafluoroborate), will constitute a majority of the future-state supporting electrolyte cost (~\$20 kg^{-1} vs. ~\$2 kg^{-1} for the salt and solvent, respectively). [1] Despite the opportunity for substantial cost savings, [5,12] few studies have focused on minimizing supporting salt content.

NAqRFBs utilize supporting salts to enhance electrolyte conductivity and maintain electroneutrality during charge and discharge. [13,14] In addition to increasing costs, high salt concentrations limit the solubility of the active species in the electrolyte solution [12,15,16] and suppress the conductivity of ion-selective membranes, increasing area-specific resistance (ASR). [17] In this chapter I will introduce the concept of common ion exchange NAqRFBs as a strategy for minimizing supporting salt content.

There are a few different NAqRFB configurations that can be conceptualized. A salt splitting configuration is illustrated schematically in Figure 6.1a. Note that to maintain bulk electroneutrality during charging, supporting salt anions migrate to the positive electrolyte (catholyte), and supporting salt cations migrate to the negative electrolyte (anolyte). For this configuration, the electrolyte must dissolve enough supporting salt to maintain bulk electroneutrality in the presence of the charged active species, requiring at minimum a n:1 ratio of supporting salt to active material, where n is the number of electrons transferred. The supporting salt ions are therefore critical reactants in the redox processes and could limit RFB capacity. A more economically viable configuration is the common ion exchange NAqRFB, where both active species have charges of the same sign, either positive or negative, and as a result, only a single ion of the supporting salt migrates across the separator as a charge carrier (Figure 6.1b). In this system, charge balance can be achieved even in the complete absence of

supporting salt, with the salt serving only to increase electrolyte conductivity. The same concept can be extended to redox-active anions with counter-cations.

The need for supporting salt can be eliminated entirely by using similarly charged active species (positive or negative) that remain as ions across all accessible states-of-charge (SOCs). In this scheme, counter-ions that are associated with the redox-active ion provide charge balance, and both the active species and counter-ions contribute to the ionic conductivity of the electrolyte. Figure 6.1c highlights the charging process for a NAqRFB utilizing cationic active species with no supporting salt, where counter-anions transport from the anolyte to the catholyte, maintaining conductivity and electroneutrality.

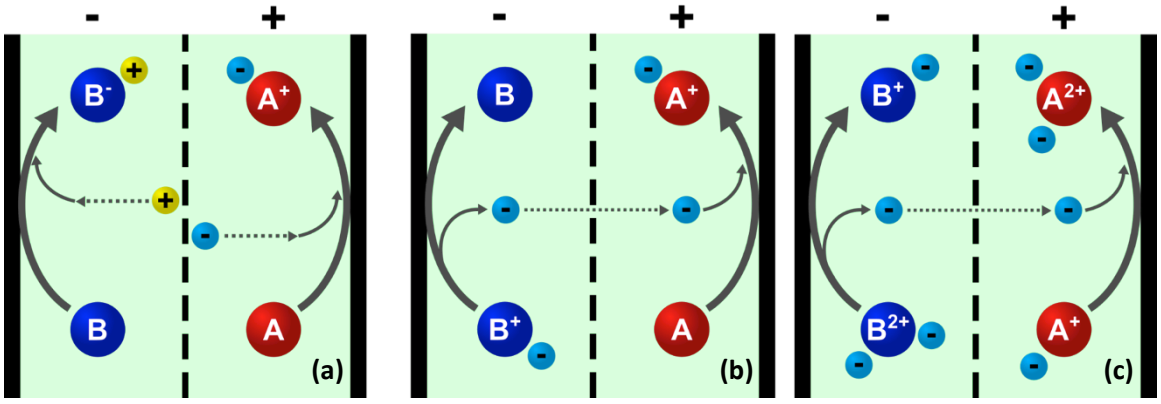

Figure 6.1 Schematic comparison of the charging processes in **(a)** a salt splitting RFB, **(b)** a common anion exchange RFB and **(c)** a common anion exchange, supporting salt free RFB. A is the catholyte active material (red), and B is the anolyte active material (dark blue). Supporting salt cations are denoted by "+" (yellow), and supporting salt anions are denoted by "-" (light blue).

To date, many reported NAqRFBs employ a salt splitting configuration. [18–21] A notable example is the vanadium acetylacetonate ($V(acac)_3$) NAqRFB, where, upon charging, an anion is formed in the anolyte ($V(acac)_3^-$), while a cation is generated in the catholyte ($V(acac)_3^+$). [15] Some studies report the use of common ion exchange for NAqRFBs, but do not contemplate the cost and performance benefits of employing this configuration. The majority of these prior

reports describe symmetric common anion exchange systems utilizing tris-bipyridine metal coordination complexes, including chromium, iron, and ruthenium tris-bipyridines. [9,22,23] A few asymmetric anion exchange systems utilized two tris-bipyridine complexes with different metal centers. [24–26] A vanadium dithiolate complex was the focus of the only symmetric common cation exchange system. [27]

In this chapter I will discuss the design and demonstration of a common ion exchange NAqRFB configured to operate in the absence of any supporting salt. A number of criteria are established to select model active species for this demonstration cell and based on these requirements iron (II) tris(2,2'-bipyridine) tetrafluoroborate ($Fe(bpy)_3(BF_4)_2$) and ferrocenylmethyl dimethyl ethyl ammonium tetrafluoroborate ($Fc1N112\text{-}BF_4$) are selected as the anolyte and catholyte, respectively. First, conductivity measurements are performed to demonstrate the high conductivities of the model ionic active species in acetonitrile (MeCN). Second, cyclic voltammetry (CV) and bulk electrolysis experiments indicate that the ionic active species maintain redox activity in the absence of supporting salt. Third, proof-of-concept flow cell experiments demonstrate the feasibility of a supporting salt free NAqRFB, exhibiting resistances and efficiencies similar to those of other recently reported NAqRFBs. Finally, a chemistry-agnostic techno-economic analysis highlights the cost savings afforded by minimizing or eliminating the amount of salt in NAqRFBs with varying active species costs, salt costs, and cell potentials. Overall, this work highlights the benefits of common ion exchange NAqRFBs, which enable higher active species concentrations, increasing electrolyte energy density, and minimizing the use of expensive NAq solvents and supporting salts. Further, the design principles outlined in this work can be extended beyond these model compounds to other active

species as they are developed, including organic molecules, providing a viable route to minimizing the cost of promising future NAqRFBs.

6.2 Experimental

6.2.1 Materials and Methods

All solution preparation and electrochemical experiments were performed inside argon filled glove boxes (O_2 < 5 ppm, H_2O < 1 ppm). MeCN (Extra Dry, 99.9%) was purchased from Acros Organics. Tetraethylammonium tetrafluoroborate (99.9%) and lithium tetrafluoroborate (99.9%) were purchased from BASF and used as received.

6.2.2 Active Species Synthesis

All reagents and starting materials (iron(II) tetrafluoroborate hexahydrate (97%), (dimethylaminomethyl)ferrocene (96%), bromoethane (98%), sodium tetrafluoroborate (98%)) were purchased from Sigma-Aldrich, with the exception of 2,2'-bipyridine (98%, Alfa Aesar), and used as received. $Fe(bpy)_3(BF_4)_2$ was prepared according to a literature procedure. [28] Fc1N112-BF_4 was synthesized through a bromide salt intermediate also as reported in literature. [7,8] Ion exchange of Br^- with BF_4^- was performed in deionized water to afford the final product.

6.2.3 Solubility Measurements

Active material solubility measurements were performed using a UV-Vis method [10] in both pure solvent and in the presence of supporting salt. First, stock solutions of $Fe(bpy)_3(BF_4)_2$ or Fc1N112-BF_4 were prepared at known concentrations in MeCN. Five-point calibration curves of characteristic absorbance peaks as a function of active species concentration were established.

The individual active species were added in excess to pure MeCN or 0.5 M $TBABF_4$/MeCN to generate solutions saturated with the active material. The saturated solutions were centrifuged at 6000 rpm for 5 min. The supernatant was diluted with MeCN or 0.5 M $TBABF_4$/MeCN to within the range of the absorption calibration curve, and the absorption of the diluted solution was measured using UV-Vis. Given the difficulty of measuring solubility in ternary electrolytes, it was assumed that $TBABF_4$ did not precipitate out of solution due to the high solubility limit of $TBABF_4$ in MeCN (> 3 M). [29]

6.2.4 Conductivity Measurements

Electrolyte conductivity measurements were collected using a two electrode, Swagelok style conductivity cell that has been described previously in literature. [30] The cell was calibrated in an ice water bath (0 $^{\circ}$C) to build a 4-point calibration curve using the following aqueous sodium chloride standards (Orion^{TM}): 0.100, 1.413, 12.90, and 111.9 mS cm^{-1}. For the NAq electrolyte conductivity measurements the cell was filled with electrolyte (600 μL) and then sealed. The impedance of the conductivity cell was measured over a small frequency range (1 MHz to 100 Hz) about the OCV with a voltage amplitude of 10 mV. The high frequency intercept of the Nyquist plot was used as the cell resistance value for subsequent calculations of electrolyte conductivity. Cell resistances were measured 10 times for 3 aliquots of each electrolyte composition. NAq electrolyte conductivities were determined from cell resistance measurements and the calibration curve.

6.2.5 *Cyclic Voltammetry*

A 3 mm diameter glassy carbon disk was used as the working electrode (BASi), a coiled platinum wire as the counter electrode, and a fritted Ag/Ag^+ quasi-reference electrode (BASi) filled with silver tetrafluoroborate (0.01 M, 98%, Sigma Aldrich) in MeCN. CVs were recorded at a scan rate of 100 mV s^{-1} in MeCN solutions containing the individual active species (5 mM) or an equimolar mixture containing both $Fe(bpy)_3(BF_4)_2$ and Fc1N112-BF_4 (10 mM total). CVs were *iR* corrected using the ohmic resistance of the cell measured using electrochemical impendence spectroscopy. Impedance measurements recorded about OCV over a frequency range of 1 MHz to 1 Hz with a potential amplitude of 10 mV.

6.2.6 *Bulk Electrolysis*

Details on the cell can be found in Section 2.2.4. A BioLogic VSP potentiostat was used to apply a constant current equivalent to a C-rate of 1C (0.67 mA). Potential cutoffs (0.55, 0 V and -1.7, -1.2 V for the positive and negative experiments, respectively) and a 100% SOC coulombic cutoff were used during cycling. A 3 mm diameter glassy carbon working electrode (BASi) was used to record CVs before and during cycling. For each test, both active species (10 mM total) were dissolved in MeCN.

6.2.7 *Flow Cells*

The flow cell used in this study is similar to previous literature reports [11,30] and additional details can be found in Section 4.2.1. Electrodes were cut from 190 ± 30 μm thick carbon paper (25 AA, SGL Group) and used as received. Carbon paper electrodes were layered two pieces thick and compressed by 20 ± 2% in the assembled flow cell. A single layer of

Daramic 175 was used as received as the cell separator. Teflon gaskets sealed the separator and electrodes inside the cell. Pre-mixed electrolyte (10 mL), containing $Fe(bpy)_3(BF_4)_2$ (0.2 M) / Fc1N112-BF_4 (0.2 M) / MeCN, was pumped into each flow cell reservoir using a peristaltic pump. During the first flow cell cycling experiment, a constant current density of 20 mA cm^{-2} (51 mA) was applied, and cell potential cutoffs of 1.00 – 1.97 V were imposed. The cell was cycled 10 times over ~5.3 h. Flow cell impedance measurements before and after the first flow cell experiment were recorded about OCV over a frequency range of 100 kHz to 5 mHz, with a potential amplitude of 10 mV. A second flow cell cycling experiment was performed in which constant current cycling (20 mA cm^{-2}) was paused at each half cycle to measure flow cell impedance in a higher frequency regime (100 kHz to 20 Hz).

6.3 Results and Discussion

6.3.1 Active Species Selection

For this study it was necessary to select model active species to demonstrate the salt free cell concept. Ideal materials need to be soluble and stable in the same solvent at all relevant oxidation states, commercially available or easy to synthesize in large quantities, and most importantly remain as ions at all accessed charge states. The lack of viable NAqRFB chemistries, especially those with the characteristics necessary for the demonstration of a salt free device, drove our selections. Fc1N112-BF_4 is known to be a highly soluble and stable catholyte active material, [7,8,12] however, it is too expensive for implementation in a low cost grid-scale device. [5] $Fe(bpy)_3(BF_4)_2$ is one of the only well-characterized NAqRFB anolyte active materials that remains as a cation across all relevant SOCs, but suffers from relatively poor stability. [12,23] Both species have been investigated extensively in prior literature and have well-characterized

properties. For these reasons we selected iron (II) tris(2,2'-bipyridine) tetrafluoroborate ($Fe(bpy)_3(BF_4)_2$) [23] and ferrocenylmethyl dimethyl ethyl ammonium tetrafluoroborate ($Fc1N112\text{-}BF_4$) [7,8] as the anolyte and catholyte model ionic redox active species, respectively.

In this system, $Fe(bpy)_3^{2+}$ and $Fc1N112^+$ act as the redox-active cations (at 0% SOC), while BF_4^- serves as the common, charge balancing, counter-anion. The catholyte and anolyte half-cell reactions are provided in Equations (1) and (2), respectively, while Equation (3) shows the full-cell reaction:

$$[Fc1N112^{2+}][BF_4^-]_2 + e^- \Leftrightarrow [Fc1N112^+][BF_4^-] + BF_4^- \quad (1)$$

$$[Fe(bpy)_3^{2+}][BF_4^-]_2 + e^- \Leftrightarrow [Fe(bpy)_3^+][BF_4^-] + BF_4^- \quad (2)$$

$$[Fe(bpy)_3^{2+}][BF_4^-]_2 + [Fc1N112^+][BF_4^-] \Leftrightarrow [Fe(bpy)_3^+][BF_4^-] + [Fc1N112^{2+}][BF_4^-]_2 \quad (3)$$

Importantly, these active species are positively charged at all relevant oxidation states, enabling the salt free cell configuration outlined in Figure 6.1c. Additionally, these species exhibit minimal inter-species reactions in the singly charged state (see Chapter 5 for additional details), are soluble in MeCN, and are easily synthesized in large quantities, facilitating a proof-of-concept flow cell enlisting the no supporting salt concept. [12]

6.3.2 Active Species Solubility

As previously mentioned, a key advantage associated with common ion exchange NAqRFBs is the ability to minimize the quantity of supporting salt required for RFB operation. Minimizing the salt content enables reduced solvent costs and higher active materials concentrations, which can subsequently decrease concentration (mass transport) and activation (kinetic) polarization losses. [31] Shinkle et al. reported that the solubility of $V(acac)_3$ in MeCN decreased monotonically with increased concentration of tetraethylammonium tetrafluoroborate

in the ternary electrolyte. [15] To quantify the dual-solute effects for the $Fe(bpy)_3(BF_4)_2$/Fc1N112-BF_4 chemistries, a UV-Vis absorbance study demonstrates the effect of supporting salt concentration on active material solubility. This methodology does not map the entire chemical space, but does demonstrate the utility of minimizing supporting salt content to maximize active species solubility. Fc1N112-BF_4/$TBABF_4$/MeCN and $Fe(bpy)_3(BF_4)_2$/$TBABF_4$/MeCN are the ternary electrolytes of interest. Table 6.1 displays the solubilities of $Fe(bpy)_3(BF_4)_2$ and Fc1N112-BF_4 in MeCN with either 0 M or ~0.5 M supporting salt. The solubilities of both active materials decrease significantly (50% for $Fe(bpy)_3(BF_4)_2$ and 27% for Fc1N112-BF_4) with ~0.5 M $TBABF_4$ in solution. For application in a commercial asymmetric RFB system, identifying the active material solubilities in the quaternary $Fe(bpy)_3(BF_4)_2$/Fc1N112-BF_4/$TBABF_4$/MeCN mixed electrolyte system would be crucial to avoid active material precipitation. Nonetheless, this preliminary solubility study demonstrates that by implementing a common ion exchange NAqRFB configuration, the concentration of supporting salt can vary independently from the active material concentration to optimize active material solubility and electrolyte conductivity.

Table 6.1 Active species solubilities with and without supporting salt in MeCN.

Active Material	**$TBABF_4$ Concentration (M)**	**Active Species Solubility (M)**
$Fe(bpy)_3(BF_4)_2$	0	0.6
$Fe(bpy)_3(BF_4)_2$	0.5	0.3
Fc1N112-BF_4	0	1.9
Fc1N112-BF_4	0.5	1.4

Darling et al. suggested that for NAqRFBs to achieve a \$150 kWh^{-1} system price, including installation and invertor costs, the solubility per accessed electron must be 4 – 5 M. [5]

For a $1e^-$ transfer NAqRFB, this requirement implies a minimum solubility of 4 – 5 M. Since the electrolyte would require an additional 4 – 5 M supporting salt, the total concentration of active species and supporting salt would be 8 – 10 M. Most nonaqueous solvents (e.g. MeCN, propylene carbonate, dimethoxyethane) cannot achieve such high solute concentrations without significantly increasing temperature or employing ionic liquid solvents. Ionic liquids would afford charge balance, but can cost 5-20 times more than molecular solvents. [32] For near term NAqRFB prototypes, a common ion configuration will enable low cost electrolytes and energy dense batteries.

6.3.3 Active Species Conductivity

To demonstrate the feasibility of performing electrochemical experiments in the complete absence of supporting salt, the conductivities of the active species are measured and compared to those of supporting salts typically employed in NAqRFBs. Figure 6.2 illustrates the high conductivities afforded by 0.2 M of the ionic active species in MeCN, especially in comparison to 0.2 M lithium tetrafluoroborate ($LiBF_4$) and tetraethylammonium tetrafluoroborate ($TEABF_4$) in the same solvent. Not shown in this figure is the conductivity of an equimolar solution containing 0.2 M Fc1N112-BF_4 / 0.2 M $Fe(bpy)_3(BF_4)_2$ / MeCN (0.4 M total active species), the electrolyte composition employed later in flow cell experiments, which is 22.5 mS cm^{-1}.

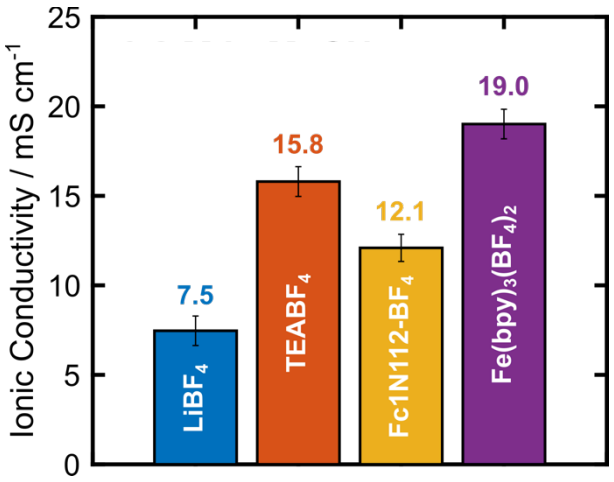

Figure 6.2 Comparison of electrolyte ionic conductivities for solutions containing 0.2 M of $LiBF_4$, $TEABF_4$, Fc1N112-BF_4, or $Fe(bpy)_3(BF_4)_2$ in MeCN. Error bars represent 95% confidence intervals of the standard error.

The conductivities of the ionic species increase in the following order: $LiBF_4$ < Fc1N112-BF_4 < $TEABF_4$ < $Fe(bpy)_3(BF_4)_2$. $LiBF_4$ likely exhibits the lowest conductivity because Li^+ is a hard acid, and will therefore interact strongly with BF_4^-, a hard base. This interaction leads to a low degree of dissociation and subsequently lower ionic strength in solution for the Li^+ cation salt compared to the larger and more polarizable TEA^+, $Fc1N112^+$, and $Fe(bpy)_3^{2+}$ cations. [33] $Fe(bpy)_3(BF_4)_2$ exhibits an enhanced conductivity relative to the other salts considered because $Fe(bpy)_3^{2+}$ is a divalent cation, leading to a higher ionic strength of the $Fe(bpy)_3(BF_4)_2$ solution as compared to the monovalent cation salts. Since the conductivities of the model ionic active species (Fc1N112-BF_4 and $Fe(bpy)_3(BF_4)_2$) are on the same order of magnitude as $TEABF_4$, a typical supporting salt for NAqRFBs, [13,34] they lend themselves to implementation in electrochemical systems without supporting salt.

6.3.4 Cyclic Voltammetry

Cyclic voltammetry is used to determine if the redox activity of the active species is maintained in the absence of supporting salt, while further validating that the electrolytes exhibit sufficient ionic conductivity to perform electrochemical measurements. Figure 6.3 displays CVs of solutions containing the individual active species and an equimolar mixture of each in MeCN, all without supporting salt. In a potential window relevant for a 1 e^- demonstration cell (Figure 6.3a), the electrochemical behavior remains similar to that of solutions containing supporting salt. When this window is expanded to include all the negative couples of $Fe(bpy)_3(BF_4)_2$ (Figure 6.3b), however, irreversible behavior is observed at negative potentials. This is due to the absence of charge balancing cations in solution. At positive potentials and through a single negative couple, $Fe(bpy)_3(BF_4)_2$ and Fc1N112-BF_4 remain as cations, and charge balance is maintained with the BF_4^- anions in solution. Beyond this redox event, though, $Fe(bpy)_3(BF_4)_2$ becomes neutral ($Fe(bpy)_3$) or negatively charged ($Fe(bpy)_3^-$). Since there are no supporting salt cations in solution to stabilize these anions, this leads to significant interactions between these species and positively charged $Fe(bpy)_3(BF_4)_2$, resulting in the observed irreversible behavior. This provides a nice demonstration on the importance of maintaining electroneutrality during cycling. Further, this behavior was expected and motivates the demonstration of only a one-electron cell utilizing these chemistries in the absence of supporting salt.

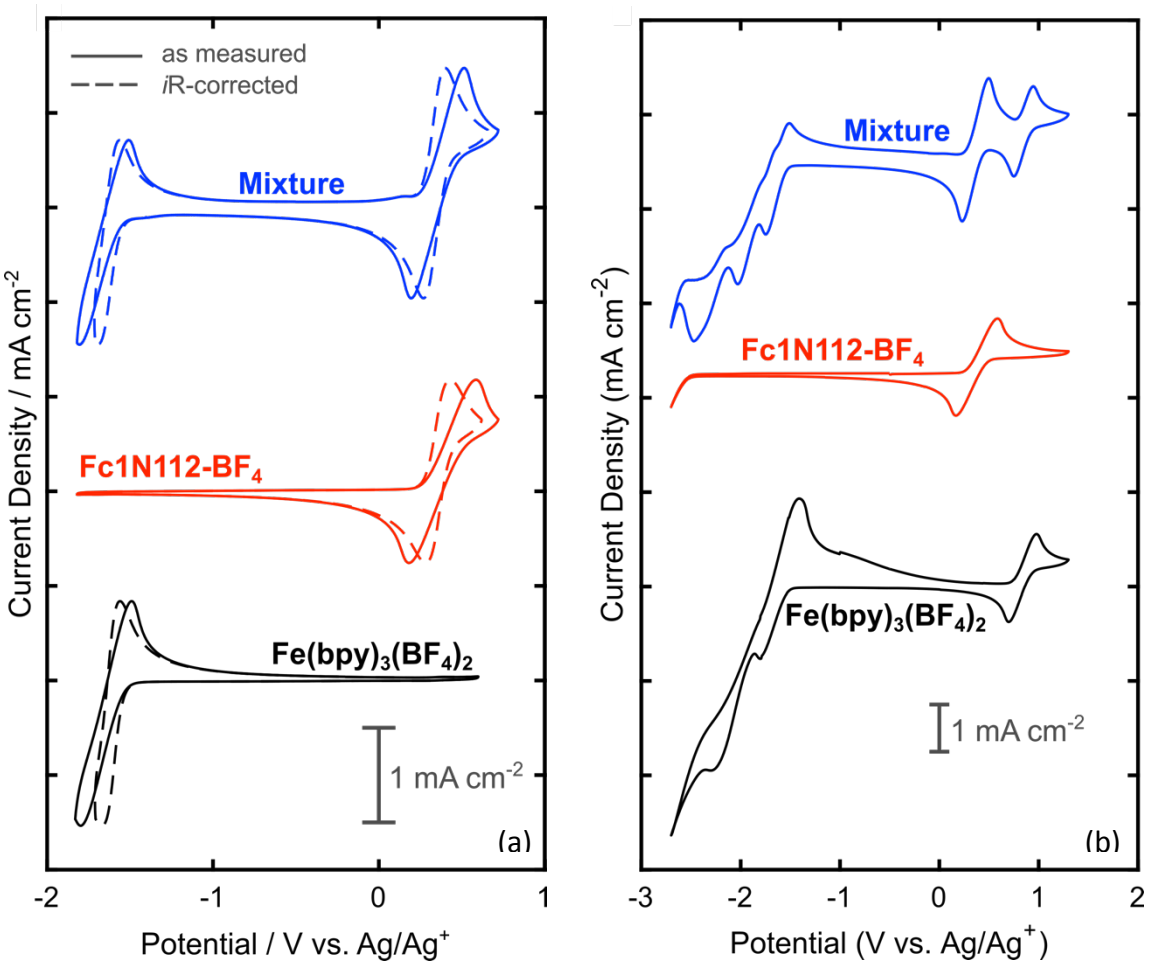

Figure 6.3 Cyclic voltammograms of 5 mM $Fe(bpy)_3(BF_4)_2$, Fc1N112-BF_4, and an equimolar mixture of each (10 mM total) in MeCN with no supporting salt for the window **(a)** used during cycling and **(b)** that includes all the couples of $Fe(bpy)_3(BF_4)_2$. Solid lines show the data as measured and the dashed lines represent *i*R-compensated CVs.

An analysis of the redox potentials and peak height ratios in Figure 6.3a reveal that they are similar to those of solutions at the same concentration in the presence of supporting salt (Table 6.2). [7,8,12,23] Notably, the redox potential of Fc1N112-BF_4 is ~70 mV greater than previously reported in a supporting electrolyte of 0.5 M $TBABF_4$ / MeCN. This discrepancy is reconciled when considering that BF_4^- appears in the Nernst equation, resulting in an increase in the equilibrium potential as the supporting salt is removed.

Table 6.2 Comparative CV analysis of electrolytes containing no supporting salt as measured and with *i*R correction, and electrolytes with a supporting salt concentration of 0.5 M $TBABF_4$ (from [12]). In all cases, the active species concentration is 5 mM.

	5 mM Fc1N112-BF_4			**5 mM $Fe(bpy)_3(BF_4)_2$**		
	Potential [V vs. Ag/Ag^+]	Peak Height Ratios	Peak Separation [mV]	Potential [V vs. Ag/Ag^+]	Peak Height Ratios	Peak Separation [mV]
No Salt (as measured)	0.35	1.0	405	-1.65	0.9	310
No Salt (*i*R-corrected)	0.36	1.0	147	-1.62	0.9	96
0.5 M $TBABF_4$ [12]	0.28	1.0	81	-1.65	0.9	66

Further analysis of the peak potentials reveals large peak-to-peak separations (Table 6.2) in the absence of supporting salt, as is anticipated due to the lower solution conductivity with only 5 mM active species in MeCN. [35] To confirm that this large peak-to-peak separation is primarily a result of low solution conductivity and not sluggish reaction kinetics, the CVs were *i*R-corrected (see dashed lines in Figure 6.3a). The uncompensated solution resistance is measured via electrochemical impedance spectroscopy. The *i*R-corrected CVs exhibit significantly smaller peak-to-peak separation values, but are still larger than those for a solution containing 0.5 M tetrabutylammonium tetrafluoroborate [12] ($TBABF_4$) (Table 6.2). This indicates that the electrokinetics are slightly slower in the regime of low ion concentration, perhaps due to the limited availability of anions. This interpretation is further supported by the decreased peak separation observed with the addition of more active species (i.e., single species vs. the equimolar mixture). These slight differences are expected to have a negligible impact during bulk cycling, especially at the high concentrations used in the flow cell experiments. Overall, these results demonstrate that a supporting salt free, one-electron flow cell utilizing

Fc1N112-BF_4 and $Fe(bpy)_3(BF_4)_2$ is feasible and should exhibit similar electrochemical behavior to that of a cell containing a high concentration (≥ 0.5 M) of supporting salt. [12]

6.3.5 Bulk Electrolysis

Bulk electrolysis experiments are used to determine if a cell containing a mixture of $Fe(bpy)_3(BF_4)_2$ and Fc1N112-BF_4 in MeCN (without supporting salt) will access the desired redox couples during cycling. Figure 6.4 displays capacity retention plots and potential curves for cells cycling through either a single positive or a single negative electron transfer event. In both cases the plateaus observed during cycling are at the potentials expected based on CV (Figure 6.3) and demonstrate that only the desired redox couples are accessed. Furthermore, the results are consistent with those reported in Chapter 5. [12]

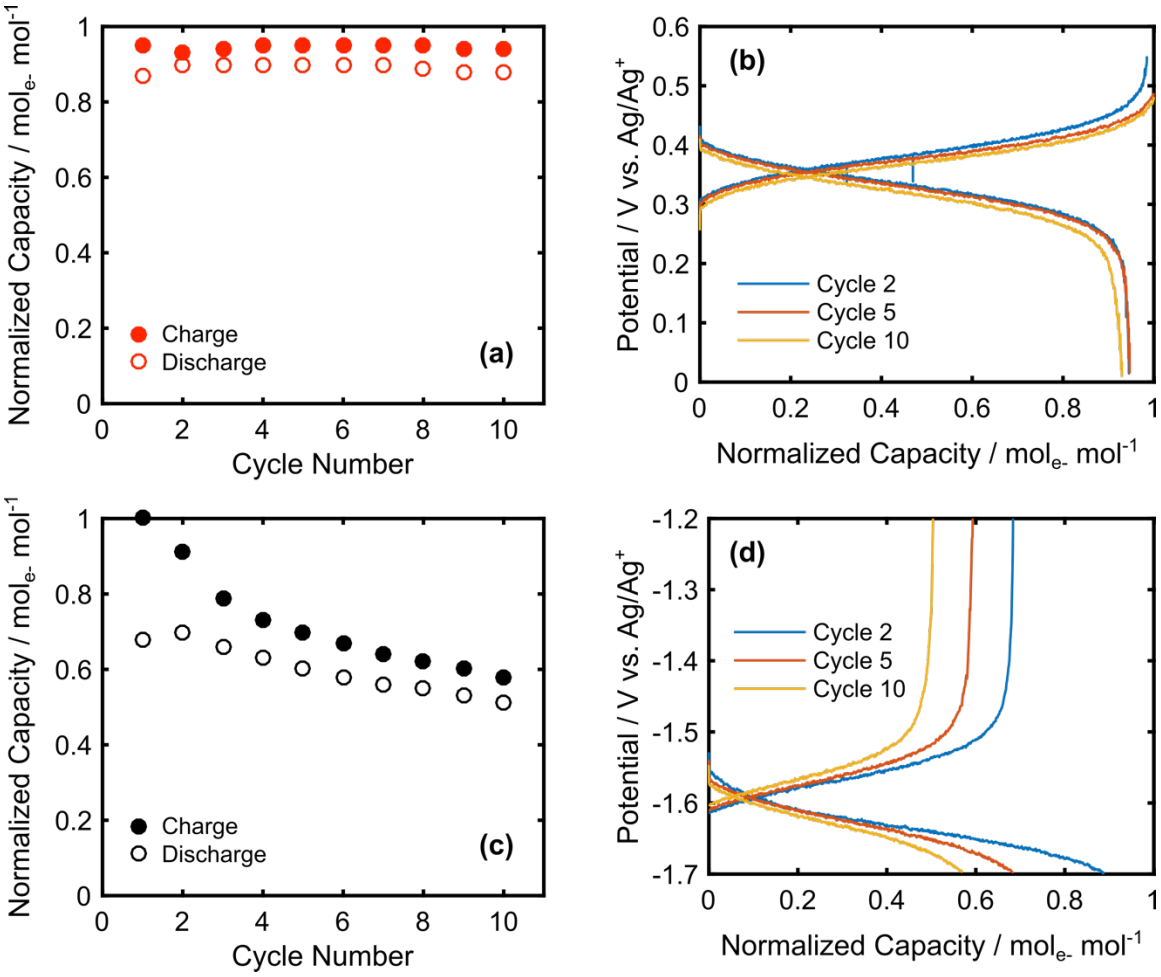

Figure 6.4 Bulk electrolysis of equimolar mixtures (5 mM each) of $Fe(bpy)_3(BF_4)_2$ and Fc1N112-BF_4 in the absence of supporting salt. **(a)** Capacity retention of the mixture, normalized to the theoretical capacity and **(b)** representative charge / discharge curves through a single positive electron transfer. **(c)** Capacity retention and **(d)** charge / discharge curves through a single negative electron transfer.

Fc1N112-BF_4 exhibits no detectable capacity fade over the 10 cycles (Figure 6.4a), which is in agreement with prior reports. [8,12] CVs before and after the bulk electrolysis experiment (Figure 6.5a) show little to no evidence of degradation at positive potentials. Conversely, $Fe(bpy)_3(BF_4)_2$ exhibits fairly rapid capacity decay over the course of the experiment due to the instability of the negative couple. [12] CVs indicate that peak heights associated with the $Fe(bpy)_3^{2+}$ / $Fe(bpy)_3^{+}$ couple decrease after cycling, confirming active species degradation

(Figure 6.5b). Despite the poor capacity retention of $Fe(bpy)_3(BF_4)_2$, in both cases the bulk electrolysis cells access the redox couples of interest, confirming the feasibility of using these model active species in a proof-of-concept flow cell without supporting salt.

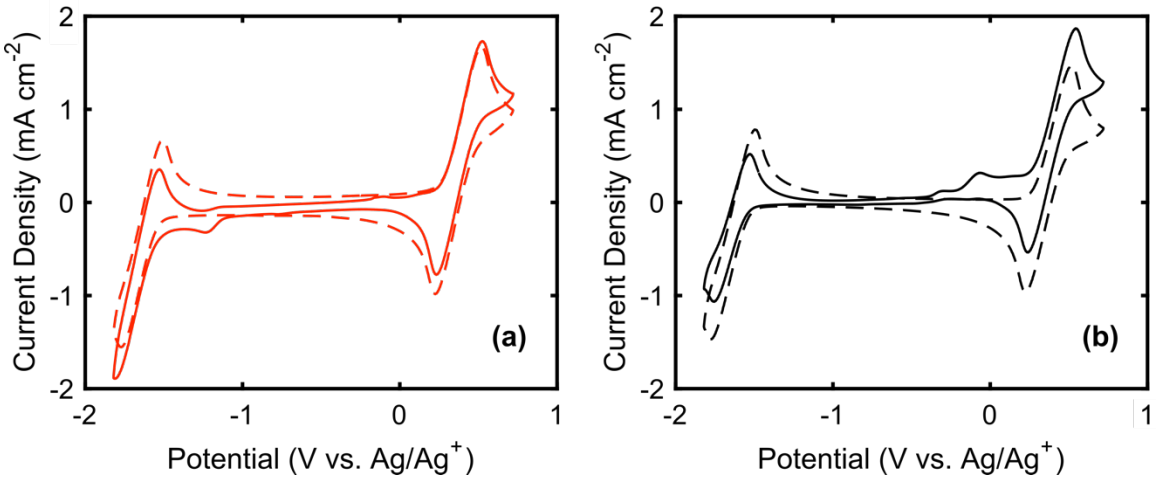

Figure 6.5 CVs before (dashed) and after (solid) 10 cycles in a bulk electrolysis cell for an equimolar mixture (10 mM total) of $Fe(bpy)_3(BF_4)_2$ and Fc1N112-BF_4, through a single **(a)** positive and **(b)** negative electron transfer. CVs are not *i*R-corrected.

6.3.6 Proof-of-Concept Flow Cell

The conductivities and fundamental electrochemical properties of the electrolyte encouraged demonstration of a proof-of-concept, supporting salt free NAqRFB, employing $Fe(bpy)_3(BF_4)_2$ and Fc1N112-BF_4 as model ionic active species. The flow cell has a similar architecture to a high performance all-vanadium flow cell, [36] modified for chemical compatibility with NAq electrolytes. [11,30] Since anion-exchange membranes exhibit limited stability in MeCN, [24,37] Daramic is selected for use as the separator due to its chemical stability in the electrolyte of interest, ensuring that separator degradation would not be a confounding factor in evaluating flow cell performance. Due to the high porosity (58%) and large characteristic pore sizes (~100 nm) for this separator, crossover is expected in these

experiments, so both reservoirs are filled with an equimolar mixture of 0.2 M $Fe(bpy)_3(BF_4)_2$ / 0.2 M Fc1N112-BF_4 / MeCN. Prior demonstration studies on RFBs have utilized pre-mixed electrolytes to mitigate effects of rapid crossover in the first few cycles, [12,38,39] however, mixed active species electrolytes will be too expensive to implement in grid-scale devices. [1,5] One additional drawback of this configuration is the limited operating concentration of each active species. Adding supporting salt can limit the solubility of active species, [12,15,16] and similar decreases are observed with the addition of other ionic active species. As a result, an active species concentration of 0.2 M ensures that the species remain soluble at all relevant SOCs.

The flow cell employs interdigitated flow fields (IDFFs) with carbon paper electrodes. Prior literature has suggested that IDFFs will offer the best performance for large-scale RFBs by balancing cell ASR and pressure drop. [36,40] Additionally, thin carbon paper electrodes offer a balance of high surface area, low ohmic losses, and facile mass transport. [11,41] Despite the relatively thick Daramic separator (175 μm), the cell exhibits an ohmic contribution (R_Ω) to the ASR of just 3.95 Ω cm^2 (Figure 6.6a) before cycling, a value similar to those reported in a prior flow cell study employing a Daramic separator and MeCN solvent. [34] Combining the IDFF with carbon paper electrodes alleviates mass transfer resistances at each electrode, [11] leading to a flow cell with a total ASR of 7.52 Ω cm^2, determined from an impedance measurement after cycling (Figure 6.6a, after). Increasing the active species concentration could further reduce mass transfer limitations, as well as improve ionic conductivity, subsequently decreasing the ohmic contribution to the ASR as well.

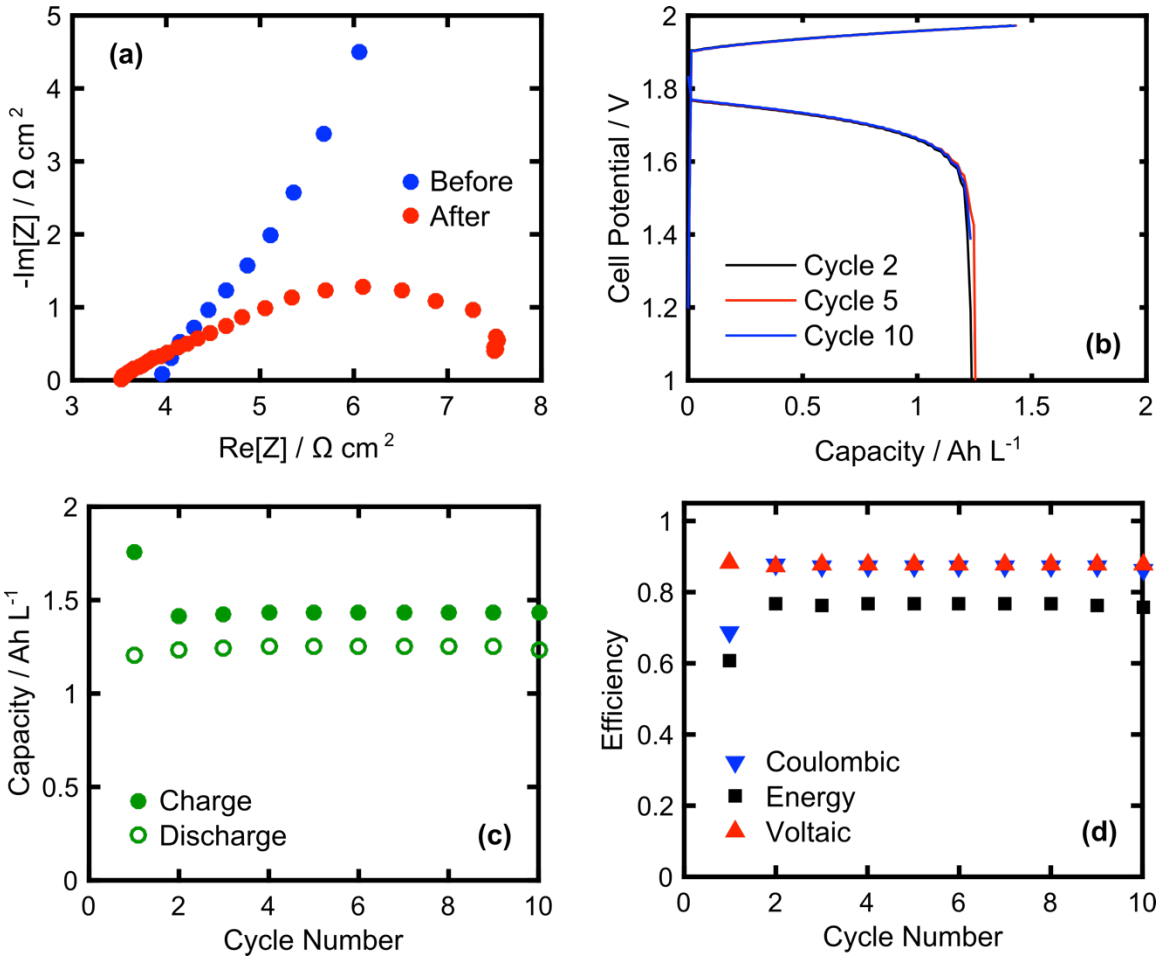

Figure 6.6 Cycling performance of a supporting salt free NAqRFB employing 0.2 M $Fe(bpy)_3(BF_4)_2$/0.2 M Fc1N112-BF_4/MeCN: **(a)** Nyquist plots before and after 10 cycles, **(b)** representative charge / discharge curves, **(c)** capacities, and **(d)** efficiencies. The theoretical capacity is 5.36 Ah L^{-1} (53.6 mAh), and 10 full cycles completed in ~5.3 h.

Further analysis of the impedance spectra reveals, prior to cycling, that the cell exhibits an unbounded, high overall impedance (Figure 6.6a, before). Since only the fully discharged active species ($Fe(bpy)_3^{2+}$ and $Fc1N112^{+}$) are present before cycling, the discharge reaction is heavily mass transfer limited and cannot proceed. After cycling, however, residual charged ($Fe(bpy)_3^{+}$ and $Fc1N112^{2+}$) and discharged species allow for the electrochemical reactions to proceed in either the forward or reverse directions, significantly improving the mass transfer

characteristics of the cell at open-circuit voltage (OCV). The bounded semicircle observed after cycling (Figure 6.6a, after), represents a diffusive mass transfer limitation through a boundary layer of finite thickness. [42] The low-frequency intercept, on the Nyquist plot exhibiting a bounded mass transfer element (Figure 6.6a, after), represents the total direct current (DC) cell resistance, at a particular SOC, and is typically a good measure of the flow cell ASR. [11,30,34,43]

The relatively low ASR in this study, as compared to those reported for other NAqRFBs, [25,34,38] allows for constant current cycling at a moderate current density of 20 mA cm^{-2}, which is among the highest reported for NAqRFBs. [44,45] Figure 6.6b presents cycling curves of the proof-of-concept supporting salt free NAqRFB, with single charge and discharge plateaus corresponding to the desired one-electron transfer processes and a nominal cell potential of ~1.9 V. To avoid accessing the additional, less stable redox couples of $Fe(bpy)_3(BF_4)_2$ (Figure 6.3b), [12,23] an upper cell potential cutoff of 1.97 V is employed. This cutoff limited the accessible capacity (Figure 6.6c) of the first cycle to 32.8% (1.76 Ah L^{-1}) of the theoretical capacity (5.36 Ah L^{-1}). We also limit cycling experiments to 10 cycles due to the known long term instability of $Fe(bpy)_3(BF_4)_2$. [12,23] After the first cycle, the coulombic, voltaic, and energy efficiencies are constant for the remaining 9 cycles, with mean values of 87.3 ± 0.1%, 87.5 ± 0.1%, 76.4 ± 0.1%, respectively (Figure 6.6d).

Notably, the capacity retention during flow cell cycling is higher than that observed during bulk electrolysis cycling for $Fe(bpy)_3(BF_4)_2$. This result is counterintuitive given the higher concentration of active species employed in the flow cell experiment (0.2 M) as compared to the bulk electrolysis experiment (5 mM) but can be reconciled when considering differences in the accessed capacity. The bulk electrolysis experiments access nearly 100% of the theoretical

capacities, as compared to < 33% for the flow cell experiment. Since a smaller fraction of the theoretical capacity is accessed in the flow cell experiment, deleterious side reactions associated with the less stable $Fe(bpy)_3(BF_4)_2$ species do not degrade the observed capacity as rapidly as in the bulk electrolysis experiment. This phenomena has been reported in prior literature for battery systems with low accessed capacities. [46,47] While the low accessed capacity in this demonstration flow cell is not useful for a grid scale device, the cycling results sufficiently illustrate a proof-of-concept flow cell operating with the design principle of utilizing redox active ions to completely remove the supporting salt.

This proof-of-concept flow cell displays cycling efficiencies similar to state-of-the-art NAqRFBs described in the literature [34,38], even without any supporting salt. Moderate current density and voltaic efficiencies are achieved because of the high separator conductivity and favorable mass transfer characteristics. The high separator conductivity is achieved by using a microporous separator, in which case the electrolyte conductivity defines the conductivity through the separator pores. Since Daramic is a passive separator, the migration of BF_4^- anions through the separator is sufficiently rapid to afford simultaneously charge balance and moderate currents across the range of accessed SOCs. Critically, the BF_4^- anions act as both charge carriers and charge balancing species in the relevant electrochemical reactions.

To highlight further the dual functionality of the BF_4^- anions, which are associated with the ionic redox active species, we perform a second flow cell cycling experiment where R_Ω is recorded at every half cycle. Figure 6.7 shows that R_Ω remains nearly constant, oscillating by ± 4.0% about a mean value of 3.48 Ω cm^2. The small oscillations in R_Ω between half cycles (inset Figure 6.7), are likely caused by variations in ion-pair association constants as a function of SOC, [30,48] subsequently changing the effective conductivity of the separator and porous electrodes.

Oscillations in electrolyte conductivity as a function of SOC are common during RFB cycling, as demonstrated for the all-vanadium RFB [48] and quantified in one NAqRFB electrolyte study. [30] Ultimately, the data in Figure 6.7 points to a cell devoid of supporting salt that maintains R_Ω values comparable to the contemporary literature. [34]

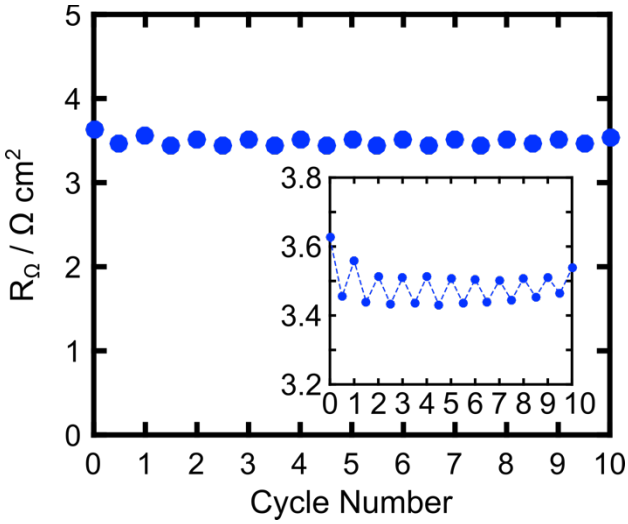

Figure 6.7 Ohmic contribution to cell ASR measured every half cycle for a supporting salt free NAqRFB. The electrolyte composition is 0.2 M $Fe(bpy)_3(BF_4)_2$ / 0.2 M Fc1N112-BF_4 / MeCN. Inset: Expansion in the R_Ω range of 3.2 – 3.8 Ω cm^2, where the dashed line serves as a visual guide. R_Ω is smaller in the cell's charged state.

6.3.7 Techno-economic Analysis of Salt Free NAqRFBs

To investigate the financial benefits of removing, or minimizing, the supporting salt requirement in NAqRFB electrolytes, we perform a chemistry-agnostic techno-economic analysis to quantify how salt cost and concentration affect battery price. Techno-economic analysis is a powerful tool for evaluating the price performance of an energy storage system by relating the total battery price to material properties, electrochemical performance, and component cost parameters. Given that the proof-of-concept flow cell does not have sufficiently stable or low cost active materials, as well as an insufficient cell potential, we develop a

chemistry-agnostic representation that illustrates the cost savings afforded by minimizing supporting salt concentration for a variety of active species costs, salt costs, and cell potentials.

6.3.7.1 Catholyte Costs

A techno-economic model is developed based on previous work by Darling et al. [1] to compare catholyte costs for a common ion configuration to that of a salt splitting cell. Equation 4 defines the chemical cost per total energy stored (C/E) in \$ kWh^{-1} based on contributions from the active species, solvent, and salt. Table 6.3 details all variable definitions. Due to uncertainties in active material cost $\left(c_m^{\$}\right)$, calculations considered a low (\$5 kg^{-1}) and high (\$20 kg^{-1}) value to illustrate changes in the model as a function of active material cost. A prior study suggested that tailored molecules could achieve an optimistic cost of \$5 kg^{-1}, [1] defining the lower bound for this analysis. In the particular case of the $Fe(bpy)_3(BF_4)_2$/Fc1N112-BF_4 chemistry, the active species resemble other tetrafluoroborate salts employed in lithium-ion batteries, so the upper bound active material cost for this analysis is \$20 kg^{-1}, a projected future state price of salts for lithium-ion batteries. [1] This description varies from Darling's model [1] in that the electrolyte cost is divided into its constituent salt and solvent costs. For simplicity, efficiencies, depth-of-discharge, and reaction stoichiometry equal unity.

$$\frac{C}{E} = \frac{1}{nFU}\left[M_m c_m^{\$} + r_{sol} M_{sol} c_{sol}^{\$} + r_{salt} M_{salt} c_{salt}^{\$}\right] \tag{4}$$

Table 6.3 Equation 4 variable definitions and units. Values of each variable used in the common ion versus salt splitting cost analysis are also provided.

Variable	Description	Unit	Common Ion	Salt Splitting
n	Number of Electrons	-	1	
F	Faraday Constant	kA·h mol^{-1}	0.026801	
U	Cell Potential	V	1.9	
M_m	Active Material Molecular Weight	kg mol^{-1}	0.359	
M_{sol}	Solvent Molecular Weight	kg mol^{-1}	0.041	
M_{salt}	Salt Molecular Weight	kg mol^{-1}	0.329	
r_{sol}	Solvent-to-Actives Molar Ratio	-	-	
r_{salt}	Salt-to-Actives Molar Ratio	-	0.5	1.5
$c_m^{\$}$	Active Material Cost	\$ kg^{-1}	5 [1] or 20	
$c_{sol}^{\$}$	Solvent Cost	\$ kg^{-1}	2 [1]	
$c_{salt}^{\$}$	Salt Cost	\$ kg^{-1}	20 [1]	

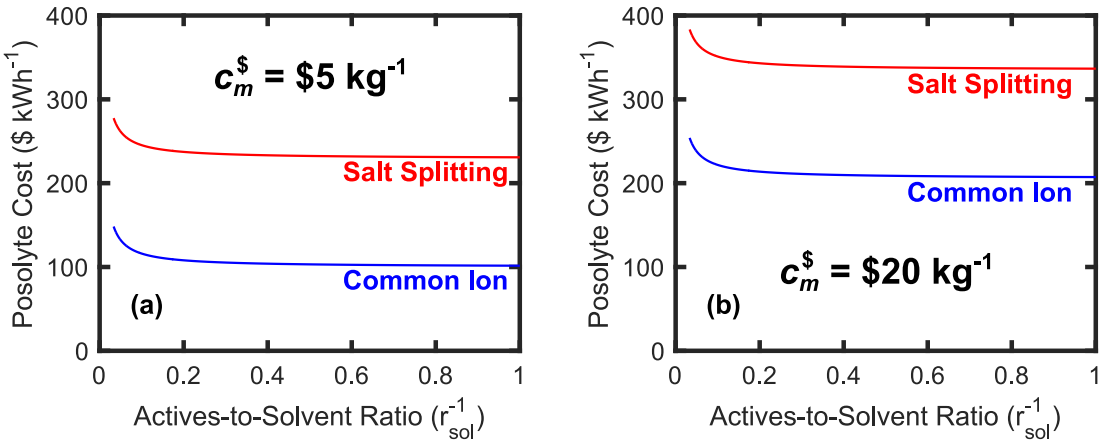

Figure 6.8 Catholyte costs for salt splitting and common ion exchange asymmetric NAqRFBs as a function of molar actives-to-solvent ratio $\left(r_{sol}^{-1}\right)$, where the active material cost $\left(c_m^{\$}\right)$is **(a)** \$5 kg^{-1} or **(b)** \$20 kg^{-1}. Fc1N112-BF_4 is the sole active material in an unmixed catholyte, and the anolyte active material has a redox potential of -1.65 V vs Ag/Ag^+ with $1e^-$ transfer. The common ion configuration is cheaper across all values of r_{sol}^{-1} due to the decreased salt cost.

Figure 6.8 plots the costs of catholytes in salt splitting and common ion configurations as a function of molar actives-to-solvent ratio $\left(r_{sol}^{-1}\right)$, clearly demonstrating the economic advantage of common ion exchange. Table 6.3 lists quantitative details for each variable in the cost analysis,

where Fc1N112-BF_4 (M_m = 0.359 kg mol^{-1}) is the sole catholyte redox active material (unmixed, asymmetric configuration), MeCN is the solvent (M_{sol} = 0.041 kg mol^{-1}), and $TBABF_4$ is the supporting salt (M_{salt} = 0.329 kg mol^{-1}). The anolyte active material has a redox potential of -1.65 V vs Ag/Ag^+, defining the cell potential, but the asymmetric catholyte cost does not account for the cost of the anolyte active material. As illustrated by Figure 6.8, the cost of both cell configurations decreases as a function of active species concentration, but the common ion cell is less expensive across *all* concentrations. These chemical cost savings are a result of the decreased salt requirement for common ion exchange NAqRFBs. While varying the active material cost linearly shifts the cost curves to higher and lower values, the cost difference in moving from a salt splitting to common ion configuration remains the same due to an identical savings (\$129 kWh^{-1} for this particular example) in total salt cost. As previously described, salt-splitting RFBs require a minimum n:1 molar ratio of salt-to-actives ($r_{salt} \geq n$) to maintain charge neutrality, while common ion exchange cells can charge balance at any supporting salt concentration ($r_{salt} \geq 0$). The techno-economic analysis uses r_{salt} values of 0.5 and 1.5 for the salt splitting and common ion NAqRFBs, respectively, representing a salt concentration 0.5 M above the minimum charge balancing salt requirement for each type of cell. In addition to increasing costs, experimental results in Section 6.3.2 show that increasing salt concentration in the electrolyte suppresses active species solubility. Active species with lower solubilities require a higher molar ratio of solvent-to-actives (r_{sol}) to dissolve completely all active species and salt in the electrolyte. Since NAqRFBs can have solvent costs $\left(c_{sol}^{\$}\right)$ on the same order of magnitude as the active species $\left(c_m^{\$}\right)$ costs, minimizing r_{sol} can significantly decrease chemical costs. The catholyte cost as a function of r_{sol} asymptotically approaches a value where the solvent cost

contribution is zero ($r_{sol} = 0$). Ultimately, common ion exchange cells decrease chemical costs by minimizing both r_{salt} and r_{sol}.

Note, however, that selecting a common ion exchange chemistry often requires active species with high(er) molecular weights. Common ion exchange RFBs must contain ionic active species at 0 % SOC. Functionalization of neutral redox active species can produce redox active ions, [7,8] which necessarily will increase the molecular weight of the active species and could also increase active material cost (higher $c_m^{\$}$) due to additional synthesis steps. Equation 5 defines a dimensionless cost ratio, γ, to determine whether to employ heavier, ionic active materials considering only the chemical cost. In Equation 5, the subscript *CI* denotes the heavier, common ion compatible active material and the subscript *SS* denotes the lighter, salt splitting active material. The cost ratio γ compares the cost increase (numerator) of employing a heavier active material to the cost savings (denominator) associated with the low salt concentration requirement and higher solubility of the common ion compatible active material. If $\gamma < 1$, the common ion exchange RFB is cheaper, whereas if $\gamma > 1$, the salt splitting RFB is more cost effective. Notably, as the number of electron transfers per molecule increases (higher n) the salt cost contribution increases linearly for the salt splitting configuration, making common ion exchange RFBs increasingly favorable for multi-electron transfer systems. In most practical examples, the common ion exchange system is cheaper, despite a higher active species molecular weight or cost. This cost analysis does not consider other advantages of ionic modification that can further decrease cost, such as increased redox potential (higher U). [8,49]

$$\gamma = \frac{\left(M_{m,CI}c_{m,CI}^{\$} - M_{m,\mathrm{SS}}c_{m,\mathrm{SS}}^{\$}\right)}{M_{sol}c_{sol}^{\$}\left(r_{sol,CI} - r_{sol,SS}\right) + nM_{salt}c_{salt}^{\$}} \tag{5}$$

6.3.7.2 Full Cell Costs

In addition to considering individual electrolyte cost savings, it is of interest to also estimate the total battery price savings that common ion exchange could provide. This analysis employs a prior model developed by Dmello and Milshtein *et al*., [5] which considers the reactor cost $\left(C_r\right)$, electrolyte cost $\left(C_{el}\right)$, additional cost $\left(C_{add}\right)$, and balance-of-plant (BOP) cost $\left(C_{BOP}\right)$ contributions to the battery price per unit energy $\left(P_0 / E_d\right)$, as shown in Equation 6. The reactor cost incorporates the costs of bipolar plates, membranes, and seals, as well as the reactor ASR and battery discharge time. The BOP costs account for auxiliary equipment such as pumps, sensors, tanks, pipes, and heat exchangers, while the additional costs account for overhead, labor, profit margin, and depreciation. Detailed assumptions and calculations of the reactor, additional, and BOP costs are available elsewhere. [1,5] Note that this work considers a future-state battery price, with a 5 h discharge time, [1,3–5] which does not include the cost of installation or power conditioning systems (e.g., inverter), as opposed to a system price that does incorporate such costs. [5] A prior RFB cost modeling study has estimated that installation and power conditioning systems would contribute future-state costs of \$30 kWh^{-1} and \$20 kWh^{-1} (\$100 kW^{-1} over 5 h discharge), respectively, to the RFB system price. [1] Hence, to achieve the DOE system price target of \$150 kWh^{-1}, [3,4] we can afford a \$100 kWh^{-1} battery price. [5]

$$\frac{P_0}{E_d} = C_r + C_{el} + C_{add} + C_{BOP} \tag{6}$$

To calculate the electrolyte cost, a detailed model (Equation 7) explicitly accounts for the costs associated with the electrolyte materials, namely the active species, solvent, and salt. [5] The electrolyte material costs are comprised of the following parameters: M is the molar mass of the active species, s is the stoichiometric coefficient of the discharge reaction, χ is the depth-of-

discharge, n_e is the number of electrons stored per mole of active material, c_m is the active species cost per unit mass, b is the harmonic mean molality of the active species across both electrodes, c_{sol} is the solvent cost per unit mass, M_{salt} is the molar mass of the salt, c_{salt} is the salt cost per unit mass, and r_{salt} is the arithmetic mean ratio of moles of salt per mole of active species across both electrodes. The +/– subscripts denote the catholyte and anolyte active materials, respectively. The electrolyte materials costs are normalized by the total discharge energy of the battery, encompassed by the following additional parameters: F is the Faraday constant, and U is the cell potential, while ε_e, ε_q, and ε_v are the energy, coulombic, and voltaic efficiencies, respectively. Here we assume an active species molality of 3 mol kg^{-1}. Assumptions for the values of all other parameters not outlined in this work, are described in detail by Dmello and Milshtein et al. [5]

$$C_{el} = \frac{1}{\varepsilon_e \varepsilon_q F \varepsilon_v U}\left(\frac{s_+ M_+}{\chi_+ n_{e+}} c_{m,+} + \frac{s_- M_-}{\chi_- n_{e-}} c_{m,-} + \frac{2}{b} c_{sol} + 2 r_{salt} M_{salt} c_{salt}\right) \tag{7}$$

To illustrate the benefits of reducing salt cost contributions, we define the salt cost factor $\left(C^{\$}_{\text{salt}}\right)$ and the active material cost factor $\left(C^{\$}_{m}\right)$in Equations 8 and 9, respectively, both of which have units of dollars per mole of electrons $\left(\$\ \text{mol}_e^{-1}\right)$:

$$C^{\$}_{\text{salt}} = 2 r_{salt} M_{salt} c_{salt} \tag{8}$$

$$C^{\$}_{\text{m}} = \frac{sM}{\chi n_e} c_m \tag{9}$$

Figure 6.9 shows the relationship between battery price and the salt cost factor for various cell potentials and active material cost factors. In general, as cell potential decreases, the battery price reduces more rapidly with decreasing $C^{\$}_{\text{salt}}$, showing that RFB price becomes more sensitive to variations in $C^{\$}_{\text{salt}}$ at lower cell potentials. Furthermore, battery price rises with increasing $C^{\$}_{m}$,

but variations in $C_m^{\$}$ do not affect the slopes of the price curves in Figure 6.9. Critically, to achieve the recommended battery price of \$100 kWh^{-1}, [5] NAqRFBs will require high cell potentials near ~3 V and values of $C_{salt}^{\$}$ near zero, [1,5] the combination of which has yet to be experimentally realized. Decreasing the salt molecular weight (small M_{salt}) or identifying low cost salts (small c_{salt}) are two strategies to decrease $C_{salt}^{\$}$, but considering the prevalence of salts with fluorinated anions in NAqRFB literature, identifying salts with molecular weights lower than that of $LiBF_4$ (93.75 g mol^{-1}) or costs under \$20 kg^{-1} [1] seems unlikely in the near term. In this work, we pursue a third option of minimizing r_{salt}, by removing the salt altogether and setting r_{salt} = 0, which Figure 6.9 and Equation 6 illustrate is a powerful pathway towards economically viable NAqRFBs.

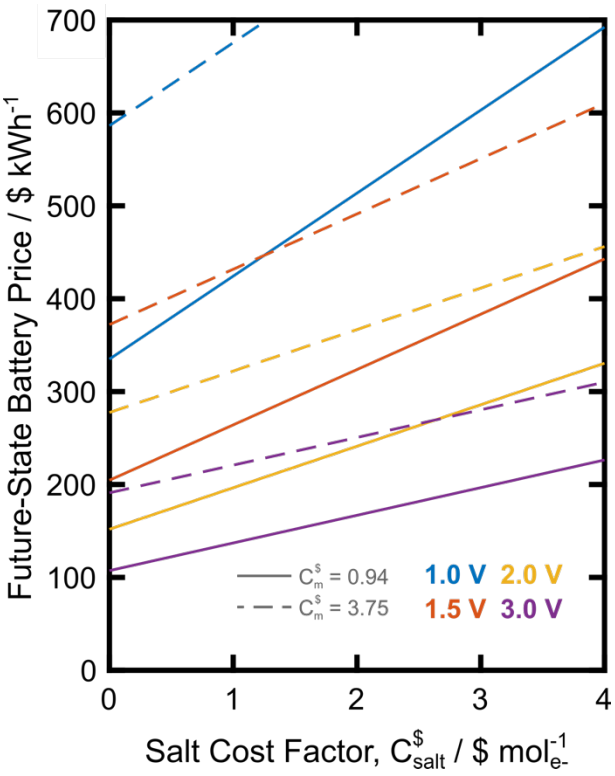

Figure 6.9 Future-state battery price as a function of salt cost factor $\left(C^{\$}_{salt}\right)$ for various cell potentials (U). Solid lines denote active material cost factors of $C^{\$}_{m} = 0.94$, while dashed lines denote $C^{\$}_{m} = 3.75$. As practical examples, consider a cell with a depth-of-discharge (χ) of 80%, stoichiometric coefficients (s) equal to 1, and active material molecular weight (M) of 150 g mol^{-1}. Then, $C^{\$}_{m} = 0.94$ would represent an active material with a cost (c_m) of \$5 kg^{-1}, and $C^{\$}_{m} = 3.75$ would represent an active material with a cost of \$20 kg^{-1}. Further, $C^{\$}_{salt} = 2$ could represent a salt with molecular weight (M_{salt}) of 100 g mol^{-1} and cost (c_{salt}) of \$20 kg^{-1} dissolved in a ratio of 0.5 moles of salt per mole of active species ($r_{salt} = 0.5$).

6.4 Conclusions

Common ion exchange NAqRFBs enable higher active species concentrations, increasing electrolyte energy density, and minimizing the use of expensive NAq solvents and supporting salts. We present a proof-of-concept NAqRFB operating in the absence of supporting salt, utilizing Fc1N112-BF_4 and $Fe(bpy)_3(BF_4)_2$ as model ionic active materials. Efficiencies comparable to state-of-the-art NAqRFBs that employ high concentrations of supporting salt are observed over 10 cycles at a moderate current density (20 mA cm^{-2}). This operation is possible

due to the high conductivities of the active species in MeCN, which remain as ions across all relevant SOCs. Additionally, a chemistry-agnostic techno-economic analysis highlights the potential cost savings of minimizing salt content in NAqRFBs of varying active material cost, salt cost, and cell potential. Overall, this chapter offers proof-of-concept of a NAqRFB operating without supporting salt, opening a pathway for exceptional performance and cost savings.

While the model active species employed in this work are too expensive or unstable for practical grid implementation, [12,23] our investigation highlights the promise of utilizing ionic redox-active species to enable cost effective NAqRFBs without sacrificing performance. Designing lower-cost counter-anions to replace the existing, expensive fluorinated options (e.g., tetrafluoroborate, hexafluorophosphate) could lead to additional cost savings. Further, ionic modification of otherwise neutral redox active compounds, [7,8] or implementation of deep eutectic, redox active melts [50–52] could be powerful approaches in realizing electrolytes with low salt content. Redox active ionic liquids, [52,53] adapted for flow battery applications, represent an extreme realization of the supporting salt free concept by enabling ultra-high concentration or even solvent free electrolytes. Tailoring ionic active species to display desirable physicochemical (i.e., high solubility, [45] low viscosity) and electrochemical properties (i.e., extreme redox potentials, [5] stability [45]) will enable the extension of the supporting salt free concept to more practical NAqRFB prototypes.

6.5 Acknowledgements

I would like to thank Dr. Jarrod Milshtein from Prof. Fikile Brushett's group at MIT for his collaborative efforts on this project. Jarrod performed the conductivity and flow cell studies

shown in this chapter, and developed the techno-economic analysis. I would also like to thank Dr. Tanya Breault who established and assisted with the synthetic efforts.

6.6 References

[1] R.M. Darling, K.G. Gallagher, J.A. Kowalski, S. Ha, F.R. Brushett, Pathways to low-cost electrochemical energy storage: a comparison of aqueous and nonaqueous flow batteries, Energy Environ. Sci. 7 (2014) 3459–3477.

[2] V. Viswanathan, A. Crawford, D. Stephenson, S. Kim, W. Wang, B. Li, G. Coffey, E. Thomsen, G. Graff, P. Balducci, M. Kintner-Meyer, V. Sprenkle, Cost and performance model for redox flow batteries, J. Power Sources. 247 (2014) 1040–1051.

[3] D. Rastler, Market driven distributed energy storage requirements for load management applications, Palo Alto, CA, 2007.

[4] U.S. Department of Energy: Office of Electricity Delivery and Energy Reliability, Energy Storage: Program Planning Document, 2011.

[5] R.D. Dmello, J.D. Milshtein, F.R. Brushett, K.C. Smith, Cost-driven materials selection criteria for redox flow battery electrolytes, J. Power Sources. 330 (2016) 261–272.

[6] J. Huang, L. Cheng, R.S. Assary, P. Wang, Z. Xue, A.K. Burrell, L.A. Curtiss, L. Zhang, Liquid catholyte molecules for nonaqueous redox flow batteries, Adv. Energy Mater. 5 (2015) 1401782.

[7] L. Cosimbescu, X. Wei, M. Vijayakumar, W. Xu, M.L. Helm, S.D. Burton, C.M. Sorensen, J. Liu, V. Sprenkle, W. Wang, Anion-tunable properties and electrochemical performance of functionalized ferrocene compounds, Sci. Rep. 5 (2015) 14117.

[8] X. Wei, L. Cosimbescu, W. Xu, J.Z. Hu, M. Vijayakumar, J. Feng, M.Y. Hu, X. Deng, J. Xiao, J. Liu, V. Sprenkle, W. Wang, Towards high-performance nonaqueous redox flow electrolyte via ionic modification of active species, Adv. Energy Mater. 5 (2014) 1400678.

[9] P.J. Cabrera, X. Yang, J.A. Suttil, K.L. Hawthorne, R.E.M. Brooner, M.S. Sanford, L.T. Thompson, Complexes containing redox noninnocent ligands for symmetric, multielectron transfer nonaqueous redox flow batteries, J. Phys. Chem. C. 119 (2015) 15882–15889.

[10] P.J. Cabrera, X. Yang, J.A. Suttil, R.E.M. Brooner, L.T. Thompson, M.S. Sanford, Evaluation of tris-bipyridine chromium complexes for flow battery applications: Impact of bipyridine ligand structure on solubility and electrochemistry, Inorg. Chem. 54 (2015) 10214–10223.

[11] J.D. Milshtein, A.P. Kaur, M.D. Casselman, J.A. Kowalski, S. Modekrutti, P. Zhang, N.H. Attanayake, C.F. Elliott, S.R. Parkin, C. Risko, F.R. Brushett, S.A. Odom, High current density, long duration cycling of soluble organic active species for non-aqueous redox flow batteries, Energy Environ. Sci. 9 (2016) 3531–3543.

[12] S.M. Laramie, J.D. Milshtein, T.M. Breault, F.R. Brushett, L.T. Thompson, Performance and cost characteristics of multi-electron transfer, common ion exchange non-aqueous redox flow batteries, J. Power Sources. 327 (2016) 681–692.

[13] W. Wang, Q. Luo, B. Li, X. Wei, L. Li, Z. Yang, Recent progress in redox flow battery research and development, Adv. Funct. Mater. 23 (2013) 970–986.

[14] A.Z. Weber, M.M. Mench, J.P. Meyers, P.N. Ross, J.T. Gostick, Q. Liu, Redox flow batteries: a review, J. Appl. Electrochem. 41 (2011) 1137–1164.

[15] A.A. Shinkle, T.J. Pomaville, A.E.S. Sleightholme, L.T. Thompson, C.W. Monroe, Solvents and supporting electrolytes for vanadium acetylacetonate flow batteries, J. Power Sources. 248 (2014) 1299–1305.

[16] J.R. Dahn, J. Jiang, L.M. Moshurchak, M.D. Fleischauer, C. Buhrmester, L.J. Krause, High-rate overcharge protection of LiFePO4-based Li-ion cells using the redox shuttle additive 2,5-ditertbutyl-1,4-dimethoxybenzene, J. Electrochem. Soc. 152 (2005) A1283–A1289.

[17] L. Su, R.M. Darling, K.G. Gallagher, W. Xie, J.L. Thelen, A.F. Badel, J.L. Barton, K.J. Cheng, N.P. Balsara, J.S. Moore, F.R. Brushett, An investigation of the ionic conductivity and species crossover of lithiated Nafion N117 in nonaqueous electrolytes, J. Electrochem. Soc. 163 (2016) A5253–A5262.

[18] F.R. Brushett, J.T. Vaughey, A.N. Jansen, An all-organic non-aqueous lithium-ion redox flow battery, Adv. Energy Mater. 2 (2012) 1390–1396.

[19] I. Escalante-Garcia, J. Wainright, L. Thompson, R. Savinell, Performance of a non-aqueous vanadium acetylacetonate prototype redox flow battery: examination of separators and capacity decay, J. Electrochem. Soc. 162 (2015) A363–A372.

[20] S.H. Oh, C.W. Lee, D.H. Chun, J.D. Jeon, J. Shim, K.H. Shin, J.H. Yang, A metal-free and all-organic redox flow battery with polythiophene as the electroactive species, J. Mater. Chem. A. 2 (2014) 19994–19998.

[21] S.K. Park, J. Shim, J. Yang, K.H. Shin, C.S. Jin, B.S. Lee, Y.S. Lee, J.D. Jeon, Electrochemical properties of a non-aqueous redox battery with all-organic redox couples, Electrochem. Commun. 59 (2015) 68–71.

[22] Y. Matsuda, K. Tanaka, M. Okada, U. Takasu, M. Morita, A rechargeable redox battery utilizing ruthenium complexes with non-aqueous organic electrolyte, J. Appl. Electrochem. 18 (1988) 909–914.

[23] M.H. Chakrabarti, R.A.W. Dryfe, E.P.L. Roberts, Evaluation of electrolytes for redox flow battery applications, Electrochim. Acta. 52 (2007) 2189–2195.

[24] N.S. Hudak, L.J. Small, H.D. Pratt, T.M. Anderson, Through-plane conductivities of membranes for nonaqueous redox flow batteries, J. Electrochem. Soc. 162 (2015) A2188–A2194.

[25] M. Park, N. Lee, S. Lee, K.J. Kim, D. Oh, Y. Kim, High-energy redox-flow batteries with hybrid metal foam electrodes, ACS Appl. Mater. Interfaces. 6 (2014) 10729–10735.

[26] J. Mun, M. Lee, J. Park, D. Oh, D. Lee, S. Doo, Non-aqueous redox flow batteries with nickel and iron tris (2, 2′-bipyridine) complex electrolyte, Electrochem. Solid-State Lett. 15 (2012) A80–A82.

[27] P.J. Cappillino, H.D. Pratt, N.S. Hudak, N.C. Tomson, T.M. Anderson, M.R. Anstey, Application of redox non-innocent ligands to non-aqueous flow battery electrolytes, Adv. Energy Mater. 4 (2014) 1300566.

[28] J. Park, M. Lee, S. Hwang, D. Lee, D. Oh, Redox flow battery: US2012/0171541 A1, 2012.

[29] J.A. Riddick, W.B. Bunger, Organic Solvents, Wiley-Interscience, 1971.

[30] J.D. Milshtein, J.L. Barton, R.M. Darling, F.R. Brushett, 4-acetamido-2,2,6,6-tetramethylpiperidine-1-oxyl as a model organic redox active compound for nonaqueous redox flow batteries, J. Power Sources. 327 (2016) 151–159.

[31] P. Alotto, M. Guarnieri, F. Moro, Redox flow batteries for the storage of renewable energy: a review, Renew. Sustain. Energy Rev. 29 (2014) 325–335.

[32] N. V Plechkova, K.R. Seddon, Applications of ionic liquids in the chemical industry, Chem. Soc. Rev. 37 (2008) 123–150.

[33] M. Ue, Mobility and ionic association of lithium and quaternary ammonium salts in propylene carbonate and γ-butyrolactone, J. Electrochem. Soc. 141 (1994) 3336–3342.

[34] I. Escalante-Garcia, J.S. Wainright, L.T. Thompson, R.F. Savinell, Performance of a non-aqueous vanadium acetylacetonate prototype redox flow battery: Examination of separators and capacity decay, J. Electrochem. Soc. 162 (2015) A363–A372.

[35] S.R. Belding, R.G. Compton, Cyclic voltammetry in the absence of excess supporting electrolyte: The effect of analyte charge, J. Electroanal. Chem. 683 (2012) 1–13.

[36] R.M. Darling, M.L. Perry, The influence of electrode and channel configurations on flow battery performance, J. Electrochem. Soc. 161 (2014) A1381–A1387.

[37] S.H. Shin, S.H. Yun, S.H. Moon, A review of current developments in non-aqueous redox flow batteries: characterization of their membranes for design perspective, RSC Adv. 3 (2013) 9095–9116.

[38] X. Wei, W. Xu, J. Huang, L. Zhang, E. Walter, C. Lawrence, M. Vijayakumar, W.A. Henderson, T. Liu, L. Cosimbescu, B. Li, V. Sprenkle, W. Wang, Radical compatibility with nonaqueous electrolytes and its impact on an all-organic redox flow battery, Angew. Chemie Int. Ed. 54 (2015) 8684–8687.

[39] Y.K. Zeng, X.L. Zhou, L. An, L. Wei, T.S. Zhao, A high-performance flow-field structured iron-chromium redox flow battery, J. Power Sources. 324 (2016) 738–744.

[40] C.R. Dennison, E. Agar, B. Akuzum, E.C. Kumbur, Enhancing mass transport in redox flow batteries by tailoring flow field and electrode design, J. Electrochem. Soc. 163 (2015) A5163–A5169.

[41] Q.H. Liu, G.M. Grim, a. B. Papandrew, A. Turhan, T.A. Zawodzinski, M.M. Mench,

High performance vanadium redox flow batteries with optimized electrode configuration and membrane selection, J. Electrochem. Soc. 159 (2012) A1246–A1252.

[42] X.-Z. Yuan, C. Song, H. Wang, J. Zhang, Electrochemical impedance spectroscopy in PEM fuel cells, Fundam. Appl. London. (2010).

[43] C.N. Sun, F.M. Delnick, D.S. Aaron, A.B. Papandrew, M.M. Mench, T.A. Zawodzinski, Resolving losses at the negative electrode in all-vanadium redox flow batteries using electrochemical impedance spectroscopy, J. Electrochem. Soc. 161 (2014) A981–A988.

[44] W. Duan, R.S. Vemuri, J.D. Milshtein, S. Laramie, R.D. Dmello, J. Huang, L. Zhang, D. Hu, M. Vijayakumar, W. Wang, J. Liu, R.M. Darling, L. Thompson, K. Smith, J.S. Moore, F.R. Brushett, X. Wei, A symmetric organic-based nonaqueous redox flow battery and its state of charge diagnostics by FTIR, J. Mater. Chem. A. 4 (2016) 5448–5456.

[45] J.A. Kowalski, L. Su, J.D. Milshtein, F.R. Brushett, Recent advances in the molecular engineering of redox active organic species for nonaqueous flow batteries, Curr. Opin. Chem. Eng. 13 (2016) 45–52.

[46] A.J. Smith, J.C. Burns, D. Xiong, J.R. Dahn, Interpreting high precision coulometry results on Li-ion cells, J. Electrochem. Soc. 158 (2011) A1136.

[47] A. Orita, M.G. Verde, M. Sakai, Y.S. Meng, The impact of pH on side reactions for aqueous redox flow batteries based on nitroxyl radical compounds, J. Power Sources. 321 (2016) 126–134.

[48] M. Skyllas-Kazacos, M. Kazacos, State of charge monitoring methods for vanadium redox flow battery control, J. Power Sources. 196 (2011) 8822–8827.

[49] B. Hwang, M.S. Park, K. Kim, Ferrocene and cobaltocene derivatives for non-aqueous redox flow batteries, ChemSusChem. 8 (2015) 310–314.

[50] M.A. Miller, J.S. Wainright, R.F. Savinell, Communication—Iron ionic liquid electrolytes for redox flow battery applications, J. Electrochem. Soc. 163 (2016) A578–A579.

[51] L. Bahadori, M.A. Hashim, N.S.A. Manan, F.S. Mjalli, I.M. AlNashef, N.P. Brandon, M.H. Chakrabarti, Investigation of ammonium- and phosphonium-based deep eutectic solvents as electrolytes for a non-aqueous all-vanadium redox cell, J. Electrochem. Soc. 163 (2016) A632–A638.

[52] M.H. Chakrabarti, F.S. Mjalli, I.M. AlNashef, M.A. Hashim, M.A. Hussain, L. Bahadori, C.T.J. Low, Prospects of applying ionic liquids and deep eutectic solvents for renewable energy storage by means of redox flow batteries, Renew. Sustain. Energy Rev. 30 (2014) 254–270.

[53] E. Mourad, L. Coustan, S.A. Freunberger, A. Mehdi, A. Vioux, F. Favier, O. Fontaine, Biredox ionic liquids: electrochemical investigation and impact of ion size on electron transfer, Electrochim. Acta. 206 (2016) 3–8.

Chapter 7

Conclusions and Future Directions

7.1 Conclusions

Non-aqueous redox flow batteries (NAqRFBs) have recently received considerable attention as promising high energy density grid-level energy storage devices. Despite many attractive features, NAqRFBs are still at an early stage of development and currently suffer from limited stability and high projected costs. Research described in this thesis aimed to advance NAqRFBs toward commercial viability through the development of structure-function relationships that facilitate the design of stable active species and the introduction of design strategies that reduce the cost of these devices.

7.1.1 Active Species Development

The first section of this thesis focused on the development of trends that relate structural features to solubility, electrochemistry (number of redox events, standard potentials, reversibility), and electrochemical stability. Tridentate metal coordination complexes (MCCs) were introduced as promising active species and the first step was to expand existing relationships for bidentate MCCs to tridentate ligand classes. In Chapter 2, I discussed the synthesis of a library of tridentate bis(triazole)pyridine (BTP) MCCs, implementing systematic ligand variations to identify trends in electrochemical properties and solubility. Analysis of the electrochemical behavior and solubility of each complex revealed that these properties can be

tuned independently, highlighting the appeal of tridentate MCCs. The versatility of these design strategies was demonstrated through the synthesis and characterization of an analogous terpyridine MCC. The voltammetry results demonstrated that the identified trends in the number and potential of redox features as well as solubility hold for other classes of tridentate ligands. Overall, this work established design strategies that can be used to rapidly engineer soluble MCCs with desirable electrochemical properties. However, after considerable synthetic efforts, BTP MCCs were found to be electrochemically unstable. This is a common trend for NAqRFB active species and motivated the implementation of a new approach for the design of active species.

The design strategy that I established prioritizes electrochemical stability. The first step is to identify a stable ligand class using a rapid screening process or chemical intuition. After a stable material is identified, the peripheral ligand structure and/or metal center can then be synthetically modified to achieve the electrochemical and solubility properties required for NAqRFB active species. To successfully apply this method and enable the efficient design of stable active materials, it will first be necessary to develop an understanding of the aspects of molecular structure that impact cycling stability.

As a first step, I investigated the impact of metal center on MCC electrochemical stability. In Chapter 3, I discussed the development of a series of tridentate bipyridylimino isoindoline (BPI) MCCs. Systematic modification of the BPI metal center revealed strong correlations between MCC electrochemical stability and structural characteristics. At negative potentials, the stability trends were explained using known rates of ligand substitution at divalent metal centers. As these properties are dependent solely on the metal center, these trends are expected to be widely applicable to all class of MCCs. BPI complexes of nickel were found to be

remarkably stable and completed 200 charge and discharge cycles through two reductions with <5% capacity fade. Applying the method just discussed, this material was functionalized to enhance solubility and a complex was identified that possesses a previously unprecedented combination of high solubility, multiple electron transfers at low redox potentials, and high stability in the charged state, even at high concentration. Chapter 3 concludes with a discussion of ligand characteristics that impact electrochemical stability. Overall, these studies offer the first demonstration of stable $2e^-$ cycling and deliver a promising anolyte candidate for NAqRFBs. They also provide key insights into chemical design principles for future classes of MCC-based active species.

A number of factors are expected to impact cycling stability, including active species structure, electrolyte composition, and flow cell components (membrane/separator, electrode, cell hardware). In addition to the investigation of structural characteristics that impact stability, I also investigated the effect of cell components. In Chapter 4, I discussed the impact of electrode material on the electrochemical stability and flow cell performance of 4-acetamido-2,2,6,6-tetramethylpiperidine-1-oxyl (ATEMPO). Comparative studies of the areal specific resistance (ASR) and limiting current for different carbon based electrode materials revealed that in general, carbon papers and cloth offer better performance than carbon felt. It should be noted that the slight variations observed in performance will have a negligible impact on lab scale flow cell studies, but they will become relevant for large scale tests. A simple techno-economic analysis was used to demonstrate this point by presenting the cost savings that result from small changes in ASR. In terms of stability, ATEMPO was shown to be insensitive to changes in the electrode material, which is an excellent trait for an active species to possess. Overall, this work offers a comparative study of the performance of different electrode materials that will be valuable for

the future development and optimization of large scale NAqRFBs. These studies also add breadth to the discussion of factors that impact NAqRFB active species stability.

Taken as a whole, these results can be used to guide the future design of stable NAqRFBs. The development of an electrochemically stable active species is critical for the success of NAqRFBs and the trends I developed herein offer an efficient route for this development. Combining the stability, solubility and electrochemical trends that have been discussed will allow for the rapid identification and characterization of promising active species. With the development of promising materials, flow cell studies will become increasingly relevant and the results from the electrode studies can be used to readily optimize stability and performance in a flow environment.

7.1.2 Design Concepts

The second section of this thesis discussed design strategies for increasing the viability of NAqRFBs. As promising NAqRFB active materials continue to be identified, it is of increasing importance to consider how these materials could be utilized in a full flow system. In Chapter 5, I introduced a method for designing NAqRFBs that employ active species with either single or unbalanced redox events. These systems require the use of different anolyte and catholyte chemistries and potentially mixed electrolytes. The developed procedure investigated possible interactions between different active species by examining the stability of all the active materials, across all relevant oxidation states, both individually and as mixtures. It included cyclic voltammetry, bulk electrolysis, and H-cell experiments, culminating in $1e^-$ and $2e^-$ transfer cycling in a full flow cell. The proof of concept multi-electron NAqRFB exhibited complex charging phenomena, which were readily explained using the results of the systematic

compatibility studies. The versatility of this methodology was then demonstrated through the design of a more stable $2e^-$ system employing a BPI MCC as the anolyte material. Overall, this work provides a route for the development of NAqRFBs employing materials that are unusable alone. Further, it offers a process for the interpretation of complex charging behavior. It can also easily be extended to other promising redox chemistries as they emerge, including all-organic, all-MCC, and mixed MCC/organic systems, to facilitate the development of stable, soluble, multi-electron NAqRFBs.

To achieve economically viable NAqRFBs, it will be necessary to decrease manufacturing costs, advance materials performance, and improve cell architecture. In conjunction with these strategies, it will also be necessary to develop new design concepts to further drive down costs. In Chapter 6, I introduced the concept of a common ion exchange NAqRFB. In this type of cell the active species have charges of the same sign, either positive or negative, at all states of charge, and as a result, only a single ion of the supporting salt migrates across the separator as a charge carrier. Common ion exchange systems enable higher active species concentrations, increasing electrolyte energy density, and minimizing the use of expensive NAq solvents and supporting salts. In this chapter I presented a proof-of-concept common ion exchange NAqRFB operating in the complete absence of supporting salt. Efficiencies comparable to state-of-the-art NAqRFBs that employ high concentrations of supporting salt were observed over 10 cycles at a moderate current density (20 mA cm^{-2}). This operation is possible due to the high conductivities of the active species in acetonitrile, which remain as ions across all relevant SOCs. A chemistry-agnostic techno-economic analysis then highlighted the potential cost savings of minimizing salt content in NAqRFBs of varying active material cost, salt cost, and cell potential. Overall, this work offers proof-of-concept of a

NAqRFB operating without supporting salt, opening a pathway for exceptional cost savings while maintaining high performance.

7.2 Future Directions

7.2.1. Stability

One of the greatest challenges facing NAqRFBs is the lack of stable, soluble active species capable of multiple electron transfers. Over the past few years, significant progress has been made in the design of highly soluble active species. [1–3] Further, there is a general understanding of the molecular characteristics that afford high solubility in non-aqueous media. [4,5] However, very few materials have been identified with high electrochemical stability. In general, there is a poor understanding of the mechanisms resulting in capacity fade as well as a lack of systematic studies to identify the molecular features that provide high stability. This thesis started to fill this gap by examining the impact of metal center and ligand structure on electrochemical stability, but additional efforts are required to develop a comprehensive understanding of stability.

Based on the results presented in this dissertation, high denticity, anionic ligands composed of rings with high bond dissociation energies are desirable. It is expected that tridentate ligands will offer an optimal balance between solubility and stability, although investigations of higher denticity ligands would be of interest. Further, it would be valuable to include a wider variety of heteroatoms, such as S and O. These heteroatoms may dictate the degradation pathway, ultimately leading to more stable MCCs. Overall, ligand charge and chelate ring size are expected to have the greatest impact on MCC electrochemical stability. A more comprehensive, systematic investigation of various ligand structures could provide

extremely valuable quantitative information on the characteristics that contribute to high cycling stability.

In addition to the factors that have been discussed, studies on organic active species have demonstrated that both the location [6] and composition [7] of the functional groups have a significant impact on electrochemical stability. However, these studies only offer a comparison of a few molecules and provide no explanation relating the structural differences to the variations in stability. Systematic studies on the impact of functional groups on stability would be highly relevant and could be performed on organic molecules or MCCs. The primary criteria would be a material that is readily available and easily modified. Trends developed for either material would be expected to translate across all types of active species. In addition to the structure of the active species, the solvent and supporting electrolyte are also expected to affect cycling stability. [8] Electrolyte modifications offer an engineering route to optimizing the performance of a promising active species. In general, while there are a variety of molecular characteristics that are expected to affect stability, systematic studies are necessary to fully understand the impact of each of these factors. The extension of the developed structure-property relationships to include additional parameters will enable the efficient design of active species with properties desirable for NAqRFB applications.

Finally, while the electrode material was shown to have a minimal impact on cycling stability and flow cell performance for ATEMPO, this is expected to be active species dependent. For example, vanadium acetylacetonate is sensitive to the presence of oxygen and water, [9] which could vary across the surface of different electrodes. Further studies on a more sensitive active species would be required to fully understand the impact of electrode material on electrochemical stability. Additionally, electrode research for aqueous RFBs has shown that

treatments can be a highly effective route for enhancing performance. [10] After a promising material is identified it would be of interest to investigate electrode treatments (electrochemical, chemical or thermal) to provide another avenue for optimizing flow cell performance.

7.2.2. Design Concepts

The ultimate application of the design concepts presented in this thesis would be the development of a stable, multielectron NAqRFB operating at a high active species concentration. To achieve this aim, it will be necessary to first focus on molecular development. The systematic approaches can then easily be extended to promising active species as they emerge, including organics, metal coordination complexes (MCCs), and mixed MCC/organic systems. BPI MCCs were identified as promising anolyte candidates in this thesis and could be paired with an appropriate catholyte to achieve a high concentration cell. Since the maximum solubility of each active species decreases in a mixed electrolyte solution, it would be ideal if electrolyte mixing were not necessary for operation. This will require the development of highly selective membranes that are stable in non-aqueous environments. Membranes are currently under development for non-aqueous systems, but this field has yet to receive significant attention. [11]

To achieve the high concentrations necessary for commercial viability, it will be necessary to employ innovative design strategies, such as the common ion exchange system presented in this thesis. While the model active species employed in this work are too expensive or unstable for practical grid implementation, [12,13] our investigation highlights the promise of utilizing ionic redox-active species to enable cost effective NAqRFBs without sacrificing performance. Designing lower-cost counter-anions to replace the existing, expensive fluorinated options (e.g., tetrafluoroborate, hexafluorophosphate) could lead to additional cost savings.

Further, ionic modification of otherwise neutral redox active compounds, [14,15] or implementation of deep eutectic, redox active melts [16–18] could be powerful approaches in realizing electrolytes with low salt content. Redox active ionic liquids, [18,19] adapted for flow battery applications, represent an extreme realization of the supporting salt free concept by enabling ultra-high concentration or even solvent free electrolytes. Tailoring ionic active species to display desirable physicochemical (i.e., high solubility, [20] low viscosity) and electrochemical properties (i.e., extreme redox potentials, [21] stability [20]) will enable the extension of the supporting salt free concept to more practical NAqRFB prototypes.

7.3 References

[1] X. Wei, W. Xu, M. Vijayakumar, L. Cosimbescu, T. Liu, V. Sprenkle, W. Wang, TEMPO-based catholyte for high-energy density nonaqueous redox flow batteries, Adv. Mater. 26 (2014) 7649–7653.

[2] P.J. Cabrera, X. Yang, J.A. Suttil, K.L. Hawthorne, R.E.M. Brooner, M.S. Sanford, L.T. Thompson, Complexes containing redox noninnocent ligands for symmetric, multielectron transfer nonaqueous redox flow batteries, J. Phys. Chem. C. 119 (2015) 15882–15889.

[3] X. Wei, L. Cosimbescu, W. Xu, J.Z. Hu, M. Vijayakumar, J. Feng, M.Y. Hu, X. Deng, J. Xiao, J. Liu, V. Sprenkle, W. Wang, Towards high-performance nonaqueous redox flow electrolyte via ionic modification of active species, Adv. Energy Mater. 5 (2014) 1400678.

[4] P.J. Cabrera, X. Yang, J.A. Suttil, R.E.M. Brooner, L.T. Thompson, M.S. Sanford, Evaluation of tris-bipyridine chromium complexes for flow battery applications: Impact of bipyridine ligand structure on solubility and electrochemistry, Inorg. Chem. 54 (2015) 10214–10223.

[5] J.A. Suttil, J.F. Kucharyson, I.L. Escalante-Garcia, P.J. Cabrera, B.R. James, R. F. Savinell, M.S. Sanford, L. Thompson, Metal acetylacetonate complexes for high energy density non-aqueous redox flow batteries, J. Mater. Chem. A. 3 (2015) 7929–7938.

[6] J. Huang, B. Pan, W. Duan, X. Wei, R.S. Assary, L. Su, F.R. Brushett, L. Cheng, C. Liao, M.S. Ferrandon, W. Wang, Z. Zhang, A.K. Burrell, L.A. Curtiss, I.A. Shkrob, J.S. Moore, L. Zhang, The lightest organic radical cation for charge storage in redox flow batteries, Sci. Rep. 6 (2016) 32102.

[7] J.D. Milshtein, A.P. Kaur, M.D. Casselman, J.A. Kowalski, S. Modekrutti, P. Zhang, N.H. Attanayake, C.F. Elliott, S.R. Parkin, C. Risko, F.R. Brushett, S.A. Odom, High current density, long duration cycling of soluble organic active species for non-aqueous redox flow batteries, Energy Environ. Sci. 9 (2016) 3531–3543.

[8] X. Wei, W. Xu, J. Huang, L. Zhang, E. Walter, C. Lawrence, M. Vijayakumar, W. a. Henderson, T. Liu, L. Cosimbescu, B. Li, V. Sprenkle, W. Wang, Radical compatibility with nonaqueous electrolytes and its impact on an all-organic redox flow battery, Angew. Chemie Int. Ed. 54 (2015) 8684–8687.

[9] A.A. Shinkle, A.E.S. Sleightholme, L.D. Griffith, L.T. Thompson, C.W. Monroe, Degradation mechanisms in the non-aqueous vanadium acetylacetonate redox flow battery, J. Power Sources. 206 (2012) 490–496.

[10] K.J. Kim, M.-S. Park, Y.-J. Kim, J.H. Kim, S.X. Dou, M. Skyllas-Kazacos, A technology review of electrodes and reaction mechanisms in vanadium redox flow batteries, J. Mater. Chem. A. 3 (2015) 16913–16933.

[11] S.H. Shin, S.H. Yun, S.H. Moon, A review of current developments in non-aqueous redox flow batteries: characterization of their membranes for design perspective, RSC Adv. 3 (2013) 9095–9116.

[12] M.H. Chakrabarti, R.A.W. Dryfe, E.P.L. Roberts, Evaluation of electrolytes for redox flow battery applications, Electrochim. Acta. 52 (2007) 2189–2195.

[13] S.M. Laramie, J.D. Milshtein, T.M. Breault, F.R. Brushett, L.T. Thompson, Performance and cost characteristics of multi-electron transfer, common ion exchange non-aqueous redox flow batteries, J. Power Sources. 327 (2016) 681–692.

[14] L. Cosimbescu, X. Wei, M. Vijayakumar, W. Xu, M.L. Helm, S.D. Burton, C.M. Sorensen, J. Liu, V. Sprenkle, W. Wang, Anion-tunable properties and electrochemical performance of functionalized ferrocene compounds, Sci. Rep. 5 (2015) 14117.

[15] X. Wei, L. Cosimbescu, W. Xu, J.Z. Hu, M. Vijayakumar, J. Feng, M.Y. Hu, X. Deng, J. Xiao, J. Liu, V. Sprenkle, W. Wang, Towards high-performance nonaqueous redox flow electrolyte via ionic modification of active species, Adv. Energy Mater. 5 (2014) 1400678.

[16] M.A. Miller, J.S. Wainright, R.F. Savinell, Communication—Iron ionic liquid electrolytes for redox flow battery applications, J. Electrochem. Soc. 163 (2016) A578–A579.

[17] L. Bahadori, M.A. Hashim, N.S.A. Manan, F.S. Mjalli, I.M. AlNashef, N.P. Brandon, M.H. Chakrabarti, Investigation of ammonium- and phosphonium-based deep eutectic solvents as electrolytes for a non-aqueous all-vanadium redox cell, J. Electrochem. Soc. 163 (2016) A632–A638.

[18] M.H. Chakrabarti, F.S. Mjalli, I.M. AlNashef, M.A. Hashim, M.A. Hussain, L. Bahadori, C.T.J. Low, Prospects of applying ionic liquids and deep eutectic solvents for renewable energy storage by means of redox flow batteries, Renew. Sustain. Energy Rev. 30 (2014) 254–270.

[19] E. Mourad, L. Coustan, S.A. Freunberger, A. Mehdi, A. Vioux, F. Favier, O. Fontaine, Biredox ionic liquids: electrochemical investigation and impact of ion size on electron transfer, Electrochim. Acta. 206 (2016) 3–8.

[20] J.A. Kowalski, L. Su, J.D. Milshtein, F.R. Brushett, Recent advances in the molecular engineering of redox active organic species for nonaqueous flow batteries, Curr. Opin. Chem. Eng. 13 (2016) 45–52.

[21] R.D. Dmello, J.D. Milshtein, F.R. Brushett, K.C. Smith, Cost-driven materials selection criteria for redox flow battery electrolytes, J. Power Sources. 330 (2016) 261–272.